

**SYSTEM DESIGN METHODOLOGY AND IMPLEMENTATION  
OF MICRO AERIAL VEHICLES**

**SWEE KING PHANG**

**NATIONAL UNIVERSITY OF SINGAPORE**

**2014**



**SYSTEM DESIGN METHODOLOGY AND IMPLEMENTATION  
OF MICRO AERIAL VEHICLES**

**SWEE KING PHANG**

*(B. Eng. (Hons.), NUS)*

**A THESIS SUBMITTED**

**FOR THE DEGREE OF DOCTOR OF PHILOSOPHY**

**NUS GRADUATE SCHOOL FOR INTEGRATIVE SCIENCES  
AND ENGINEERING**

**NATIONAL UNIVERSITY OF SINGAPORE**

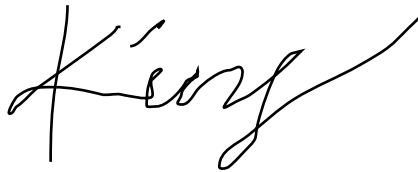
**2014**



## **Declaration**

**I hereby declare that this thesis is my original work and it has been written by me in its entirety. I have duly acknowledged all the sources of information which have been used in the thesis.**

**This thesis has also not been submitted for any degree in any university previously.**



---

**Swee King Phang**

**December 5, 2014**



# Acknowledgements

I would like to express my sincere gratitude to my supervisor, Prof. Ben M. Chen, for his continuous motivation and guidance during my Ph.D. studies. Not only he showed me the road and helped to get me started on the path to my Ph.D. degree, but his enthusiasm, encouragement and faith in me throughout has inspired me to gain confidence and to be persevered with my research and study.

I am also grateful to the rest of my thesis committees, Prof. S. Z. Sam Ge, Prof. T. H. Lee and Dr. Chang Chen, for their assistance and suggestions throughout the meetings during my Ph.D. studies.

To all my friends in the Control Lab, thank you—especially to the members of the NUS UAV Research Group for always listening and giving me words of encouragement. UAV research is so broad that it is not possible to be done alone, and I am grateful that we are in the same team. Special thank to Li Kun who has been working together for the past 3 years, for his help in circuit design. Dr Wang Fei, my senior who has guided me through many obstacles I faced during my Ph.D. studies. Lai Shupeng, my work partner to realize the application of the MAV during Singapore Airshow 2014. Huang Rui, for his help in developing vision motion estimation algorithm for the MAV. Prof. Wang Biao, for his professional and critical suggestions for my Ph.D. project. I also wish to thank all the other members who have taken part in various UAV competitions with me in the past few years—Dr. Dong Xiangxu, Dr. Lin Feng, Dr. Peng Kemaoy, Kevin Ang, Liu Peidong, Wang Kangli, Ke Yijie, Cui Jinqiang, Yang Zhaolin, Lin Jing, Pang Tao, Bai Limiao, Deng Di, Li Xiang and Lan Menglu.

Last but not least, I am grateful for my family members for their unconditional support and never-ending love, which encourage and motivate me to survive my Ph.D. studies in Singapore.



# Contents

<b>Acknowledgements</b>	<b>v</b>
<b>Summary</b>	<b>xi</b>
<b>List of Tables</b>	<b>xiii</b>
<b>List of Figures</b>	<b>xv</b>
<b>List of Symbols</b>	<b>xix</b>
<b>1 Introduction</b>	<b>1</b>
1.1 Introduction . . . . .	1
1.2 Literature Review . . . . .	2
1.2.1 Platform Types . . . . .	2
1.2.2 Challenges on Flight Control . . . . .	7
1.3 Thesis Outline . . . . .	10
<b>2 Platform Selection</b>	<b>13</b>
2.1 Introduction . . . . .	13
2.2 Maneuverability . . . . .	16
2.3 Size and Weight . . . . .	16
2.4 Structure Complexity . . . . .	17

2.5	Summary . . . . .	18
<b>3</b>	<b>Airframe Design</b>	<b>21</b>
3.1	Introduction . . . . .	21
3.2	Material . . . . .	21
3.2.1	Bi-Directional Plain Weave Carbon Fiber . . . . .	22
3.2.2	Uni-Directional Carbon Fiber . . . . .	22
3.3	Vibration Analysis Formulation . . . . .	23
3.3.1	Natural Mode Analysis . . . . .	24
3.3.2	Frequency Response Analysis . . . . .	25
3.4	Finite Element Analysis . . . . .	26
3.5	Case Study . . . . .	27
3.5.1	Single Quadrotor Arm . . . . .	30
3.5.2	Full Quadrotor Configuration . . . . .	35
3.6	Experimental Validation . . . . .	37
3.7	Quadrotor Body Design . . . . .	39
<b>4</b>	<b>Avionics Design</b>	<b>45</b>
4.1	Introduction . . . . .	45
4.2	Motor and Propeller . . . . .	47
4.3	Micro-Processor . . . . .	48
4.4	Inertial Measurement Unit . . . . .	50
4.5	Brushed Electronic Speed Controller . . . . .	51
4.6	Radio-Frequency Receiver . . . . .	52
4.7	Data Logger . . . . .	53
4.8	Power Supply . . . . .	54
4.9	Avionic Circuit Board Design . . . . .	55
4.10	Camera Subsystem . . . . .	59

4.11	Software Realization . . . . .	61
4.11.1	Read and Decode IMU Data . . . . .	62
4.11.2	Read and Decode Receiver Data . . . . .	62
4.11.3	Generate PWM Signals . . . . .	63
4.11.4	Total Program Run-Time . . . . .	64
<b>5</b>	<b>Dynamics Modeling</b>	<b>69</b>
5.1	Introduction . . . . .	69
5.2	Working Principle . . . . .	71
5.3	Coordinate Systems . . . . .	72
5.4	Kinematics . . . . .	73
5.5	6 DOF Rigid-Body Dynamics . . . . .	73
5.6	Forces and Moments Generation . . . . .	74
5.6.1	Gravitational Force . . . . .	74
5.6.2	Rotor Movement . . . . .	75
5.7	Motor Dynamics . . . . .	77
5.7.1	Equivalent Analog Voltage . . . . .	77
5.7.2	Electrical and Mechanical Dynamics . . . . .	78
5.8	Parameter Identification . . . . .	81
5.8.1	Measurable Parameters . . . . .	81
5.8.2	Gravity . . . . .	81
5.8.3	Moment of Inertia . . . . .	81
5.8.4	Motor Dynamics . . . . .	83
5.8.5	Aerodynamics Coefficients . . . . .	84
5.9	Model Verification . . . . .	87
<b>6</b>	<b>Flight Control Systems Design</b>	<b>95</b>
6.1	Introduction . . . . .	95

6.2	Feedback Linearization . . . . .	99
6.3	Inner Loop Design . . . . .	100
6.4	Outer Loop Design . . . . .	101
6.5	Flight Control Simulation . . . . .	103
6.6	Flight Control Verification . . . . .	103
<b>7</b>	<b>Trajectory Planning</b>	<b>109</b>
7.1	Introduction . . . . .	109
7.2	Normalized Uniform B-Spline . . . . .	111
7.3	Minimum Jerk Trajectory: Closed Solution . . . . .	114
7.4	Minimum Jerk Trajectory: Quadratic Programming . . . . .	117
7.5	Implementation on Ground Station . . . . .	119
<b>8</b>	<b>Case Study: UAV Calligraphy</b>	<b>125</b>
8.1	Introduction . . . . .	125
8.2	Hardware Setup . . . . .	126
8.3	Handwriting Extractions . . . . .	127
8.4	Trajectory Generating: Optimal Time Segmentation . . . . .	129
8.5	MAV Autonomous Writing Results . . . . .	132
<b>9</b>	<b>Conclusion and Future Work</b>	<b>139</b>
	<b>Bibliography</b>	<b>143</b>
	<b>Publications</b>	<b>153</b>

# Summary

This thesis aims to develop micro-unmanned aerial vehicles (MAVs), which will be utilized in indoor projects, such as spying, mapping and surveillance. The MAVs developed will be fully autonomous, with less than 50 g take-off weight in total. Quadrotor platform is first selected as the MAV platform. The use of quadrotor platform is justified from the ease of control law implementation and the scalability of the platform. Once the platform has been selected, four major aspects for development are considered: structure design, avionics design, model-based controller design, and autonomous flight path generation. Structural analysis is important to aircraft implementation, especially when dimension and weight are the main constraints to the design. In general, the lighter and smaller the structure is, the lower is the natural frequency of the structure. The aircraft platform is to design in a way that the vibration frequency caused by the motor rotation is much lower than its natural frequency. Finite element analysis will be presented with the aid of MSC Patran and Nastran simulation programs. Next, avionics design details the selection of hardware and electronics to build a quadrotor MAV. In order for autonomous control, sensors like inertial measurement unit and camera are essential to the on-board system. Each of the components is selected with the trade-off between weight, cost, and performance. For further weight reduction, these components are redesigned and customized into a single circuit board. Subsequently, a model based control methodology is adopted for the MAV control. A nonlinear model of the aircraft is first derived. Method of identifying parameters of the model is then proposed and verified. Based on the derived model, inner and outer loop controllers are designed. The quadrotor system is first linearized via feedback linearization,

then a linear control law based on linear quadratic regulator (LQR) design is implemented to control its orientation. Position control is designed according to the robust and perfect tracking (RPT) controller. Once the stability and controllability of the MAV are guaranteed, a minimum jerk trajectory is generated. With limitation on maximum acceleration and velocity of the MAV, an optimal path can be pre-generated, based on user specific's waypoints. This guarantees the resulting reference path is continuous up to its acceleration such that RPT control law could work well. Finally, an application of the MAVs is proposed and realized in a flight demo in Singapore Airshow 2014.

# List of Tables

1.1	Target weight distribution of the MAV . . . . .	10
2.1	Advantages and disadvantages of each platform . . . . .	19
3.1	Material properties of bi-directional plain weave carbon/epoxy T300/5208 . . . . .	23
3.2	Material properties of uni-directional carbon/epoxy T300/976 . . . . .	24
3.3	Natural frequencies of thin plate with varying length . . . . .	30
3.4	Natural frequencies of different beam (1 mm thickness) . . . . .	31
3.5	Natural frequencies of different beam (0.5 mm thickness) . . . . .	32
3.6	Natural frequencies of the rectangular hollow beam . . . . .	35
3.7	Natural frequencies of the circular hollow beam . . . . .	36
3.8	Natural mode comparison . . . . .	38
4.1	Key parameters of ATmega328P . . . . .	50
4.2	Important specifications of VN-100 SMD . . . . .	51
4.3	Total current consumption of MAV system . . . . .	55
4.4	Specifications of the analog camera . . . . .	60
4.5	Specifications of the video communication modules . . . . .	60
4.6	Weight breaks down for quadrotor MAV . . . . .	61
5.1	Main movements of MAV . . . . .	72

5.2	Identified parameters . . . . .	89
9.1	Weight budget and final weight . . . . .	140



# List of Figures

1.1	Examples of fixed-wing MAV: (a) Black Widow; (b) MLB; (c) Flexible-Wing; (d) NPS . . . . .	3
1.2	Examples of rotary-wing MAV: (a) muFly; (b) Mesicopter . . . . .	4
1.3	Examples of flapping-wing MAV: (a) Hummingbird; (b) Entomopter; (c) MicroBat; (d) DelFly . . . . .	5
1.4	muFly MAV: (a) its components layout; (b) its swash plate design . . . . .	6
2.1	Rotary-wing platforms . . . . .	14
2.2	Fixed-wing platform . . . . .	15
2.3	Flapping-wing platform . . . . .	15
2.4	Changes in collective pitch of the blade . . . . .	18
2.5	A swash plate of a small scale RC helicopter . . . . .	19
3.1	Carbon/epoxy T300/5208 . . . . .	22
3.2	Carbon/epoxy T300/976 . . . . .	23
3.3	Modeling and simulation process . . . . .	28
3.4	Cross-section of beams . . . . .	29
3.5	Thin plate model in MSC Patran . . . . .	30
3.6	Mode shape for rectangular shaped beam . . . . .	32
3.7	Mode shape for rectangular hollow shaped beam . . . . .	33

3.8	Mode shape for circular hollow shaped beam . . . . .	33
3.9	Mode shape for T shaped beam . . . . .	34
3.10	Mode shape for N shaped beam . . . . .	34
3.11	Quadrotor model with rectangular hollow beams . . . . .	36
3.12	Displacement response at tip of the arm . . . . .	38
3.13	Fabricated quadrotor body and its counterpart designed in SolidWorks . . . . .	40
3.14	Motor holder designed in SolidWorks . . . . .	40
3.15	Full micro quadrotor body designed in SolidWorks with dimension (in mm) . . . . .	41
3.16	Fabricated MAV platform . . . . .	41
3.17	Vibration analysis of quadrotor frame . . . . .	43
4.1	Essential hardware and electronics needed for a quadrotor MAV . . . . .	46
4.2	Motor and propeller of the MAV . . . . .	48
4.3	Components used in avionic system design . . . . .	49
4.4	PCTx cables from Endurance R/C . . . . .	53
4.5	Battery for the MAV . . . . .	54
4.6	Flow chart for MAV PCB design . . . . .	56
4.7	Schematic diagrams . . . . .	57
4.8	PCB layout . . . . .	58
4.9	Tasks to be carried out on MAV's processor . . . . .	61
4.10	PPM signal from receiver . . . . .	63
4.11	Flow of program in getting PPM reading . . . . .	63
4.12	Synchronization of four PWM outputs . . . . .	65
4.13	Flow of program in generating PWM outputs . . . . .	66
4.14	Total program run-time . . . . .	67
5.1	Overall model of the quadrotor . . . . .	70
5.2	Pitching, rolling and yawing of a quadrotor MAV . . . . .	71

5.3	Trifilar pendulum method . . . . .	82
5.4	Steady-state response of the ESC on two different inputs . . . . .	84
5.5	Linear relationship obtained experimentally . . . . .	85
5.6	Rotational speed response of the motor supplied with analog voltage . . . . .	85
5.7	Setup to obtain motor speed and thrust/torque produced . . . . .	86
5.8	Nano17 F/T Sensor . . . . .	87
5.9	Thrust vs rotation speed square . . . . .	88
5.10	Torque vs rotation speed square . . . . .	88
5.11	Input to the MAV system in pitch perturbation test . . . . .	90
5.12	Pitch angle and angular rate of the system response together with simulated response . . . . .	91
5.13	Input to the MAV system in heave perturbation test . . . . .	92
5.14	Heave velocity response of the MAV together with simulated response . . . . .	93
6.1	Detailed structure of the inner- and outer-loop layers of the flight control system	96
6.2	Simulated responses of the MAV orientation control system . . . . .	104
6.3	A single infrared Vicon camera . . . . .	105
6.4	The Vicon system setup . . . . .	106
6.5	Position reference and response of the quadrotor in full autonomous square path	107
6.6	Position reference and response of the quadrotor in full autonomous zigzag path	108
7.1	Straight path drawn in MATLAB . . . . .	120
7.2	Acceleration and velocity references generated for a straight path . . . . .	120
7.3	Square path drawn in MATLAB . . . . .	121
7.4	Acceleration and velocity references generated for a square path . . . . .	121
7.5	Circular path drawn in MATLAB . . . . .	122
7.6	Acceleration and velocity references generated for a circular path . . . . .	122
7.7	Random zigzag path drawn in MATLAB . . . . .	123

7.8	Acceleration and velocity references generated for a zigzag path . . . . .	123
8.1	The designed calligraphy brush and its holder . . . . .	126
8.2	Graphical interface for user handwriting input . . . . .	128
8.3	Split-and-merge sequence on continuous line segments . . . . .	129
8.4	User input and generated spline of vortex drawing . . . . .	130
8.5	Generated spline's acceleration of vortex drawing . . . . .	130
8.6	User input and generated spline of Chinese character <i>Guang</i> . . . . .	131
8.7	Generated spline's acceleration of Chinese character <i>Guang</i> . . . . .	131
8.8	Four MAVs writing calligraphy to the public . . . . .	133
8.9	Samples of the MAV calligraphy results . . . . .	134
8.10	Position tracking of the MAV . . . . .	135
8.11	Velocity tracking of the MAV . . . . .	136
8.12	Sequence of processing . . . . .	137

# List of Symbols

## Latin variables

$A$	Disc area or the rotor
$C_Q$	Aerodynamic torque coefficient of the propeller
$C_T$	Aerodynamic thrust coefficient of the propeller
$\bar{C}$	Damping matrix of the structure
$\mathbf{F}$	Force vector of MAV in body frame
$F$	Motor viscous friction coefficient
$\mathbf{F}_{\text{gravity}}$	Force vector in body frame generated by gravitational acceleration
$\mathbf{F}_{\text{rotor}}$	Force vector in body frame generated by rotor movements
$\mathbf{J}$	Moment of inertia of MAV fuselage
$J$	Rotor inertia
$J_x$	Rolling moment of inertia of MAV fuselage
$J_y$	Pitching moment of inertia of MAV fuselage
$J_z$	Yawing moment of inertia of MAV fuselage
$K_\Phi$	Motor's magnetic flux constant
$\bar{\mathbf{K}}$	Stiffness of the structure
$L_a$	Motor coil inductance
$\mathbf{M}$	Moment vector of MAV in body frame
$\mathbf{M}_r$	Desired moment vector of MAV in body frame
$\mathbf{M}_{\text{rotor}}$	Moment vector in body frame generated by rotor movements

$\bar{\mathbf{M}}$	Mass of the structure
$N_{i,p}(u)$	Basis function of a generally defined B-spline
$\mathbf{P}_n$	Position vector in NED frame, $[x, y, z]^T$
$\mathbf{P}_{n,r}$	Position vector reference in NED frame
$\bar{P}(\omega)$	External force to the structure in complex form
$Q_i$	Torque produced by $i$ -th rotor
$R$	Radius of the rotor
$R_a$	Motor coil resistance
$\mathbf{R}_{n/b}$	Rotational matrix from body frame to NED frame
$\mathbf{R}_{b/n}$	Rotational matrix from NED frame to body frame
$\mathbf{S}$	Lumped transformation matrix
$S_k(t)$	Spline function
$T_i$	Thrust produced by $i$ -th rotor
$T_M$	Motor's torque
$T_{j,i}(s)$	Basis function of a normalized uniform B-spline
$\mathbf{V}_b$	Velocity vector in body frame, $[u, v, w]^T$
$V_f$	Fiber volume fraction of carbon fiber-reinforced polymer
$\mathbf{V}_{n,r}$	Velocity vector reference in NED frame
$\mathbf{a}_b$	Acceleration vector in body frame
$\mathbf{a}_n$	Acceleration vector in NED frame
$\mathbf{a}_{n,r}$	Acceleration vector reference in NED frame
$a_{x,n}$	$x$ -axis acceleration in NED frame
$a_{y,n}$	$y$ -axis acceleration in NED frame
$a_{z,n}$	$z$ -axis acceleration in NED frame
$c_i$	Trajectory points to be optimized
$e$	Back EMF of motor
$f_{\max}$	Maximum allowable thrust for MAV

$g$	Gravitational acceleration
$g_1, g_2, g_3$	Gravitational acceleration components on $x$ -, $y$ -, and $z$ -axis in NED frame
$i_a$	Motor coil current
$\dot{j}_1, \dot{j}_2, \dot{j}_3$	Jerk components of the desired trajectory on $x$ -, $y$ -, and $z$ -axis in NED frame
$k_Q$	Torque coefficient
$k_T$	Thrust coefficient
$l_m$	Distance from a motor to CG of aircraft
$m$	Mass of aircraft
$p$	Body frame $x$ -axis angular rate of aircraft
$q$	Body frame $y$ -axis angular rate of aircraft
$q_0, q_1, q_2, q_3$	Variables of quaternion description
$r$	Body frame $z$ -axis angular rate of aircraft
$t_{\text{init}}, t_{\text{end}}$	Initial and final time of the trajectory
$u$	Aircraft forward velocity in body frame
$u_0, u_1, u_2, u_3$	Control inputs to MAV system
$u_n$	$x$ -axis velocity in NED frame
$u_{\text{PWM}}$	PWM input to the motor (general)
$\bar{u}$	Vibration displacement
$\bar{u}(\omega)$	Vibration displacement in complex form
$\bar{u}'$	Free vibration mode
$v$	Aircraft lateral velocity in body frame
$v_a$	Analog voltage output from the ESC
$v_n$	$y$ -axis velocity in NED frame
$v_s$	Supply voltage to the system
$w$	Aircraft vertical velocity in body frame
$w_n$	$z$ -axis velocity in NED frame
$x, x_n$	$x$ -coordinate of the aircraft in NED frame

$y, y_n$   $y$ -coordinate of the aircraft in NED frame

$z, z_n$   $z$ -coordinate of the aircraft in NED frame

### Greek variables

$\Lambda$  Combination of force and moment vectors

$\Lambda_{\text{gravity}}$  Force and moment vector generated from gravitational acceleration

$\Lambda_{\text{rotor}}$  Force and moment vector generated from rotor movements

$\Omega$  Rotational speed of rotor (general)

$\Omega_i$  Rotational speed of the  $i$ -th rotor

$\bar{\Omega}$  Rotational speed of rotor in unit 10000 rad/s (general)

$\bar{\Omega}_i$  Rotational speed of the  $i$ -th rotor in unit 10000 rad/s

$\Phi$  Flux flowing in the motor

$\Theta$  Angular vector,  $[\phi, \theta, \psi]^T$

$\delta$  Normalized input to motor (general)

$\delta_1, \delta_2, \delta_3, \delta_4$  Normalized inputs to motor 1, 2, 3, 4

$\delta_{\text{ail}}$  Normalized aileron input

$\delta_{\text{ele}}$  Normalized elevator input

$\delta_{\text{thr}}$  Normalized throttle input

$\delta_{\text{rud}}$  Normalized rudder input

$\omega$  Structure natural frequency

$\omega_b$  Body frame angular velocity vector,  $[p, q, r]^T$

$\phi$  Roll angle

$\varphi$  Latitude

$\psi$  Yaw angle

$\psi_r$  Desired yaw angle

$\rho$  Density of air

$\tau_a$  Motor electrical dynamics time constant

$\tau_m$  Motor mechanical dynamics time constant



$\tau_F$	Fixed points in the trajectory
$\tau_P$	Programmable points to be optimized in the trajectory
$\theta$	Pitch angle

### **Acronyms**

1D	One Dimensional
2D	Two Dimensional
3D	Three Dimensional
ABS	Acrylonitrile Butadiene Styrene
AHRS	Attitude Heading Reference System
CG	Center of Gravity
CMOS	Complementary Metal-Oxide-Semiconductor
COTS	Commercially Off-The-Shelf
CPU	Central Processing Unit
DARPA	Defense Advanced Research Projects Agency
DC	Direct-Current
DOF	Degree-Of-Freedom
EKF	Extended Kalman Filter
EMF	Electromotive Force
ESC	Electronic Speed Controller
FEA	Finite Element Analysis
FEM	Finite Element Method
GPS	Global Positioning System
GPU	Graphics Processing Unit
IMU	Inertial Measurement Unit
LiPo	Lithium-Polymer
LQG	Linear Quadratic Gaussian
LQR	Linear Quadratic Regulator

MAV	Micro-unmanned Aerial Vehicle
MOSFET	Metal-Oxide-Semiconductor Field-Effect Transistor
NAV	Nano Air Vehicle
NED	North-East-Down
NUS	National University of Singapore
PCB	Printed Circuit Board
PCH	Pseudo Control Hedging
PPM	Pulse-Position Modulation
PWM	Pulse-Width Modulation
RC	Radio-Controlled
RF	Radio Frequency
RPT	Robust and Perfect Tracking
UAV	Unmanned Aerial Vehicle
VTOL	Vertical Take-Off and Landing

# Chapter 1

## Introduction

### 1.1 Introduction

Unmanned aerial vehicles (UAVs) are playing major roles in tasks such as reconnaissance for search and rescue, environment monitoring, and security surveillance [66]. Their mobile capability, which is unavailable in ground vehicle, makes them an ideal platform for exploration, mapping, and monitoring tasks. Also, they are used to deliver payloads in complex three dimensional (3D) environments.

Today, they are further realized in small scale [9]. The small scale UAV, often being called the micro-unmanned aerial vehicle (MAV), can be used in narrow outdoor and indoor environments [74]. They present a minimum risk for the environment and the people living in it as compared to the normal size UAV [43, 44]. However, to realize such operations, conventional navigating systems relying on global positioning system (GPS) information are no longer sufficient. Fully autonomous operation in cities requires the MAV to fly at low altitude or indoor environments where GPS signals are often unavailable, and to explore unknown environments while avoiding collisions and creating maps [2, 20]. This involves a number of challenges on all levels: platform design, power supply, actuation, navigation, and control [22, 23, 61].

## 1.2 Literature Review

The blooming trend in developing UAV, especially for surveillance and reconnaissance missions in obstacle-rich areas which ultimately constrained the size of the aircraft, has triggered much research in the area of micro air vehicles, or MAVs. Micro-size aircraft designs become realizable as sensors and actuators are becoming smaller and smarter [75]. In 1997, the Defense Advanced Research Projects Agency (DARPA) initiated a program to develop and test MAVs for military surveillance and reconnaissance missions. According to DARPA's definition of the MAV, the maximum dimension of the aircraft in any direction should not be greater than 15 cm, the gross weight should not exceed 100 g, with up to 20 g devoted to payload, and the aircraft should be able to reach an altitudes of 100 m [31]. As a result from the emerging technologies that enable the flight of small vehicles, many institutions began investigating various MAV concepts, in the form of fixed-wing, rotary-wing (rotorcraft), and flapping-wing configurations. Although realizing a true MAV is far from success, DARPA has attempted another program to develop even smaller nano air vehicles (NAV) with a wingspan of 7.5 cm [70]. However, no NAVs meets the specifications to-date.

### 1.2.1 Platform Types

In the past decade, many variations of fixed-wing, rotorcraft, and flapping-wing flight concepts have been explored. MAVs proposed by various research teams or universities generally adopts one of these three configurations, with each being used for different purposes. Fixed-wing aircrafts require higher forward flight speeds and therefore are use in missions that cover longer distances [16]. Rotorcrafts, with its vertical take-off and landing (VTOL) and hovering abilities, are being used in navigating in complex situation such as indoor environment. Flapping-wing aircraft, if fully realized, would boast a maneuverability that is superior to both fixed-wing and rotorcraft designs because of the high wing loadings. It is, however, yet to reach the same maturity level in their development as compared to the other platforms. Fig. 1.1 to Fig. 1.3



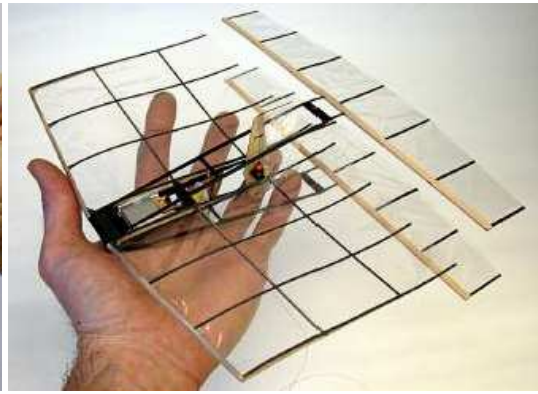
(a) Black Widow



(b) MLB Trochoid



(c) Flexible-Wing



(d) NPS

**Figure 1.1:** Examples of fixed-wing MAV: (a) Black Widow; (b) MLB; (c) Flexible-Wing; (d) NPS

show some examples of MAV in different platforms.

### Fixed-Wing

Based on the current development, the most advanced MAVs to-date use fixed-wing platform, where much work has been done by the researchers around the world [13]. A widely successful fixed-wing MAV, Black Widow is developed by AeroVironment as a part of DARPA's MAV initiative [25]. It has a 15 cm (6 in) wingspan. This platform was designed to deliver real-time images via a custom-made camera and transmitter. The Black Widow claimed to be of fully autonomous. Its avionics include a two-axis magnetometer to sense compass heading, pressure sensors to sense altitude and dynamic pressure, a piezoelectric gyro for angular rate

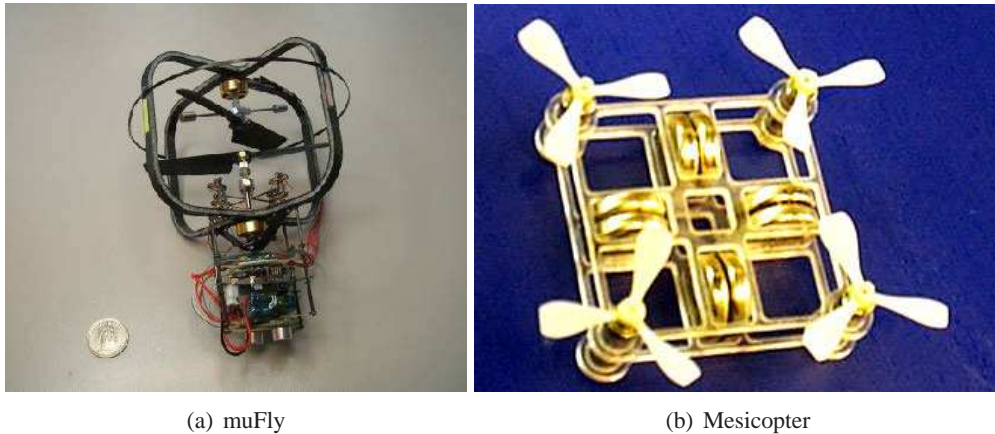


**Figure 1.2:** Examples of rotary-wing MAV: (a) muFly; (b) Mesicopter

measurement, a command uplink receiver (2 g), a flight computer which consists of two microprocessors, and customized control actuators (0.5 g). In order to deliver live color video images, it was installed with a commercially off-the-shelf (COTS) video transmitter and a COTS black/white complementary metal-oxide-semiconductor (CMOS) camera (total of 5.5 g) which then were modified into a custom video transmitter and a custom color CMOS camera (total of 3.1 g). Overall, it has a total mass of 80 g and flight endurance of 30 minutes.

Other than the Black Widow, there are several other popular examples such as MLB Trochoid, NPS MAV, and Flexible-Wing. The MLB Trochoid had a 20 cm wingspan and was able to fly for 20 minutes at speed up to about 100 kph (60 mph) [50]; the NPS MAV, measures 25 cm in wingspan and weighed 12.4 g [68]; and the Flexible-Wing MAV from the University of Florida with wingspan of 16 cm, which is slightly above the requirement set by DARPA [3]. In general, due to the wing loading requirement for all fixed-wing aircraft, the size of the wingspan has to be much larger than other platforms.

### Rotory-Wing

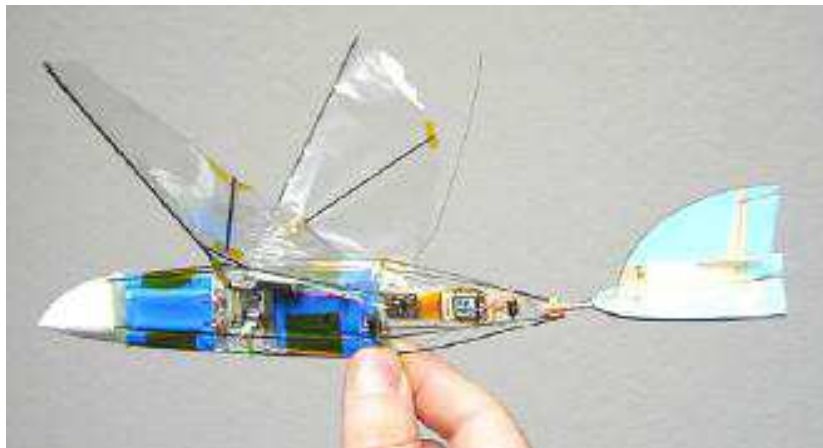
Other than the fixed-wing MAV, rotorcraft is currently one of the main platforms many researchers preferred, due to its VTOL and hovering abilities [48]. A co-axial MAV codenamed



(a) Nano Hummingbird



(b) Entomopter



(c) MicroBat



(d) DelFly

**Figure 1.3:** Examples of flapping-wing MAV: (a) Hummingbird; (b) Entomopter; (c) MicroBat; (d) DelFly

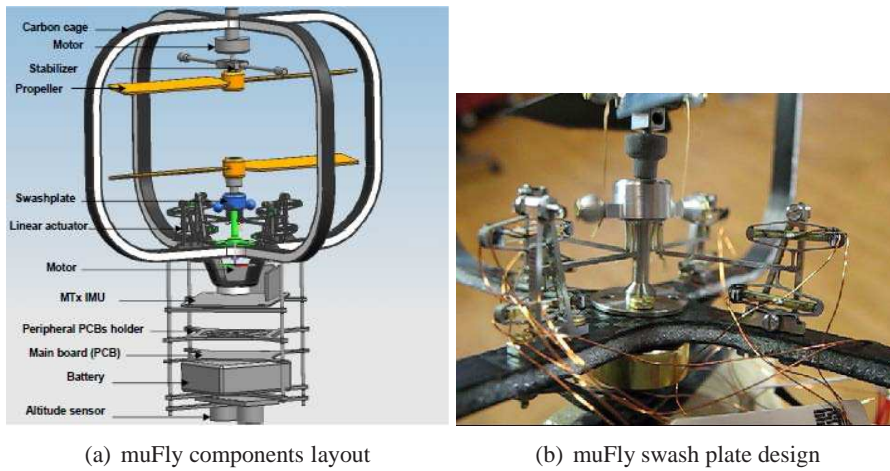


**Figure 1.4:** muFly MAV: (a) its components layout; (b) its swash plate design

muFly was built by a research team in ETH Zurich in 2007 [67]. MuFly was designed to carry out fully autonomous flight in a dimension of 12 cm rotor diameter, with the weight of 77 g in total. It has a flight time of about 4 minutes. The mechanical structure of muFly MAV is different from the usual co-axial platform. The rotors are controlled by two different motors without gears, while the lower rotor is attached to a swash plate controlled by four linear actuators. As shown in Fig. 1.4, the avionic system of muFly consists of an inertial measurement unit (IMU), a sonar range sensor, and two customized printed circuit boards (PCBs). The research team from ETH has also included an omni-directional camera for navigation in their later prototypes, resulting in a bigger dimension of MAV which weighted 90 g.

Another famous example of rotorcraft MAV is the Mesicopter by Stanford University. It has an impressive total weight of 3 g, with a quadrotor platform. It was, however, never able to lift the weight of its own energy source due to the inefficient design of the rotor blades [39].

### Flapping-Wing

Recently, being inspired by how insects and birds navigate, many research teams have started their development of MAV by adopting to this natural flapping-wing platform [4]. The most successful example so far would be the Nano Hummingbird MAV developed by AeroViron-



ment [1]. It was claimed to be the world's first successful flight of the smallest self-powered, rudderless aircraft with flapping wings [32,62]. This MAV is modeled after hummingbird, and at current development, it is able to hover, take-off/landing, flying in forward and lateral direction under remote control. It is weighted 19 g including a power supply last up to 8 minutes flying time, with a wingspan of 16.5 cm (6.5 in). Unlike the conventional rotorcraft and fixed-wing, the mechanical structure of flapping-wing MAV, are usually designed according to control requirements. As such, the Nano Hummingbird MAV operates by using only two flapping wings with each of them attached to a direct current (DC) motor, functioning as rudder, elevators, ailerons, and engine. Besides the motors, the bot carries a video camera, communication modules, and a battery.

Other successful examples are the Microbat by AeroVironment, 23 cm wingspan with 12.5 g weight, which has an endurance of 22 minutes under remote control [17]; and DelFly Micro with an impressive 10 cm wingspan and 3 g weight [19].

### **1.2.2 Challenges on Flight Control**

Generally, MAV control can be stratified into two levels: mission control and flight control. Mission control operates the payload on the MAVs to accomplish certain tasks, while flight control takes care of the stabilization of the aircraft. In the other words, it is to fly the aircraft autonomously like what radio-controlled (RC) modelers have done.

In the current literature, no MAV has achieved a true mission autonomous flight. Most of the autonomous control discussed is referred to the flight control alone, or just the aircraft attitude stabilization. As a result, experienced pilots are needed to gain the high level control of the MAV for guidance and navigation. This, however, is impractical as the MAV will be out of the pilot's sight beyond certain range. To overcome the line-of-sight problem, the inclusion of an on-board camera was first demonstrated in the AeroVironment's Black Widow, where it can be remotely piloted by observing the live images transmitted to the ground station. However, since most of the MAV cannot carry on-board transmitters powerful enough to allow tele-operation,

many researchers have focused on developing a fully autonomous MAV. An example which has been designed from its inception as a fully autonomous MAV, is the Entomopter originally developed at the Georgia Institute of Technology under a DARPA contract [49].

In an ideal situation, the MAV should be able to attend their mission regardless of weather conditions. Here, stability and control of MAVs pose a great concern to the researchers due to the lack of power, mass, or control surface area to fly in extreme environments such as with turbulence and wind gusts. A simple solution to minimize the effect of local wind gusts would be flying at a higher velocity. This, however, makes them less useful in certain close-in reconnaissance. On top of that, the fixed-wing configuration is susceptible to roll perturbations. Even if it is flown by a ground pilot, roll stability augmentation is needed. As for the flapping-wing platform, flapping flight is more complicated than any other aircraft due to the high nonlinearity of the flapping wings. In such a platform, it is necessary to combine the wing structures and flight controls to perform the desired maneuvers. In brief, flight control of MAVs presents more challenges, which involves all motion and air data sensors, flight actuators and control surfaces, even mechanical structures, all driven by an automatic pilot and the flight control system [27].

In order to build an aircraft system with higher degree of autonomy, increasing demands are being placed on the hardware and software that comprise the guidance and control system. As the aircraft becoming more autonomous, guidance and control systems must support advanced functions such as automated decision making, obstacle avoidance, target acquisition, target tracking, artificial vision, and interaction with other manned or unmanned systems [60,73]. The acceptable form factors of these systems are decreasing, at the same time performance requirements are also increasing. Current miniaturization techniques may accommodate these changes, however, the main challenge is still presented in the processor speed and storage capacity. Currently, it is believed that advances in software technology have the potential to revolutionize the control system design.

For flight control, it is common to divide the control problem into an inner loop that controls attitude and an outer loop that controls the translational trajectory of the aircraft [46]. At

the lowest level, inner loop flight control is simply to maintain the vehicle in the correct orientation (roll, pitch, yaw) while maneuvering through environmental perturbations such as wind and precipitation [72]. Therefore, its reference is either a gyroscopic reference, integrated accelerometers, or external passive (infra-red sensor), or active (radar/sonar sensor) cues. For the outer loop control, GPS is an ideal reference so long as it is available. However, GPS-reference control system has its limitation as GPS signal is unavailable in indoor environment, or it may be denied on the battlefield. For very small MAVs, the ability to carry an efficient GPS antenna is not possible because the vehicle itself falls well below the wavelength aperture of the L1 and L2 GPS frequencies (1575.42 MHz and 1227.60 MHz, respectively, or about  $\lambda = 22$  cm) [15].

Many control methods have been applied to MAVs, in either simulation or actual implementation [52]. Dynamic inversion and neural-network-based adaptations have been used to improve the performance of the attitude control systems [18], and a pseudo control hedging (PCH) method has been used to protect the adaptation process from actuator limits [34]. This results in the introduction of adaptation to uncertainty in the attitude and the translational dynamics to minimize the effects of flight control model error in all six degree-of-freedom (DOF), and thus leading to a more accurate position tracking. Optical flow sensing is a technique that allows a moving observer to sense the proximity of its surroundings and its relative motion. It becomes another control technique that has gained popularity since the advent of MAVs [65]. The method was motivated by how some insects, such as the honey bee, observe the bilateral flow of objects in their field of view in order to assess their speed and trajectory relative to objects [26]. Besides, vision-based state estimation and some commonly used control techniques such as PID, linear quadratic gaussian (LQG), feedback linearization, backstepping, are all evaluated on MAVs [21, 30, 76].

Regardless of the flight control methods employed, the ultimate result must be a system capable of responding to the high bandwidth maneuvering requirements posed by the MAV's mission. For instance, in the indoor flight scenarios, they must be able to sense and react to avoid disaster in an obstacle-rich environment. Relative to the speed of flight, the on-board

<b>Parts</b>	<b>Weight Portion</b>	<b>Weight (g)</b>
Hardware system	40%	20
Electronics	30%	15
Power supply	30%	15
Total	100%	50

**Table 1.1:** Target weight distribution of the MAV

sensors must be able to detect obstacles and provide enough time for the control system to re-plan the trajectory [37]. The system has to then command actuators that are able to follow the commanded path before collision occurs. These dynamics are one of the most challenging control problems for any flight vehicle. Given that MAVs can be controlled by fully autonomous means, significant test and evaluation issues continue to exist [8].

### 1.3 Thesis Outline

The major aim for this thesis is to develop MAVs which are capable of full autonomous flight in indoor environments. According to the literatures, well developed fully autonomous air vehicles for indoor navigation are rather large in size (above 30 cm diameter), which ultimately fall out from the MAV definition set by DARPA. While small scale MAVs which satisfy the requirements are widely available, most of them has limited autonomy due to the size limitation.

This thesis aims to develop small scale autonomous MAVs starting from structural analysis and design, followed by avionic circuit board customization. A model based control methodology is also included to achieve different autonomous performance based on the applications. Power supply is also needed to power the entire MAV for 8 minutes flight. The targeted weight of the MAV is set as 50 g, while largest dimension below 15 cm. The proposed weight distribution of the MAV systems is shown in Table. 1.1.

This thesis is divided into 9 chapters. This chapter introduces the state-of-the-art UAVs and the aim of this thesis in developing fully autonomous MAVs. Chapter 2 discusses the platform selection criteria. Chapter 3 highlights the importance of finite element analysis on different

aircraft structure to obtain an aircraft frame that is free from potential vibration problems while maintaining its low weight. A guideline to design MAV avionics circuit board is proposed in Chapter 4 to integrate the essential sensors and processors. Chapter 5 details the derivation of the dynamics model of the MAV systems, together with suggested methods to identify its parameters. Controller design on the identified MAV model is discussed in Chapter 6, followed by flight trajectory generating algorithm based on minimum jerk optimization in Chapter 7. An application of the MAV and its realization are discussed in Chapter 8. Finally, concluding remarks and projected future work are discussed in the last chapter.



## Chapter 2

# Platform Selection

### 2.1 Introduction

In general, based on current review on the market discussed in Chapter 1, there are three main aircraft platforms to be considered: the rotary-wing (Fig. 2.1); the fixed-wing (Fig. 2.2); and the flapping-wing (Fig. 2.3). Besides these conventional platforms, there are also various unconventional platforms including tail-sitter aircraft and rolling-wing platforms. However, these platforms are mainly developed to achieve specific flight mission such as having both the abilities of vertical take-off and long range cruise flight. As a result, these unconventional platforms will not be considered in the design of the MAV.

Rotary-wing aircraft can be further broken down into three different types: the single-rotor vehicle, also known as helicopter (Fig. 2.1(a)); the co-axial rotorcraft (Fig. 2.1(b)); and the multi-rotor vehicle, with quadrotor (Fig. 2.1(c)) dominating this type of platform currently.

In this chapter, five aforementioned platform types (fixed-wing, flapping-wing, helicopter, co-axial, and quadrotor) will be considered and discussed according to the proposed specifications. They will be evaluated based on their maneuverabilities, weight and size factors, and the complexity of the platforms.



(a) Single-rotor helicopter



(b) Co-axial helicopter



(c) Quadrotor

**Figure 2.1:** Rotary-wing platforms





**Figure 2.2:** Fixed-wing platform



**Figure 2.3:** Flapping-wing platform

## 2.2 Maneuverability

Requirement for aircraft maneuverability is strongly constrained by the surrounding environment. Most of the applications of the proposed MAV are indoor related, as its proposed size and weight allow it to navigate freely even in a cluttered indoor environment. Also, the aircraft must be fully controllable for its 6 DOF motions, i.e.,  $x$ -,  $y$ -,  $z$ -translation and rotation. Furthermore, the platform must also be easy to operate for a human pilot. Thus, it requires the platform to have high control margin at its hovering state with a certain payload.

Although having quick responses, the fixed-wing aircraft is, however, not suitable for indoor missions. A fixed-wing aircraft has no fixed-point hovering ability which is very important or essential for indoor navigation. Also, it generally needs a huge turning radius to change its heading direction, thus it is not recommended to maneuver in an obstacle rich environment.

The signatures of all rotary-wing platforms are the ability to take-off vertically and hover at a fixed point. Particularly, helicopters and quadrotors are well-known for their agility maneuverability in confined space. Although such aggressive movements are not essential in indoor navigation, the high maneuverability bandwidth makes such platforms the ideal candidates for MAV development.

Besides the rotary-wing, flapping-wing aircrafts are also ideal for guidance and navigation in buildings with cluttered obstacles. Like the helicopter, the flapping-wing has high maneuverability at any direction of flight. However, the technology of such a platform is yet to be mature enough to operate in practical cases today.

## 2.3 Size and Weight

According to the criteria set by DARPA on MAV, it has to be lighter than 100 g, with a largest dimension of 15 cm. With these stringent restrictions on both the size and weight of the MAV, the platform choices are limited.

For rotary-wing platforms, conventional helicopter loses its advantage in terms of size factor

as a tail-rotor is always needed to compensate yaw reaction torques. To shorten its tail, the main rotor needs to reduce its size, resulting in a lower payload budget. On the other hand, with the contra-rotating main rotors sharing the same shaft, the co-axial platform has its advantage in the size factor as a tail-rotor is no longer needed. As for a quadrotor, due to its highly symmetry design, it can be shrunk or expanded depending on the payload of the platform. This makes it another suitable candidate to develop MAVs.

In literature, the smallest platforms with the lowest weight are not the rotorcraft, but the fixed-wing and flapping-wing platforms. These platforms gain their lift forces from the wings, which are usually made from lightweight materials. However, as the lift generated by the wings are either through airfoil (for fixed-wing) or flapping motion (for flapping-wing), it is generally weaker as compared to the lift generated by the rotating propellers of the rotary-wing platform. As their wings area get further restricted due to the size constraint, the lifting force produced by them will be lowered. This ultimately restricts the payload of the platform, which is not desired in the MAV design.

## **2.4 Structure Complexity**

Complexity of the platform structure will result in complicated aerodynamics during flight. This will in turn complicates the controller design of the aircraft as the aerodynamics of the aircraft need to be taken care of. A simple structure with straight forward working principle is desired.

Among the selected platforms, flapping-wing has the most complicated aerodynamics during flight. With only a pair of wings and a tail rudder control surface, a flapping-wing platform is an under-actuated system and thus can only be controlled in less than six DOF. For flapping-wing to achieve full six DOF control, it needs to be modified mechanically to a more complex structure.

On the other hand, fixed-wing aircraft has the simplest and mature structure, with aileron control surfaces on its wings, rudder and elevator control surfaces on its tail. It is one of the



**Figure 2.4:** Changes in collective pitch of the blade

ideal candidates in terms of structural complexity.

For rotary-wing, both helicopter and co-axial need collective pitch to control the direction of travel (see Fig. 2.4). Current state-of-art collective pitch control mechanism uses a swash plate attached with two to three servo motors as control inputs. The upper body of the swash plate will be linked to the blades and spin together with them, while the lower body of the swash plate stays at certain desired orientation (Fig. 2.5). The swash plate complicates the MAV mechanical design, and introduces extra unmeasurable states to the vehicle dynamics in the control point of view. The other type of rotary-wing platform, the quadrotors, utilize four fixed pitch blades without the need of any swash plate. The direction of motion of such vehicle is solely controlled by the combination of different rotating speed of the motors. Such a simple mechanical structure and working principle of the quadrotor will also ease up the miniaturization work.

## 2.5 Summary

A summary of the discussion can be seen in Table 2.1. According to the advantages shown on each requirement, a quadrotor platform appears to be the best candidate to realize the proposed MAV system design. The quadrotor has high maneuverability as it can take-off and land vertically, hover, and even to perform agility movements. It can be shrink down easily to small and light while maintaining its core structure and working principle. It has also one of the simplest



**Figure 2.5:** A swash plate of a small scale RC helicopter

	<b>Maneuverability</b>	<b>Size</b>	<b>Structure Complexity</b>
<b>Fixed-wing</b>	Not suitable due to large turning radius	Small but low payload	Simple
<b>Flapping-wing</b>	Good	Small but low payload	Complex
<b>Helicopter</b>	Good	Large due to tail-rotor	Complex
<b>Co-axial</b>	Good	Small	Complex
<b>Quadrotor</b>	Good	Small	Simple

**Table 2.1:** Advantages and disadvantages of each platform

structure among the aircrafts. The system design of the MAV will be realized on a quadrotor platform.



## **Chapter 3**

# **Airframe Design**

### **3.1 Introduction**

The restriction in size of the MAVs has several implications on their performance capabilities. One of them is the structural stability of the aircrafts. In general, a small-scale model is structurally weak and vulnerable to variety of potential structural vibration problems especially the structural resonance. In this condition, the vibration amplified to a maximum amplitude when forcing frequency matched the natural frequency of the structure.

For a small-scale quadrotor platform, slender bodies such as the quadrotor arms are typically susceptible to this harmful threat. This excessive vibration is more likely to occur as the frame is made of composite materials which are much lighter. Therefore, the quadrotor frame needs to be carefully designed to avoid any potential structural natural frequencies within the range of quadrotor operating speeds.

### **3.2 Material**

After careful consideration on the material of the main body frame, carbon fiber-reinforced polymer appears to be one of the optimum choice as it has high tensile strength-to-weight ratio.

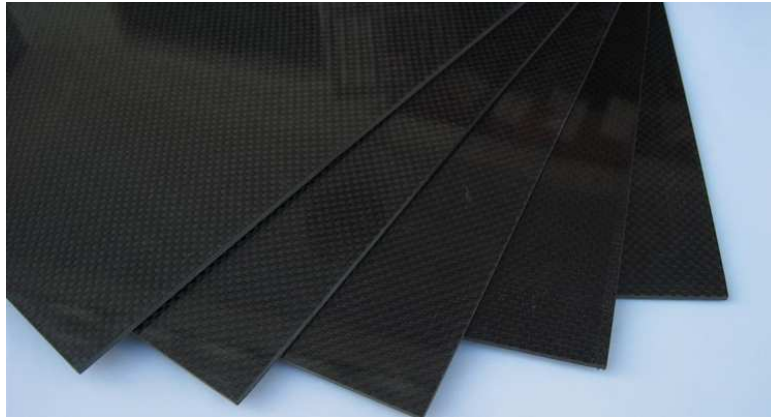


**Figure 3.1:** Carbon/epoxy T300/5208

It is also used extensively in aerospace and automotive field.

Two typical types of carbon fiber used in the aerospace industry are the bi-directional plain weave carbon fiber and the uni-directional carbon fiber.

### **3.2.1 Bi-Directional Plain Weave Carbon Fiber**

The bi-directional plain weave carbon fiber (Fig. 3.1) is the most commonly selected fabric style for lightweight aerodynamic parts. It delivers uniform strength in both horizontal and vertical directions, which is ideal for most flat or slightly curved applications. To maximize its strength properties, each carbon fiber layer can be added at an alternating 45 degree angle during the lay-up process.

The material properties of this material depends on the types of carbon and its epoxy. According to [63], the bi-directional plain weave composite made of carbon and epoxy of type T300 and 5208 respectively, with fiber volume fraction,  $V_f$ , of 0.4, has the material properties shown in Table 3.1.

### **3.2.2 Uni-Directional Carbon Fiber**

Unlike the bi-directional plain weave composite, the uni-directional carbon fiber (Fig. 3.2) is extremely stiff on one direction while relatively weak on the other direction. It can be used



Description	Unit	Value
In-plane Young's modulus	GPa	53.1
Out-of-plane Young's modulus	GPa	8.0
In-plane Poisson ratio		0.055
Out-of-plane Poisson ratio		0.074
In-plane Shear modulus	GPa	3.79
Out-of-plane Shear modulus	GPa	3.70
Density	kgm <sup>-3</sup>	1465

**Table 3.1:** Material properties of bi-directional plain weave carbon/epoxy T300/5208



**Figure 3.2:** Carbon/epoxy T300/976

for a variety of applications such as aircraft and rocket fuselages with long body parts. In the quadrotor fuselage design, it is especially useful for quadrotor arms design.

The material properties of the uni-directional carbon and epoxy of type T300 and 976 is shown in Table 3.2 [38].

### 3.3 Vibration Analysis Formulation

Once the material of the platform is selected, vibration analysis will be carried out to determine a suitable size and shape of the structure. Limited by the requirement for MAVs, the quadrotor

<b>Description</b>	<b>Unit</b>	<b>Value</b>
Young's modulus along grain	GPa	135.2
Off-grain Young's modulus	GPa	9.24
Poisson ratio along grain		0.32
Shear modulus along grain	GPa	6.28
Density	kgm <sup>-3</sup>	1480

**Table 3.2:** Material properties of uni-directional carbon/epoxy T300/976

arms length are bounded to a maximum of approximately 7 cm, while due to the vibration caused by the rotating rotors, the natural frequencies of the structure need to be higher than the maximum rotating frequency. Thus, analysis is carried out to fulfill the two requirements stated above.

In this section, mathematical formulation of the vibration analysis will be derived. It includes the natural mode analysis which calculates the natural frequencies of the material, and the frequency response analysis which shows the amplitude and frequency of the vibration due to oscillating load.

### 3.3.1 Natural Mode Analysis

For a full system, the natural mode analysis, also known as the free vibration analysis, is a vital preliminary study in order to investigate the vibrational characteristics of the structure. For normal mode analysis, there are no external forces that act on the system and hence the equation of motion is presented in [14] as

$$\bar{\mathbf{M}}\ddot{\bar{\mathbf{u}}} + \bar{\mathbf{K}}\bar{\mathbf{u}} = 0, \quad (3.1)$$

where  $\bar{\mathbf{M}}$  and  $\bar{\mathbf{K}}$  are mass and stiffness matrices of the structure. Also, the term  $\bar{\mathbf{u}}$  and  $\ddot{\bar{\mathbf{u}}}$  are the displacement and acceleration of the system. As the full system is constructed, Equation (3.1) is then solved in order to obtain the natural frequencies,  $\omega$ , and the modes,  $\bar{\mathbf{u}}'$ , of the free vibration

for a structure. For free vibrations, a general solution is in the form of

$$\bar{u} = \bar{u}' \cos \omega t, \quad (3.2)$$

and thus Equation (3.1) becomes

$$[\bar{\mathbf{K}} - \omega^2 \bar{\mathbf{M}}] \bar{u}' = 0. \quad (3.3)$$

By replacing the  $\omega^2 = \lambda$ , we have

$$[\bar{\mathbf{K}} - \lambda \bar{\mathbf{M}}] \bar{u}' = 0, \quad (3.4)$$

which is commonly known as the general matrix eigenvalue problem. Using the existing method among eigensolution techniques, one may obtain the solution by solving  $\det[\bar{\mathbf{K}} - \lambda \bar{\mathbf{M}}] = 0$  where the roots (also called eigenvalues),  $\lambda_i$ , for  $i = 1, 2, \dots$  can be calculated. Subsequently, the corresponding eigenvectors,  $\bar{u}'_i$ , can be computed once the eigenvalues are found.

### 3.3.2 Frequency Response Analysis

For complete structural model, the equation of motion in Equation (3.1) can be extended and presented as [14]

$$\bar{\mathbf{M}}\ddot{\bar{u}} + \bar{\mathbf{C}}\dot{\bar{u}} + \bar{\mathbf{K}}\bar{u} = \bar{P}(\omega)e^{j\omega t}, \quad (3.5)$$

where  $\bar{\mathbf{C}}$  is the damping matrix and  $\dot{\bar{u}}$  is the velocity of the system. Meanwhile,  $\bar{P}(\omega)e^{j\omega t}$  is a vector of external forces in complex form. The forces can be real or imaginary, or both. Assuming the harmonic motion of the system, harmonic solution can be expressed as

$$\bar{u} = \bar{u}(\omega)e^{j\omega t}, \quad (3.6)$$

where  $\bar{u}(\omega)$  is a complex displacement vector. Thus, the first and second derivatives are presented as

$$\dot{\bar{u}} = j\omega\bar{u}(\omega)e^{j\omega t}, \quad (3.7)$$

$$\ddot{\bar{u}} = -\omega^2\bar{u}(\omega)e^{j\omega t}. \quad (3.8)$$

Substituting them into the equation of motion, gives

$$[-\omega^2\bar{\mathbf{M}} + j\omega\bar{\mathbf{C}} + \bar{\mathbf{K}}]\bar{u}(\omega) = \bar{P}(\omega), \quad (3.9)$$

which can be solved as matrices  $\bar{\mathbf{M}}$ ,  $\bar{\mathbf{C}}$ , and  $\bar{\mathbf{K}}$  are known. Thus, the displacement response can be determined according to the load  $\bar{P}$  for a specific forcing frequency.

### 3.4 Finite Element Analysis

Although closed-solutions can be obtained, analytical methods to solve the vibration frequencies and amplitudes are impractical in the platform design process. As the platform may consist of multiple irregular shape structures, numerical approach to find solution by utilizing commercial softwares will be more accurate and efficient. Finite element analysis (FEA) is a numerical approach in solving structural problems. The main idea of finite element method (FEM) is to discretize the problem where the domain to be analyzed is divided into a number of discrete elements. Using this approach, it offers great flexibility to model complex geometries which would be impossible by taking analytical approach. Therefore, the MSC Nastran, one of the most widely used FEA commercial software is utilized in the design of the micro quadrotor platform.

Nastran is a useful tool which simulates static and dynamic cases for a wide variety of complicated structural problems. Therefore, the real structural behavior of the model can be examined. Accompanied with Nastran, modeler software called MSC Patran is employed for

finite element modeling. Patran provides geometry modeling, meshing, boundary condition and material properties setup for Nastran. It is also used for post-processing purpose. The process of modeling and simulation using Patran and Nastran is illustrated in Fig. 3.3. Provided in Nastran, Lanczos method is utilized for eigenvalues and eigenvectors extraction purpose.

To simulate the quadrotor platform in a systematic way, single arm and full configuration model are constructed in Patran with composite material assigned before Nastran is used to investigate the structural resonance. In corresponding to this research, the study is concentrated on natural mode analysis to determine the natural frequencies and mode shapes of the model, then the frequency response analysis will be simulated based on the results. The natural mode analysis leads to the prediction of resonance for the structure and the type of resonance that may occur. Meanwhile, the displacement response of the model can be determined using frequency response analysis when external steady-state oscillatory excitation is applied.

### **3.5 Case Study**

Two case studies were conducted. The first case studies the single arm configuration, followed by the second case, the full quadrotor configuration. In the simulation, the structures will be tested for the normal mode and the frequency response analysis. In an effort to explore the suitable structure for the quadrotor arms, models with five different cross-sections were tested. The cross-sections are the commonly used rectangular, rectangular hollow, circular hollow, T shape and N shape. The geometry of the cross-sections are showed in the Fig. 3.4. As the force of the system exerts only on the tip of the beam, uni-directional carbon fiber with fiber direction parallel to the beam is utilized. the material used in the structural analysis is the uni-directional carbon/epoxy T300/976 which has been discussed in the previous section.

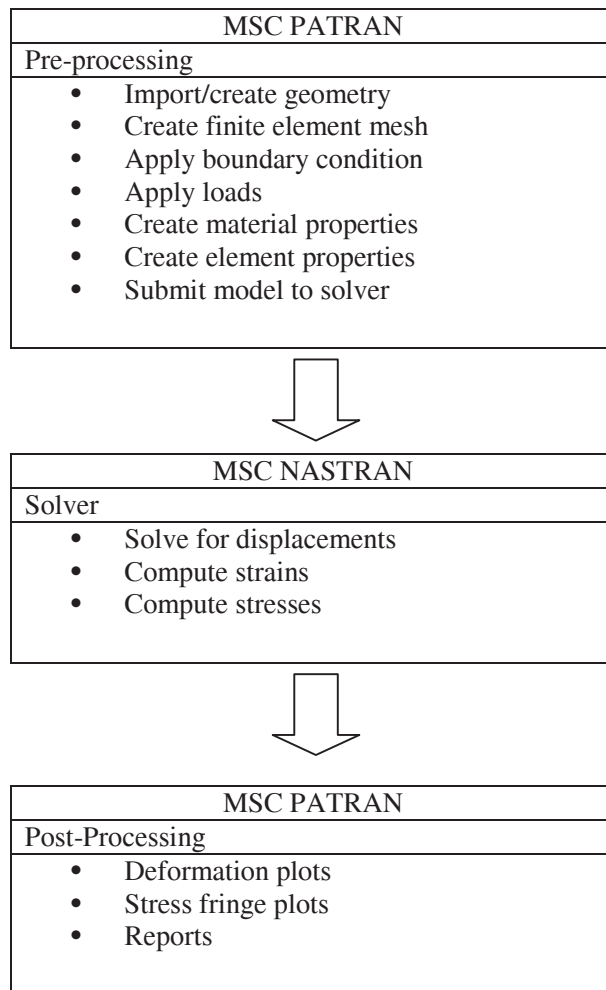


**Figure 3.3:** Modeling and simulation process using MSC Patran and Nastran

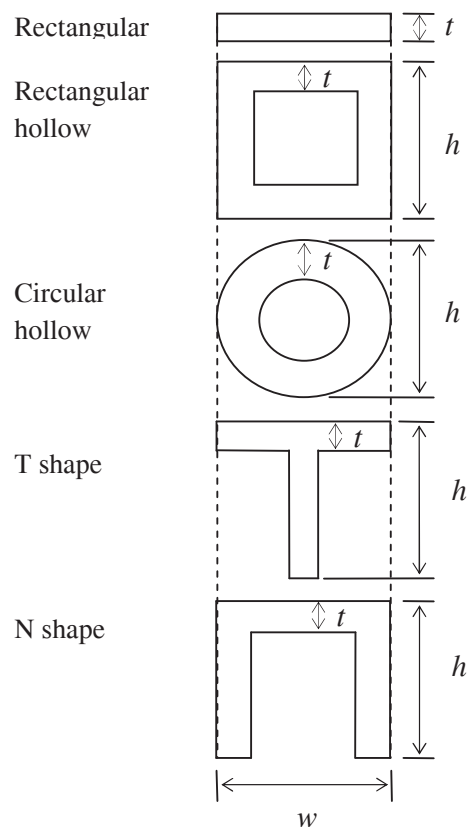


**Figure 3.4:** Cross-section of beams

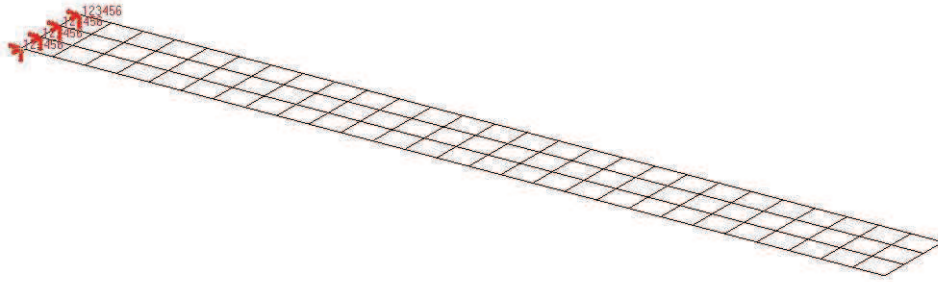


**Figure 3.5:** Thin plate model in MSC Patran

Length (mm)	Frequency (Hz)			
	Mode 1	Mode 2	Mode 3	Mode 4
50	614.60	3656.7	3803.4	10518
60	426.85	2546.1	2642.6	7313.4
70	313.62	1873.6	1942.1	5377.1
80	240.30	1437.1	1491.3	4137.1
90	189.73	1135.4	1175.3	3255.4
100	153.68	920.14	952.05	2637.5

**Table 3.3:** Natural frequencies of thin plate with varying length

### 3.5.1 Single Quadrotor Arm

It is well known that slender bodies are more easily exposed to vibration. Thus, shorter structure is stiffer and this is proven in the simulations using Nastran. Here, thin plates (Fig. 3.5) with varying length between 50 mm to 100 mm are tested. In Patran, the thin plate model is built using two dimensional (2D) four-node quad elements with material orientation of  $[450, -450, 0]$ . Using the models constructed, the normal mode analysis is conducted via Nastran. For this analysis, the discrete element employed has six DOF per node and all nodes at the one of the tip are assumed to be fixed. In Table 3.3, summary of the Nastran analysis results obtained for this study is given.

Based on the simulation results, it is evident that the natural frequencies for all first four mode increased as the structure is shorter. Therefore, shorter model is preferable to form the quadrotor arm. Further study is then directed to the other models with different cross-section.



Type of Cross Section	Weight (g)	Frequency (Hz)	
		Mode 1	Mode 2
Rectangular	0.5328	426.85	2546.1
Rectangular hollow	1.7760	3032.4	17318
Circular hollow	1.3949	2647.9	15624
T shape	0.9768	1902.8	2622.7
N shape	1.4208	2717.5	3215.6

**Table 3.4:** Natural frequencies of beam with different cross-sections (1 mm thickness)

Following the defined cross-sections, the models are again constructed in Patran. Here, the model for each cross-section was constructed with length  $a = 60$  mm, width  $w = 6$  mm, height  $h = 6$  mm and thickness  $t = 1$  mm. By following the similar procedure for normal mode analysis, the natural frequencies for the first two modes are tabulated in Table 3.4.

It is noted that rectangular shaped beam has the lowest natural frequencies for the first two modes among the five. For the first mode, the natural frequencies for open shape (T shape and N shape) beams are comparable to those with closed shape (rectangular hollow and circular hollow). Meanwhile, the natural frequencies for closed shape beam are much higher in mode 2 with 17318 Hz and 15624 Hz for rectangular hollow and circular hollow beams. Overall, models with closed shape cross-sections have higher natural frequencies, thus they are more rigid. Using similar approach, the simulation is repeated for beams with thickness,  $t = 0.5$  mm and the natural frequency results are shown in the Table 3.5. In this case, the weight of the beams is greatly reduced (between 45 to 50%) while maintaining the relatively high natural frequencies. These results show that in most of the shape that has been experimented, decreasing the thickness of the beams will cause low effects on the natural modes of the structure. The resulted mode shapes for the first two modes for these five shaped beam are illustrated in Fig. 3.6-3.10.

Referring to Table 3.4 and 3.5, one can notice that in general, the beam having a closed cross-section shape, i.e., rectangular hollow and circular hollow, has better natural modes as they have much higher natural frequencies compared to others. A more detailed study is conducted on the effect of cross section geometry variation toward the performance of the beam. Next, the effects of width and height of these selected beams are investigated.

Type of Cross Section	Weight (g)	Frequency (Hz)	
		Mode 1	Mode 2
Rectangular	0.2664	213.45	1322.5
Rectangular hollow	0.9768	3270.7	18312
Circular hollow	0.7670	2851.6	16495
T shape	0.5106	1845.3	2713.2
N shape	0.7548	2810.4	3458.7

**Table 3.5:** Natural frequencies of beam with different cross-sections (0.5 mm thickness)

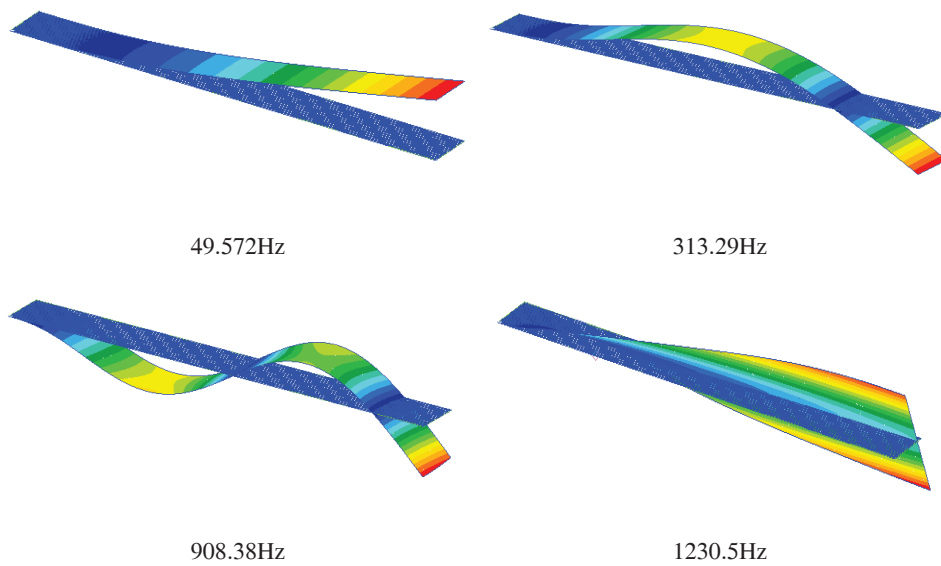


**Figure 3.6:** Mode shape for rectangular shaped beam

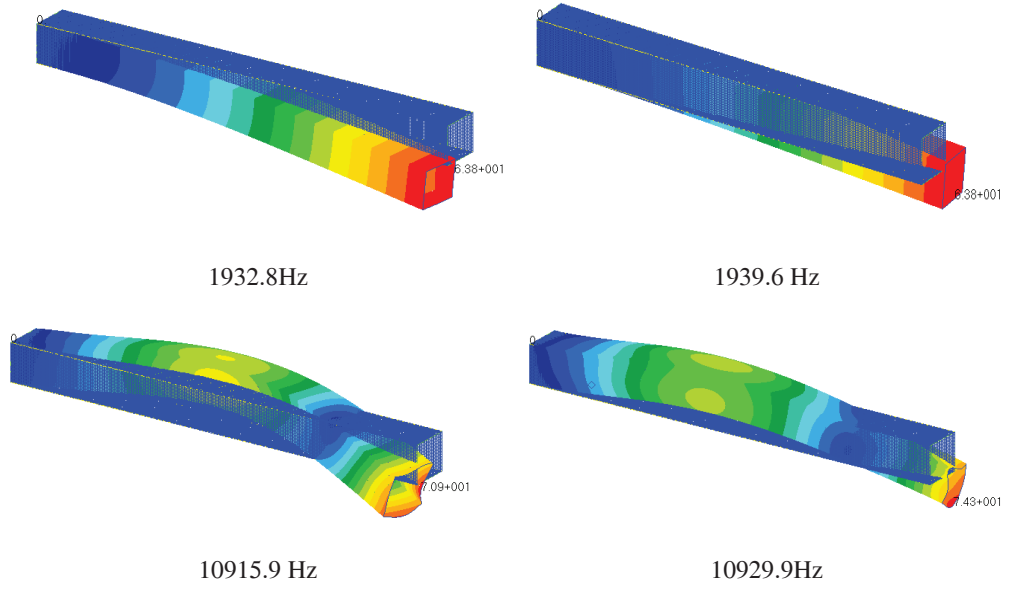


**Figure 3.7:** Mode shape for rectangular hollow shaped beam

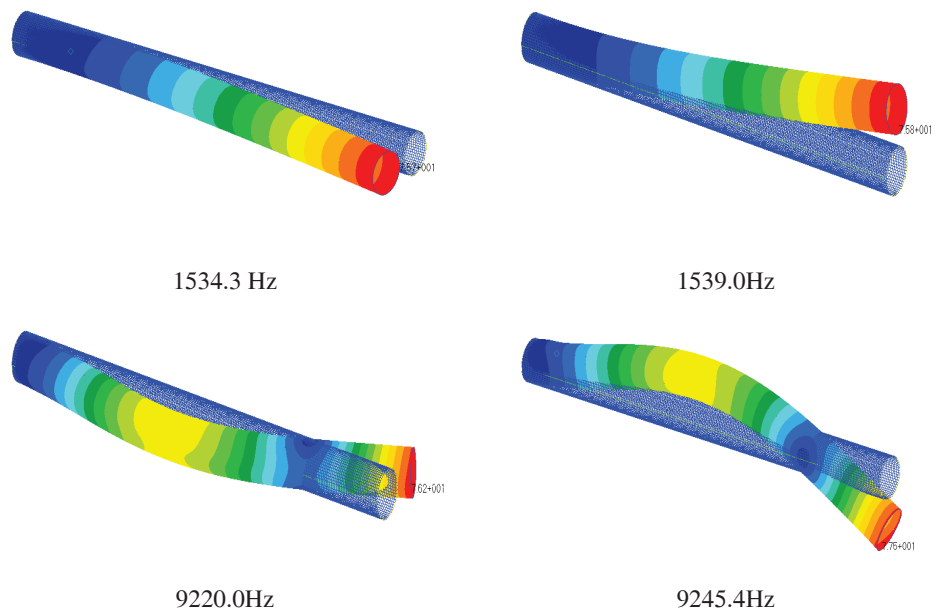


**Figure 3.8:** Mode shape for circular hollow shaped beam

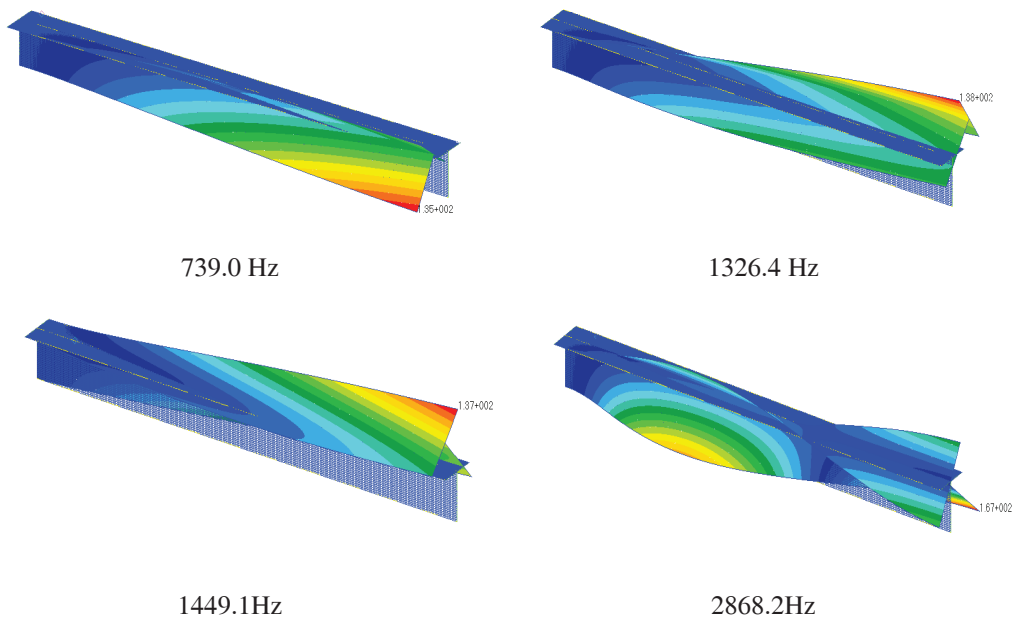


**Figure 3.9:** Mode shape for T shaped beam

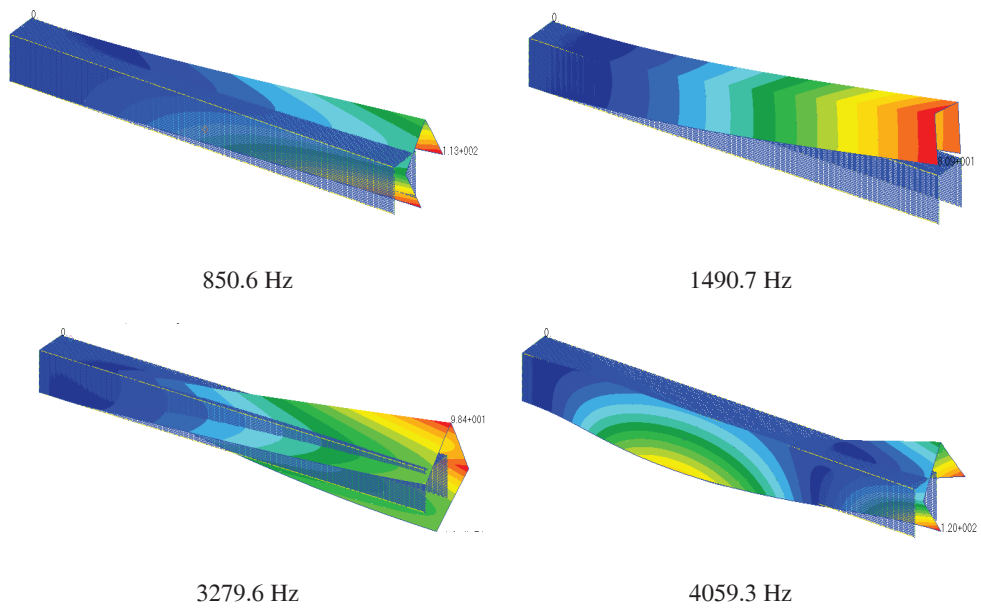


**Figure 3.10:** Mode shape for N shaped beam

Height (mm)	Width (mm)	Frequency (Hz)	
		Mode 1	Mode 2
3	3	1538.5	1538.5
3	4	1588.9	2036.4
3	5	1625.9	2515.8
3	6	1651.8	2979.7
3	7	1670.3	3430.8
3	8	1683.5	3871.3
3	9	1693.0	4302.7
3	10	1699.4	4725.6
4	6	2218.0	3105.6
5	6	2756.0	3199.4
6	6	3270.7	3270.7

**Table 3.6:** Natural frequencies of the rectangular hollow beam with different width and height (0.5 mm thickness)

It can be seen from Table 3.6 that the height variation of the rectangular hollow beam affects the 1st mode frequencies more severely than the 2nd mode frequencies. On the other hand, the width variation of the beam affects the 2nd mode frequencies much more than the 1st mode frequencies. In conclusion, utilizing a square beam with equal height and width will give similar frequencies for 1st and 2nd mode. This is further proven in Table 3.7 where the circular hollow beams were analyzed.

Based on the single quadrotor arm simulation results, the smallest simulated rectangular beam of 3 mm  $\times$  3 mm has the lowest natural frequency of higher than 1500 Hz, which is more than twice the maximum rotating speed of the motor of 2291 rad/s, or 729 Hz (see Chapter 5). Thus, it gives relatively high margin for the full quadrotor design, which will be simulated in the next section.

### 3.5.2 Full Quadrotor Configuration

Due to structure stability shown by closed shape beams, the full configuration is then tested using rectangular hollow beam and circular hollow beam to form the arms attached to each corner of the main frame. The main frame is designed to be 28.28  $\times$  28.28 mm with thickness of

Radius (mm)	Frequency (Hz)	
	Mode 1	Mode 2
2.0	1839.3	1839.3
2.5	2347.5	2347.5
3.0	2851.6	2851.6
3.5	3349.6	3349.6
4.0	3840.1	3840.1
4.5	4322.0	4322.0
5.0	4794.3	4794.3
5.5	5256.1	5256.1

**Table 3.7:** Natural frequencies of the circular hollow beam with different width and height (0.5 mm thickness)

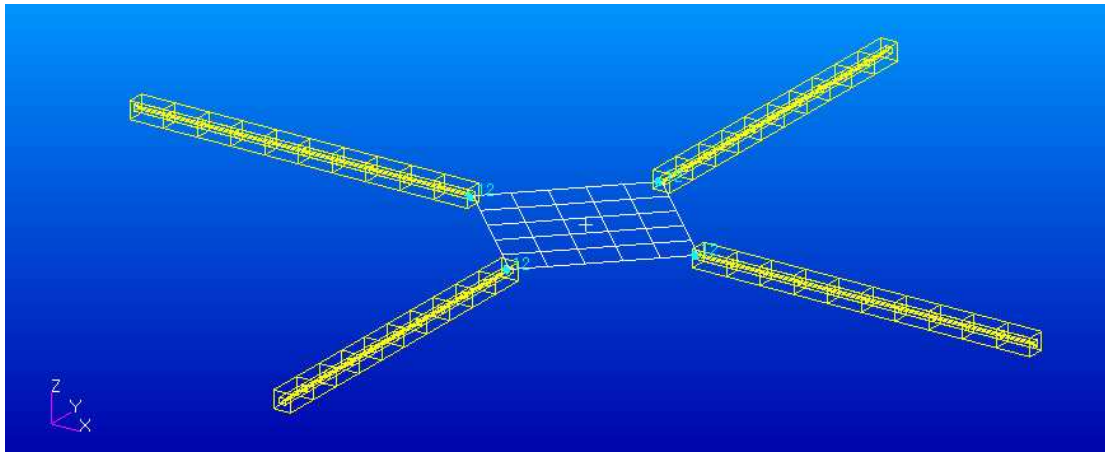


**Figure 3.11:** Quadrotor model with rectangular hollow beams

2 mm. For simulation purpose, the main frame is made of aluminum with modulus of elasticity 70 GPa and Poissons ratio 0.3 with density  $2700 \text{ kg/m}^3$ . Meanwhile, 60 mm long carbon fiber beams are employed as the quadrotor arms. Again, uni-directional carbon/epoxy T300/976 is used. The main frame is modeled as 2D shell element while the quadrotor arm using one dimensional (1D) beam, as shown in Fig. 3.11.

For this analysis, the main frame is assumed to be rigid and thus, fixed in all three translation DOF. For a quadrotor model with arms of  $3 \text{ mm} \times 3 \text{ mm} \times 6 \text{ mm}$  rectangular hollow beam, the resulted natural frequencies for 1st and 2nd mode are 971.92 and 5843.3 Hz respectively. On the other hand, the natural frequencies for quadrotor model using circular hollow beam with

outer diameter of 3 mm with length 6 mm are at 940.35 Hz for first mode and 5070.7 Hz for second mode.

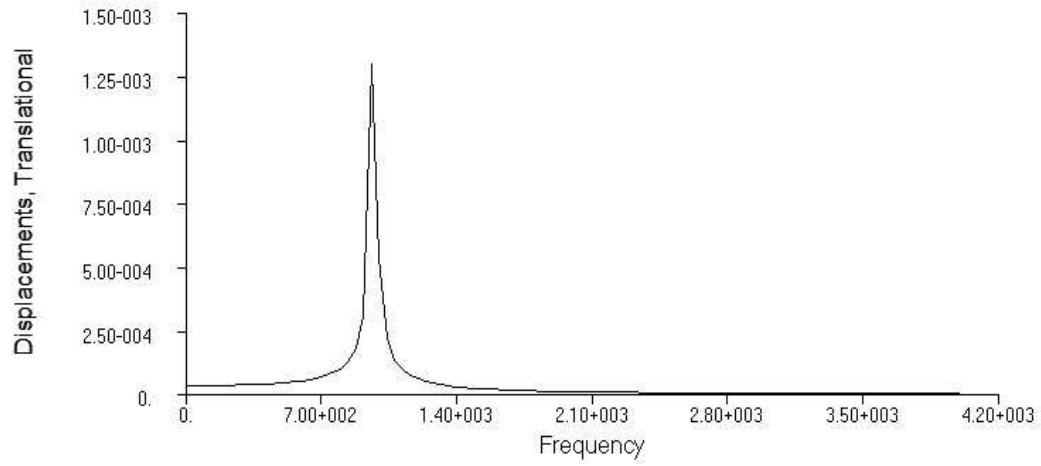
Subsequently, dynamic analysis is performed to investigate the response of the quadrotor to oscillatory excitation produced by the propeller. As the targeted weight for the full MAV system is below 50 g, 0.1225 N force is applied on each arm of the quadrotor. The analysis is performed over frequency range of 0 to 4000 Hz. Results obtained from the Nastran are displayed in Fig. 3.12.

The results show the displacement amplitude at the tip of the quadrotor arm. From the response spectrum, the frequency at peak for both quadrotor models matches the first natural mode simulated earlier. Based on the simulation result, both models are suitable for miniature quadrotor design as the maximum vibration frequency (729 Hz) is far from the natural frequency (971.92 Hz and 940.35 Hz) for the first mode. Therefore, using closed shape beam as the quadrotor arm can guarantee extreme stability for the whole quadrotor model.

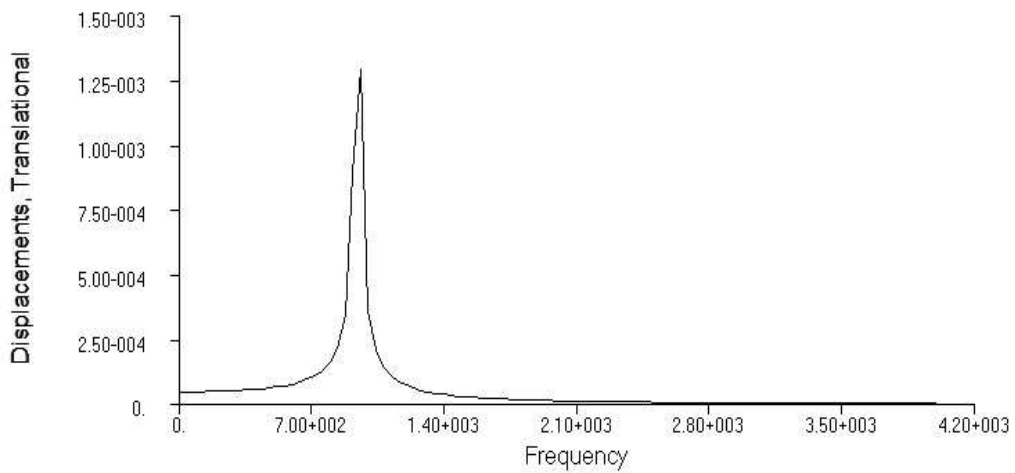
### **3.6 Experimental Validation**

Two test-bench experiments were carried out to verify the natural frequency simulated by Nastran. The first experiment uses an aluminum beam of 200 mm length, 6 mm width and 1.5 mm thickness, with an electrical motor mounted at the tip of the beam. The motor was then powered up to the speed where the aluminum beam starts to vibrate severely. In the second experiment, a carbon fiber beam of 70 mm length, 6 mm width and 1 mm thickness was examined. To obtain the vibration frequency and amplitude of the structure in these experiments, an external laser range sensor was used to detect vibration motion of the beams. Both the experiment results are tabulated in Table 3.8.

From the validation results, one can conclude that the Nastran simulation resembles the real structure up to at least 95% accuracy. The simulation results can therefore be used as a guideline to design the structure of the quadrotor MAV.



(a) Quadrotor model with rectangular hollow beam



(b) Quadrotor model with circular hollow beam

**Figure 3.12:** Displacement response at tip of the arm

Material	Experimental	Nastran Simulation	Accuracy
Aluminum	117.2 Hz	123.34 Hz	95%
Carbon fiber	68.85 Hz	71.57 Hz	96%

**Table 3.8:** Comparison of the first natural mode between experiment and simulation results



### 3.7 Quadrotor Body Design

The previous sections have illustrated the structural analysis for several beam candidates. It is noted that closed shape beams yield higher natural frequencies, thus outperforming the others. Oscillatory steady-state excitation representing the force induced by propeller is experimentally determined along with its working frequency. The external force is then applied on the tip of each quadrotor arm for frequency response analysis. The results show quadrotor models with either rectangular hollow or circular hollow cross-section give significantly low displacement amplitude. Also, the natural frequency for both model are above 940 Hz which is far away from the working frequency of the proposed micro quadrotor. Therefore, rectangular hollow or circular hollow beams are the most suitable structures to form the quadrotor arms. In fact, they are widely available.

According to the results from the beam analysis, four carbon fiber tubes with the dimension of  $60 \times 3 \times 3$  mm are utilized to connect four motors to the base frame. The base frame is designed with the aid of a 3D mechanical design software named SolidWorks. SolidWorks develops efficient and quicker designs of mechanical products and components, facilitating the design tasks for the platform. This 3D software is chosen as the design and analyzing software over other mechanical design tools for the following advantages:

1. In-built intelligence design tools increase design efficiency and minimize design error;
2. Better visualization of the design with intuitive interaction with the 3D model;
3. Easy one click creation of 2D drawing from 3D objects for fabricating and manufacturing;
4. Weights, center of gravity (CG), moment of inertia and other geometric data can be obtained directly from the evaluation functions;
5. Vibration and resonant frequencies simulation can be conducted with aid of SolidWorks simulation softwares.

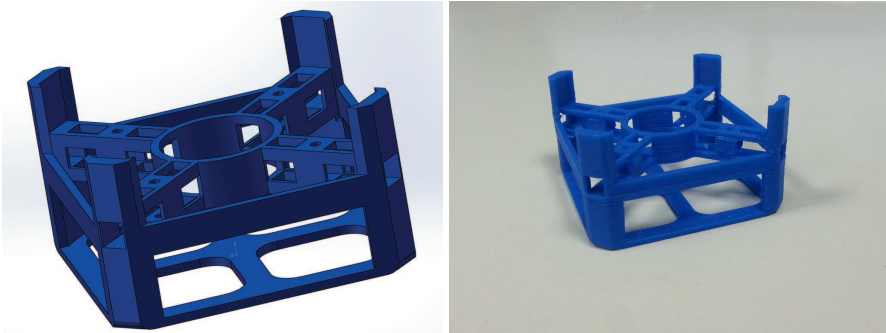


**Figure 3.13:** Fabricated quadrotor body and its counterpart designed in SolidWorks



**Figure 3.14:** Motor holder designed in SolidWorks

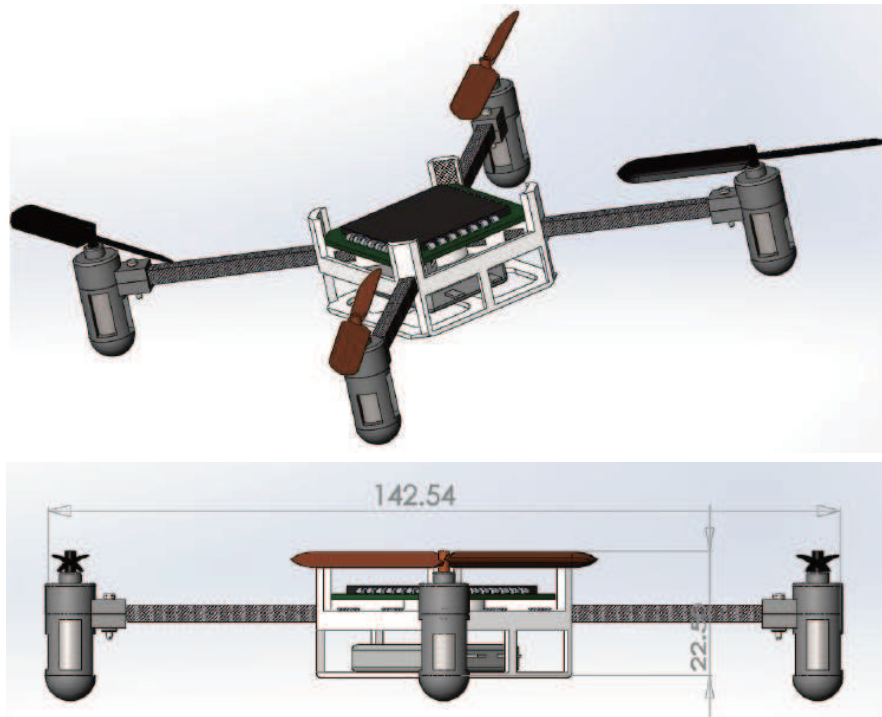


**Figure 3.15:** Full micro quadrotor body designed in SolidWorks with dimension (in mm)



**Figure 3.16:** Fabricated MAV platform

The base frame is designed such that it holds four carbon fiber tubes, forming a symbolical cross shape of the quadrotor. Two partitions were created to mount the avionic circuit and to hold the battery. It can be visualized in Fig. 3.13.

Four light weight holders are designed to mount the electric motor to the end of each beam (see Fig. 3.14). Together with the base frame, they are fabricated with acrylonitrile butadiene styrene (ABS). Although the ABS material is not as stiff as the carbon fiber, as the base frame and the motor holder have no slender parts, the overall natural frequency of the system will not be affected much. The ABS material is not only light weight, but it can also be fabricated easily by shaping from mould or 3D printing. The complete frame design for the quadrotor MAV can be visualized in Fig. 3.15. Once the design is confirmed, the MAV is fabricated as shown in Fig. 3.16. Note that this mechanical design allows the carbon rod to be inserted into the middle layer of the center frame, where only part of the rod appears outside the frame. The total diagonal length of the aircraft is thus 142.54 mm.

Vibration analysis is again carried out in simulation for the quadrotor frame design. Frequency analysis of these assembly parts are shown in Fig. 3.17, where the fundamental resonant frequency of the current structure is estimated in simulation as 1199.6 Hz, which is much higher than the working frequency of the motors. Flight tests of the fabricated MAVs are also carried out to verify that the whole platform design is free from vibration problems. A complete work of this chapter is documented in [57,59].

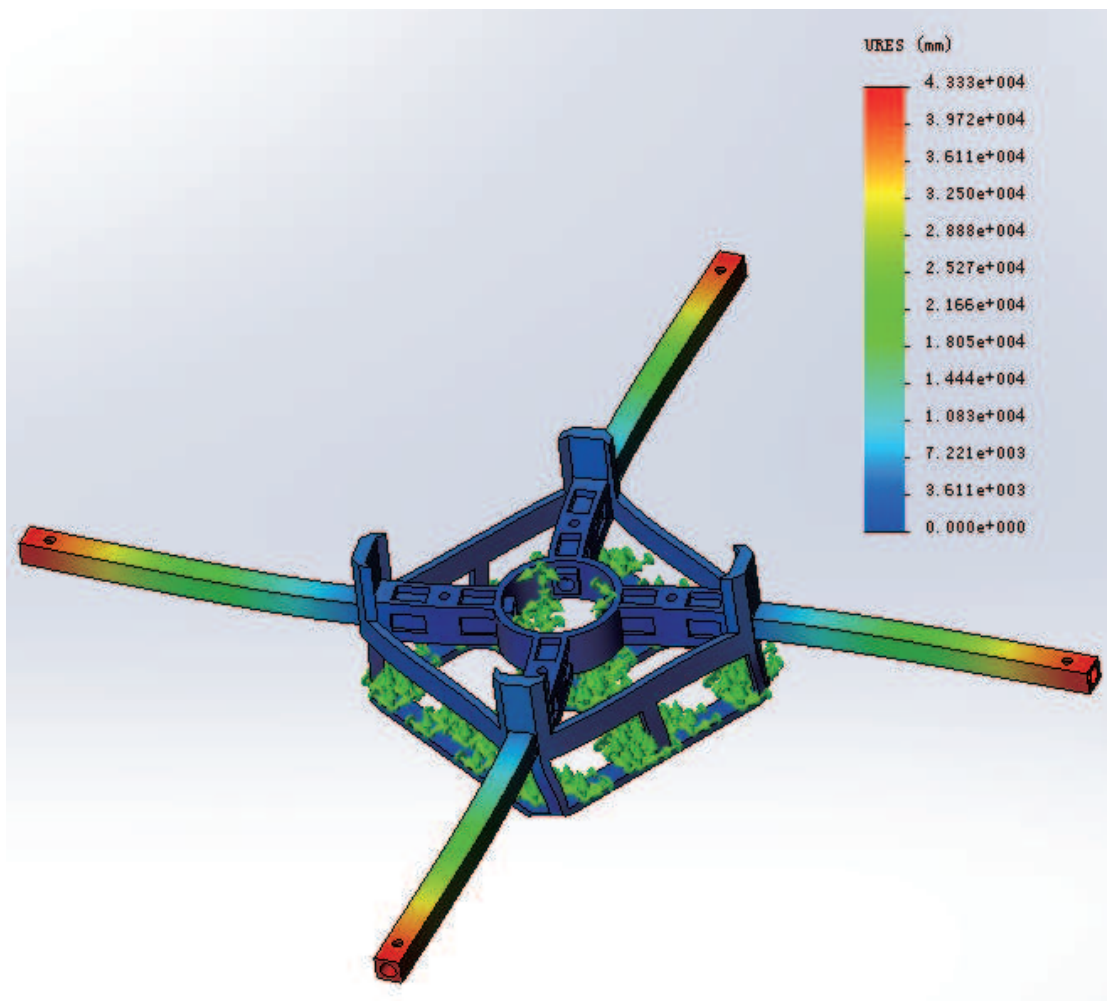


**Figure 3.17:** Vibration analysis of quadrotor frame



# Chapter 4

## Avionics Design

### 4.1 Introduction

To construct a quadrotor MAV capable of autonomous flying, several essential hardware and electronics are required. Besides the aircraft bare body, an MAV also consist the following hardware:

1. **Motors and propellers** to create the main lift for the aircraft;
2. **Electronic speed controllers (ESCs)** to precisely control the rotational speed of the motors;
3. **Microprocessor** to process control algorithm and to output control signal to the speed controller;
4. **IMU** to measure attitude changes of the MAV for control purpose;
5. **Camera** to provide local position information for navigation purpose;
6. **Radio frequency (RF) receiver** to receive control command from the ground station;
7. **Data logger** to log flight data.

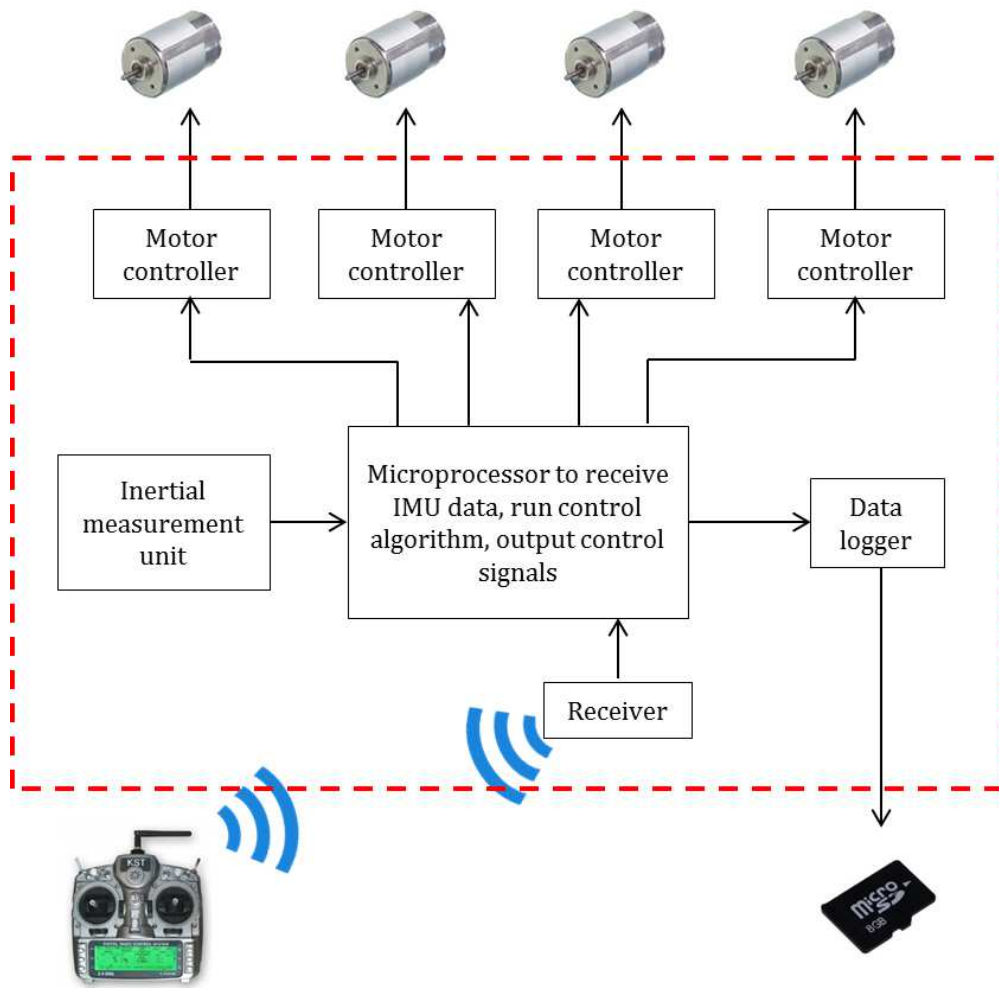


**Figure 4.1:** Essential hardware and electronics needed for a quadrotor MAV

The overview of the quadrotor MAV hardware and electronics connection can be viewed in Fig. 4.1. In this chapter, each hardware and electronics will be discussed in detail, followed by a customized avionic circuit board that integrates most of the electronics. In the last section, software implementation of the MAV system will be briefed.



## 4.2 Motor and Propeller

Motor and propeller are the main actuators of the quadrotor MAV. As each quadrotor consists of four sets of motor and propeller, they need to be carefully chosen as their characteristics must satisfy the design requirements [5, 40]. A few important design requirements of the quadrotor MAV, which are directly related to the characteristics of the motor and propeller, are listed below:

1. *Operating Voltage*: Different motor has different maximum input voltage, depends mainly on the size of the motor, and the torque produced by the motor. In general, smaller motor has lower operating voltage, where the torque produced by such motor is also relatively lower. In RC aircrafts, the motor operating voltage is commonly rated in the multiple of 3.7 V, similar to the output voltage of a single cell Lithium-polymer (LiPo) battery. In the MAV design, since majority of the components can be powered by voltage as low as 3.3 V, a single cell powered motor will be ideal to the design.
2. *Current Consumption*: As motors are the main power drains for the MAV, the current consumption of the motor directly affects the capacity of the battery needed for the MAV to fly in a specific amount of time.
3. *Weight*: Four motors contribute four times its weight to the MAV system, and thus affect the overall weight of the system heavily.
4. *Maximum Thrust*: The maximum thrust of four rotors could produce must be at least greater than the overall weight of the MAV, for MAV to take-off. Ideally it must be at least 1.5 times the weight of the quadrotor to realize more aggressive maneuver.

Based on the requirements stated above, a 8000 kV single cell brushed DC motor is utilized. Combined with four propellers, two with clockwise and another two with anticlockwise spinning blades, the total weight of a single motor and propeller set is approximately 4 g. The propellers used are made of plastic, 56 mm in length. This propeller is readily available in the

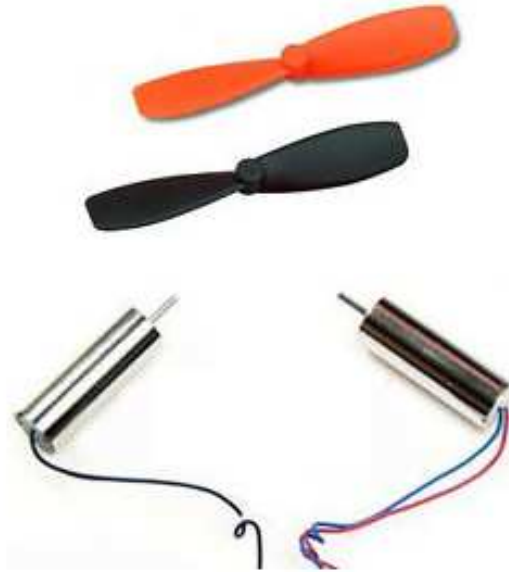


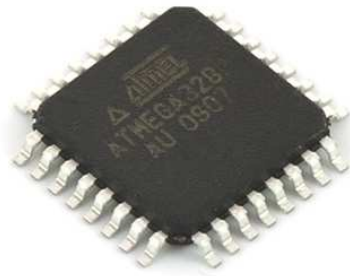
**Figure 4.2:** Motor and propeller of the MAV

market, as it is also used in many hobby-range RC quadrotor such as Walkera QR Ladybird, Hubsan mini Quad, and TRAXXAS QR-1 (see Fig. 4.2). Test bench experiment has proven that the combination could produce a maximum thrust of 20 g each, which combined is approximately 1.5 times larger than the proposed weight of MAV at 50 g.

### **4.3 Micro-Processor**

In avionics, processor is the crux of the entire system. Within this compact MAV design, the functions of the processor are

1. To read IMU data at 100 Hz;
2. To read command from the receiver in the form of pulse-position modulation (PPM);
3. To decode IMU and receiver's data;
4. Run data filtering and control algorithm;



(a) ATmega328P



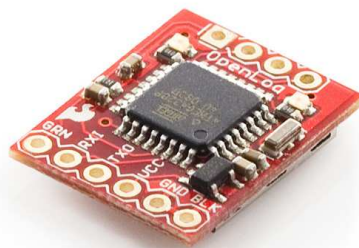
(b) VN-100 SMD



(c) ATtiny13A



(d) DelTang Rx31d



(e) Sparkfun OpenLog

**Figure 4.3:** Components used in avionic system design

<b>Parameter</b>	<b>Value</b>
Flash memory	32 Kbytes
Pin count	32
Max. operating frequency	20 MHz
CPU	8-bit AVR
SPI	2
I2C	1
UART	1
PWM	6
ADC channels	8
Operating voltage	1.8 - 5.5 v
Active current consumption (1 MHz, 1.8 v)	0.2 mA

**Table 4.1:** Key parameters of ATmega328P

5. To output pulse-width modulation (PWM) signals to ESCs;
6. To log data to the external logger.

In order to perform these tasks, ATmega328P (see Fig. 4.3(a)), a high performance Atmel 8-bit AVR microcontroller is selected due to the presence of the following characteristics:

1. Availability of various ports sufficient for MAV use;
2. Low power consumption;
3. Programming convenience with Arduino libraries.

Key parameters of ATmega328P are listed in Table 4.1.

## **4.4 Inertial Measurement Unit**

IMU is an indispensable sensor to all autonomous aerial vehicles. It is attached to the aircraft to provide vital real-time motion data such as accelerations, angular rates, and magnetic values. In addition, 3-axis Euler angles measurements are necessary for aircraft orientation control. However, IMU does not necessarily need to provide angular measurement of the aircraft as it can be estimated using an extended Kalman filter (EKF) [33] or complimentary filtering. The

<b>Parameter</b>	<b>Value</b>
Yaw/Roll range	$\pm 180$ deg
Pitch range	$\pm 90$ deg
Angular rate range	$\pm 500$ deg/s
Acceleration range	$\pm 8$ g
Power supply	3.2-5.5 V
Current drawn	50 mA @ 3.3 v
Communication	UART, SPI
Dimension	$24 \times 22 \times 3$ mm
Weight	3 g
Output data	Raw IMU data, Filtered Euler angles
Highest output data rate	200 Hz

**Table 4.2:** Important specifications of VN-100 SMD

primary disadvantage of these filters is - they are computationally intensive, which add extra burden on the on-board Atmel AVR microprocessor. One of the solutions is to select a small, light yet powerful IMU with in-built EKF algorithm.

The VN-100 SMD (Fig. 4.3(b)) from VectorNAV is selected as the on-board IMU. It is light weight (3 g) and miniature ( $24 \times 22 \times 3$  mm) high performance IMU with Attitude Heading Reference System (AHRS). It is also built-in with 3-axis accelerometers, 3-axis gyros, 3-axis magnetic sensors as well as a 32-bit processor to compute and output a real time plus drift-free 3D orientation solution.

Apart from that, VN-100 SMD also comprises a quaternion based drift compensated Kalman filter operating with full 32-bit floating point precision by utilizing the on board 32-bit processor, which updates at 300 Hz according to the data provided. It also provides both raw and corrected sensor measurements as well as the estimated angles at 200 Hz, which is more than sufficient for the MAV system. Important specifications of VN-100 SMD is shown in Table 4.2.

## 4.5 Brushed Electronic Speed Controller

ESC is the fundamental component for each brushed motor used in the MAV design. The purpose of ESC is to convert PWM signal to analog signal, the only waveform accepted as the

input of the motor. Four 8 pins processors ATtiny13A (Fig. 4.3(c)) are utilized as individual ESC to the motors. A customized program is uploaded to the processors to convert low frequency (50 Hz) PWM signal from the main processor to the high frequency (5000 Hz) PWM signal output. Such high frequency PWM signal is effectively filtered to approximate analog voltage to the motor. As the output current of the processor's pin is low, metal-oxide-semiconductor field-effect transistor (MOSFET) is used to boost the current of the analog signal such that it drives the motor directly from the power supply. In total, four processors and four MOSFETs are included in the circuit board design which will be discussed in Section 4.9.

## 4.6 Radio-Frequency Receiver

Typically in RC flights, an RF receiver is used to receive and decode RF signals sent from a transmitter controlled by a remote pilot. Receiver is not a requisite in a fully autonomous flight control system as no remote pilot is required. However, most of the UAV designs today retain the receiver component for failsafe purposes, where the human pilot has higher authority to remotely control the UAV during emergencies.

In the proposed quadrotor MAV system, the receiver is implemented for a different objective. Apart from being able to receive control signal from a remote pilot, the receiver is used to receive control signals from a ground station in autonomous mode. It is effective especially operating in indoor environment with the aid of Vicon motion technology where the system measures the position and velocity of the MAV. Next, the Vicon system will transmit the control signals or the measurement values to the aircrafts on-board processor via the transmitter-receiver link.

This communication link can be realized using a PCTx cable, a product by Endurance R/C (see Fig. 4.4). The PCTx cable connects the ground station (desktop or laptop) to the transmitter which transmits the RF signal wirelessly to the on-board receiver. PPM signal is sent to the on-board processor for processing upon receiving the signals from the ground station. The Rx31d manufactured by DelTang is selected for system integration due to its ultra tiny package of



**Figure 4.4:** PCTx cables from Endurance R/C

10 × 10 mm with 0.21 g (see Fig. 4.3(d)). It is capable of providing up to 7 channels of PPM signals, which is sufficient for a full control of the MAV.

## 4.7 Data Logger

Important flight data such as state variables of an MAV are recorded for post flight observation and analysis, thus requiring a data logger. In order to fit into the MAV avionics, the data logger needs to be small, light and reliable. An open source data logger from Sparkfun - OpenLog (see Fig. 4.3(e)) is utilized for this purpose. OpenLog weighs only 1.70 g and fits perfectly into the MAV design. It starts logging any serial data up to 115200 baud rate to the micro SD card upon powered up. In addition, Sparkfun provides OpenLog firmware and design files which can be redesigned into the main PCB of the avionic system.



**Figure 4.5:** Battery for the MAV

## 4.8 Power Supply

The main consideration in designing the power supply is to meet the overall system and flight duration requirements. The choice of power supply is important as it usually constitutes approximately 30% of the overall weight of the MAV, and the power needed to lift the MAV will be increased due to its own weight. As all on-board components can be powered up with 3.3 V, a single cell LiPo battery is considered.

To efficiently power the MAV system for 8 minutes flight time, the current consumption of each components need to be considered. Table 4.3 shows the total current consumption of the MAV electronics. It is clear that the main power drains are from the motors. To achieve 8 minutes flight time, we need

$$\begin{aligned}\text{Current capacity} &= 2111.8 \times \frac{8}{60} \\ &= 281.57 \text{ mAh}\end{aligned}$$

Assuming 80% efficiency of the system, we needs a battery with close to the current capacity as



Component	Amount	Total Current Consumption (mA)
Motor	4	2000
ATmega328P	1	6.6
ATtiny13A	4	35.2
VN-100 SMD	1	70
Total		2111.8

**Table 4.3:** Total current consumption of MAV system

shown below:

$$\frac{281.57}{0.80} = 351.97 \text{ mAh}$$

A short survey on the market, a LiPo 3.7 V battery with current capacity of 360 mAh is utilized to power the avionics and to drive the motors (see Fig. 4.5). A 3.3 V regulator is included to provide a clean voltage to the components, as a single cell LiPo battery has output voltage from 4.2 V when fully charged to lower than 3.4 V when it is used up. The battery is as light as 9.80 g and is also tested experimentally to provide enough energy for an 8 minutes flight duration.

## 4.9 Avionic Circuit Board Design

In this section, the design process of the PCB for the avionic system of the MAV will be described in detail. Among the five components to be included to the avionic system, the IMU, flight control processor and four ESCs will be incorporated into the design, while the receiver and the logger will be attached to the designed PCB. A general guideline to design avionics PCB for quadrotor MAV using Altium Designer is shown in Fig. 4.6. They will be discussed in the following:

1. *Logic development* - Before the start of the design, circuit logic must be made right.

The connection between each electronics should be identified. Signal transmission type

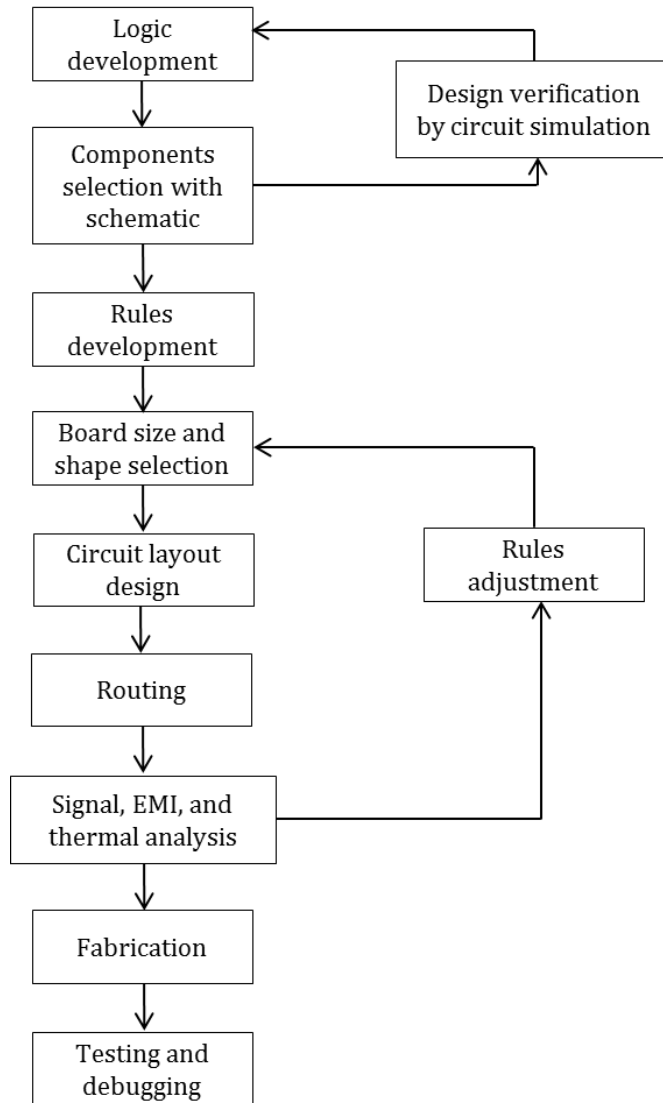
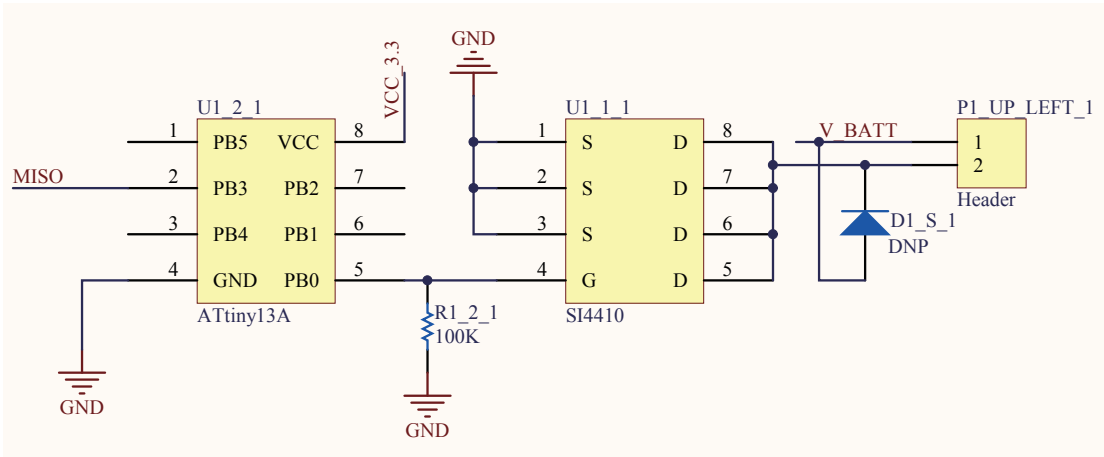
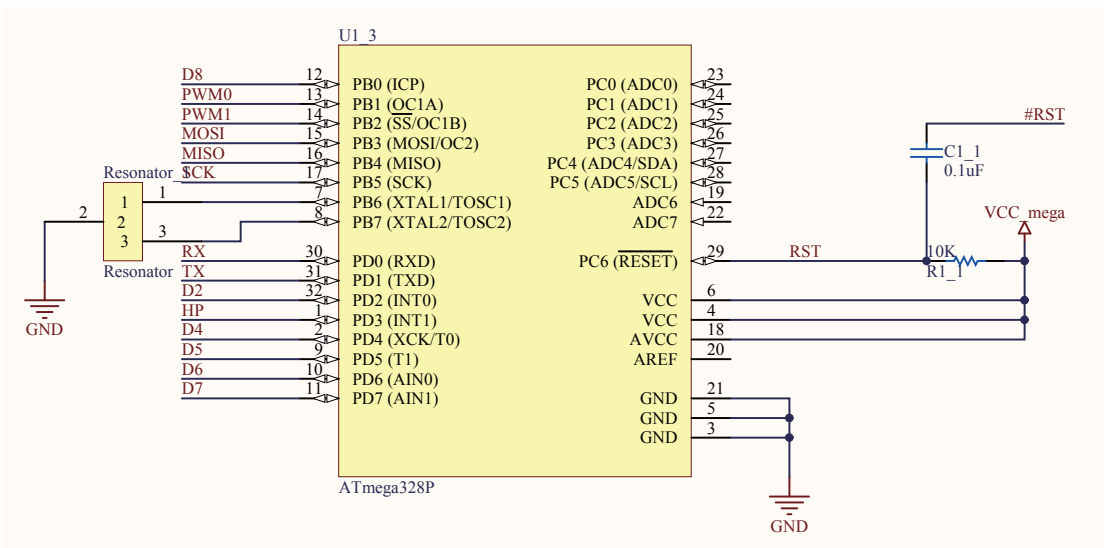


**Figure 4.6:** Flow chart for MAV PCB design



(a) ESC



(b) Processor

**Figure 4.7:** Schematic diagrams

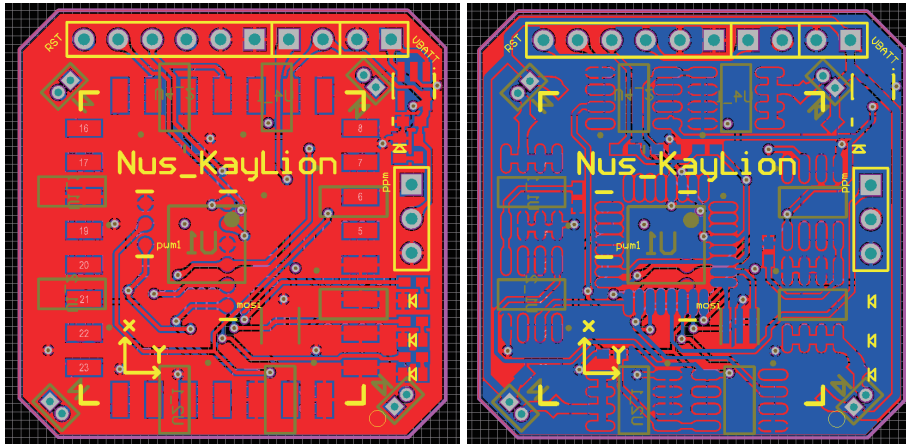


**Figure 4.8:** PCB layout

between each components is analyzed. For example, communication between the receiver and the processor is in the form of PPM signals, while the IMU and the processor are link through a serial port.

2. *Component selection and schematic design* - A schematic diagram of the design must be drawn in Altium Designer with all the components needed, i.e., one ATmega328P, one VN-100 SMD, four ATtiny13As, and four MOSFETs. Also, four status indication LEDs are introduced to the design, with one of them connected directly to the power supply as the power indicator, while the rest of them connected to the general output pins of the flight control processor for user configurable purposes. As all these components can be powered up with 3.3 V, a voltage regulator with 3.3 V output is included. Connections between each of the components can be viewed in the schematics of ESC (see Fig. 4.7(a)) and the micro-processor (see Fig. 4.7(b)).
3. *Design verification by circuit simulation* - A physical circuit prototype is built at this stage with breadboard. The system must work well once it is powered up. For example, the ESC should run the motor once a throttle signal is given from the remote transmitter.
4. *Rules development* - Note that the default distance measurement in Altium Designer is in

unit mil (one-thousandth of an inch). In default, the non-main power routing is set to have a width of 10 mil, while the main power routing (3.7 V directly from power supply) is manually set to be 30 mil width to allow higher flow of current.

5. *Board size and shape selection* - To satisfy the dimension and weight constraints, a square shape of  $4 \times 4$  cm PCB layout is imposed. As only a few components are use in the design, this dimension of the PCB should well be enough to place all components.
6. *Circuit layout design* - The layout of the components on the PCB is important as to reduce the electromagnetic interference between the components. The first component to be placed on the PCB is VN-100 SMD, as it must be placed in the middle of the design to be as closed to the CG as possible. Its orientation is also an important issue to care of, as the  $x$ -axis of the component must be pointed to the front. Next, the flight control processor, ATmega328P is placed in the middle of the opposite side of the PCB, while the four ESCs (one ATtiny13A and one MOSFET each) are placed at the four corner of the same side. Lastly, the four LEDs are placed beside the VN-100 SMD so that they are clearly visible to the user during flight.
7. *Routing* - The final step of designing PCB is the routing to connect each component according to the connection assigned in the schematic phase. The routing could be easily done (see Fig. 4.8) in a 2-layer-PCB setup.

Once the design is done, it can be sent to PCB manufacturer for fabrication. With PCB thickness of 1 mm, the fabricated product is approximately 7 g including all components, within the dimension of  $40 \times 40 \times 1$  mm.

## **4.10 Camera Subsystem**

While the IMU is one essential sensor to provide orientation estimation of the MAV, it can also estimate the position of the aircraft relative to its starting location by integrating the measured

<b>Parameter</b>	<b>Value</b>
Weight (g)	2
Resolution (lines)	420
Pixel	400000
Lens (mm)	2.78
Power supply (V)	3.5-5
View angle (degree)	62

**Table 4.4:** Specifications of the analog camera

<b>Parameter</b>	<b>Transmitter (on-board)</b>	<b>Receiver (ground)</b>
Module code	TX5813	RX5808
Weight (g)	3.4	6.6
Frequency range (MHz)	5705-5945	5705-5945
Power supply (V)	3.5-5	3.5-5
Dimension (mm)	22 × 20 × 3	28 × 23 × 3

**Table 4.5:** Specifications of the video communication modules

accelerations twice. However, the naive approach of integrating the accelerations introduce drifting that would cause serious issue to the MAV position estimation. In the environment where the position of the MAV can be accurately estimated through external sensor, such as under the Vicon motion tracking system, position of the aircraft can be obtained. In practical situation where no external sensors are installed, one of the solution to the localization problem of the MAV can be solved by utilizing vision motion estimation.

In order to realize vision localization, a stand-alone camera subsystem consisting of an analog camera, an analog transmitter and a 40 mAh LiPo battery is designed and fabricated. Table 4.4 lists the specifications of the analog camera while the specifications of the analog video transmitter and receiver are highlighted in Table 4.5. A 40 mAh LiPo battery was selected to provide sufficient power supply to the camera system alone for up to 10 minutes. All the components were integrated on a single customized PCB for easy mounting on the platform. Table 4.6 lists the total parts in the design of the quadrotor MAV together with the actual weight of the manufactured components.

Component	Amount	Weight (g)
Battery	1	9.80
Motor and propeller	4	14.36
Quadrotor arm	4	3.72
Quadrotor frame	1	2.13
Avionic system	1	7.32
Camera system	1	6.25
Miscellaneous		1.70
Total		45.28

**Table 4.6:** Weight breaks down for quadrotor MAV

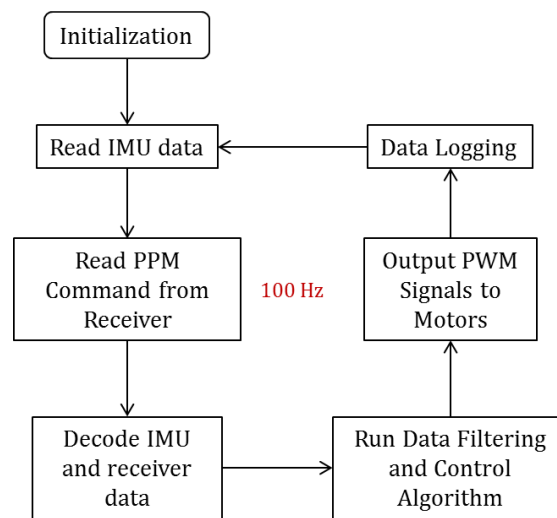


**Figure 4.9:** Tasks to be carried out on MAV's processor

## 4.11 Software Realization

The avionics is not complete without its software. By utilizing Arduino C++ Library, the autopilot software is drafted and implemented from scratch. Arduino environment provides a platform to realize embedded system programming in a straight forward and user friendly manner, especially useful for Atmel processors.

In this section, several key events of the program will be discussed. The flow of the software can be visualized in Fig. 4.9.

### 4.11.1 Read and Decode IMU Data

The measurement data from the IMU can be transferred via a serial port. With the baud rate of 115200, the measurement can be transmitted to the main processor at 100 Hz. The communication data includes

1. Quaternion data of current measurement;
2. Angular rate data of current measurement;
3. Checksum value for error detection.

While angular rate data can be used directly for control, conversions are needed to transform the quaternion to Euler angles. They can be converted easily via

$$\psi = \tan^{-1} \left[ \frac{2(q_0q_1 + q_2q_3)}{q_3^2 - q_2^2 - q_1^2 + q_0^2} \right], \quad (4.1)$$

$$\theta = \sin^{-1} [-2(q_0q_2 - q_3q_1)], \quad (4.2)$$

$$\phi = \tan^{-1} \left[ \frac{2(q_0q_3 + q_2q_1)}{q_3^2 + q_2^2 - q_1^2 - q_0^2} \right], \quad (4.3)$$

where  $q_0, q_1, q_2, q_3$  are the quaternion variables obtained from the IMU data. Through the conversions, the main program is able to retrieve Euler angle and angular rate measurements every 10 ms.

### 4.11.2 Read and Decode Receiver Data

The selected receiver has two output modes: PWM and PPM outputs. PWM output requires each channel (Total of 5: Aileron, Elevator, Throttle, Rudder, Switch) to have its own pin, where as PPM output requires only one pin, where all the channel outputs are queued up and sent out one after another. Although the PPM output has lower time resolution as compared to PWM output, it is ideal for the MAV system as the main processor has limited PWM ports.

As PPM signal uses the width between pulses as signal modulation, the value of the data can be retrieved by recording the time taken between each pulse. An example of PPM signal is



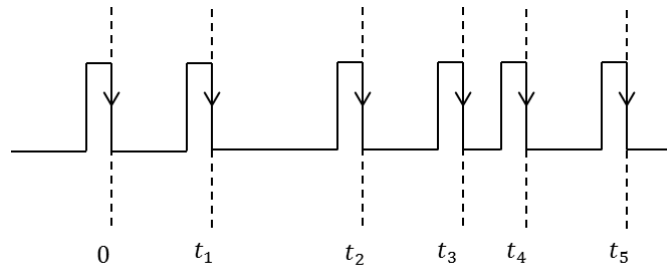


**Figure 4.10:** PPM signal from receiver

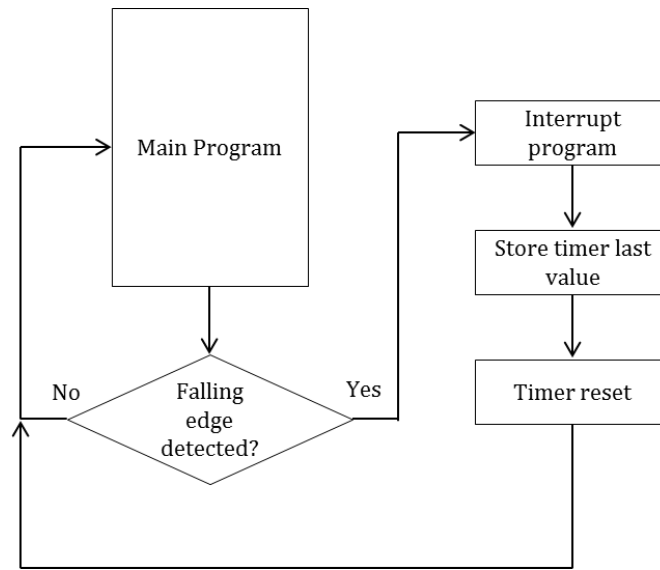


**Figure 4.11:** Flow of program in getting PPM reading

shown in Fig. 4.10, where  $t_1$ ,  $t_2 - t_1$ ,  $t_3 - t_2$ ,  $t_4 - t_3$  and  $t_5 - t_4$  correspond to the time taken between the consecutive pulses, which ultimately represent the values of the data on channel 1 to 5. To obtain  $t_1$  to  $t_5$ , a timer and an interrupt pin from ATmega328P is utilized as shown in Fig. 4.11. According to the flow chart, the PPM data is decoded as the stored timer value.

### 4.11.3 Generate PWM Signals

To receive PPM signals from the receiver, one timer is reserved, left only two more for generating PWM outputs. As there are total of four PWM signals to be sent out from the processor, both the timers need to be utilized well.

In the MAV software design, the PWM signals are set to 50 Hz. In other words, there are 20 ms time-lapse between the pulses. In general, the pulses of PWM signal are in the range of 1 ms to 2 ms, where the width of the pulse indicate the data of the signal sent. Due to this property, it only utilize less than 10% of the duty cycle for each PWM signals, and thus it can be realized using just two timers, as shown in the steps below:

1. According at the time flow shown in Fig. 4.12, at time  $t_1$ , PWM1 signal will be pulled up, Timer1 will be initialized to 5 ms, while Timer2 will be initialized to  $(t'_1 - t_1)$ , where its value is determined by the controller output for motor 1;
2. At time  $t'_1$ , Timer2 will overflow and hence interrupt the program. At this instance, PWM1 signal will be pulled down;
3. At time  $t_2$  which is 5 ms after  $t_1$ , Timer1 will overflow and hence interrupt the program. At this instance, PWM2 signal will be pulled up and Timer2 will be initialized to  $(t'_2 - t_2)$ , where its value is determined by the controller output for motor 2;
4. Similar procedure will be carried out every 5 ms during Timer1 overflow interrupt. This algorithm ensure all four PWM outputs are generated with just two timers.

A flow chart graphical view of the algorithm is shown in Fig. 4.13.

#### **4.11.4 Total Program Run-Time**

Multiple tests were conducted to ensure ATmega328P microcontroller is capable of running the software and perform the tasks mentioned above within a specific time. Fig. 4.14 shows the total program run-time in the conducted experiment. The main loop of the program which run the control algorithm is able to complete each loop within 5 ms. The software main loop is thus set to 100 Hz, so that the processor will never be overloaded, as there will be more than 50% margin for each loop of processes.

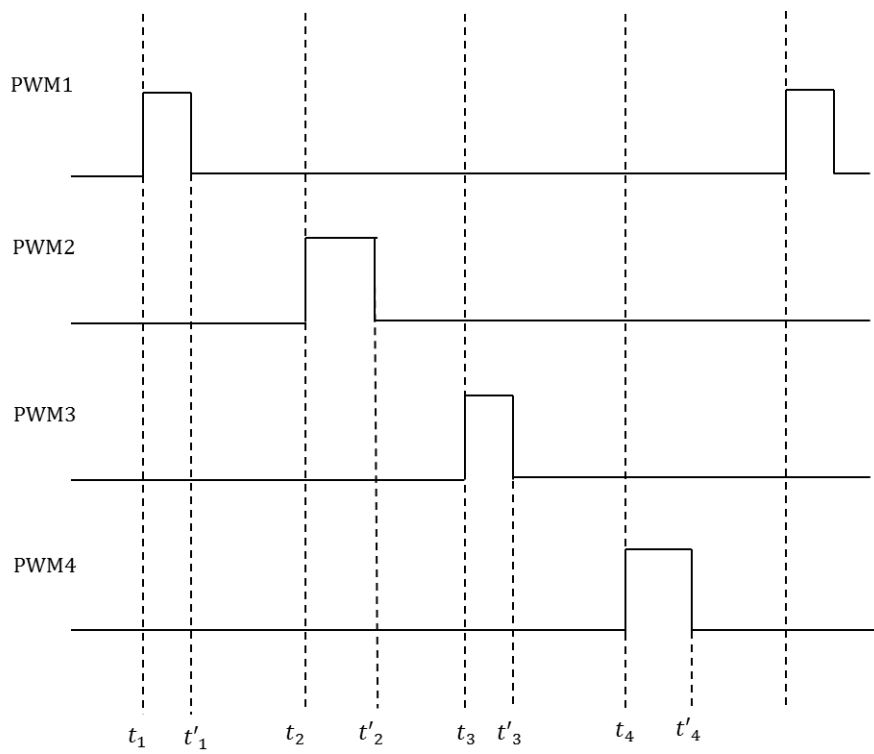


**Figure 4.12:** Synchronization of four PWM outputs

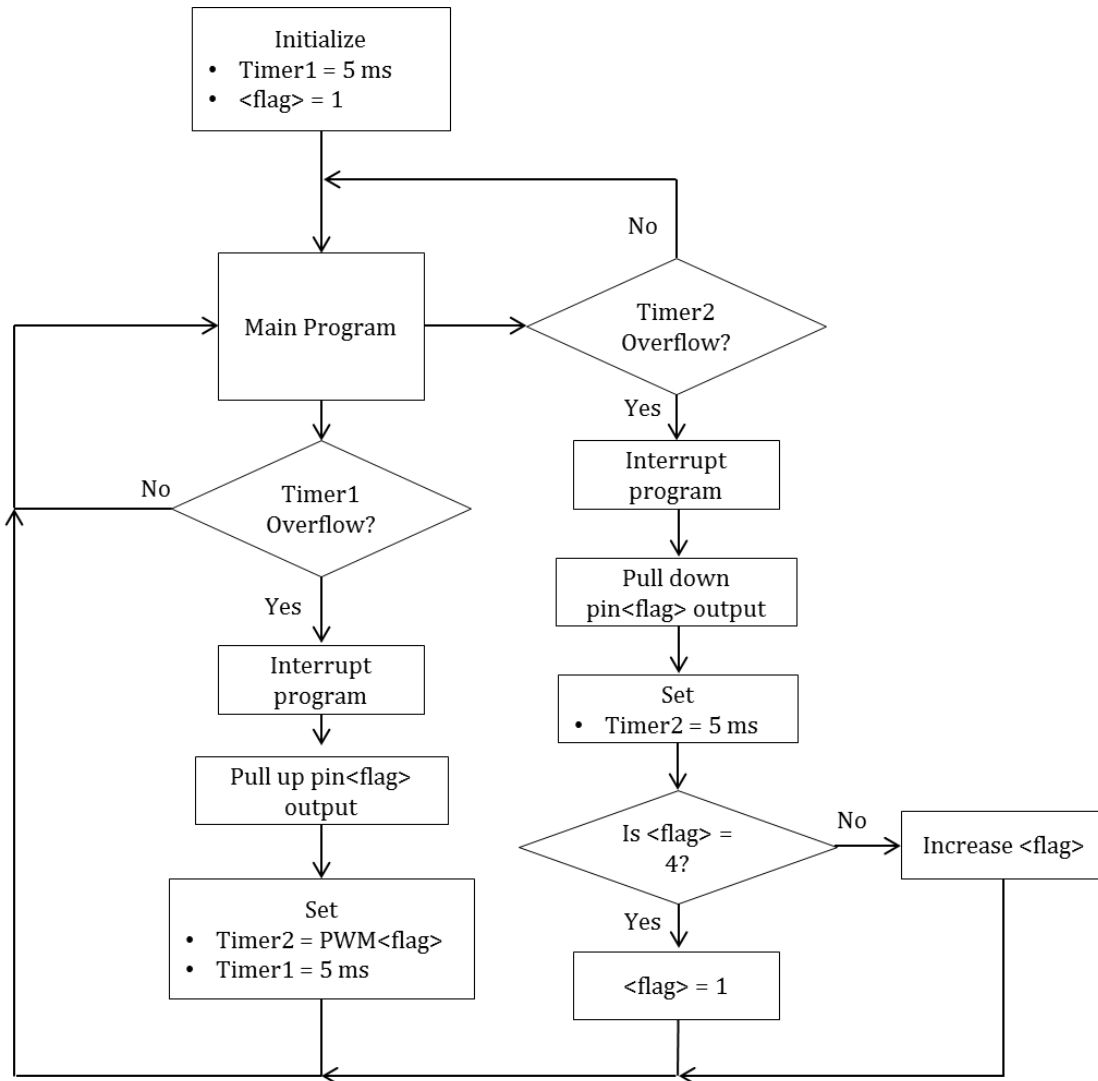


**Figure 4.13:** Flow of program in generating PWM outputs

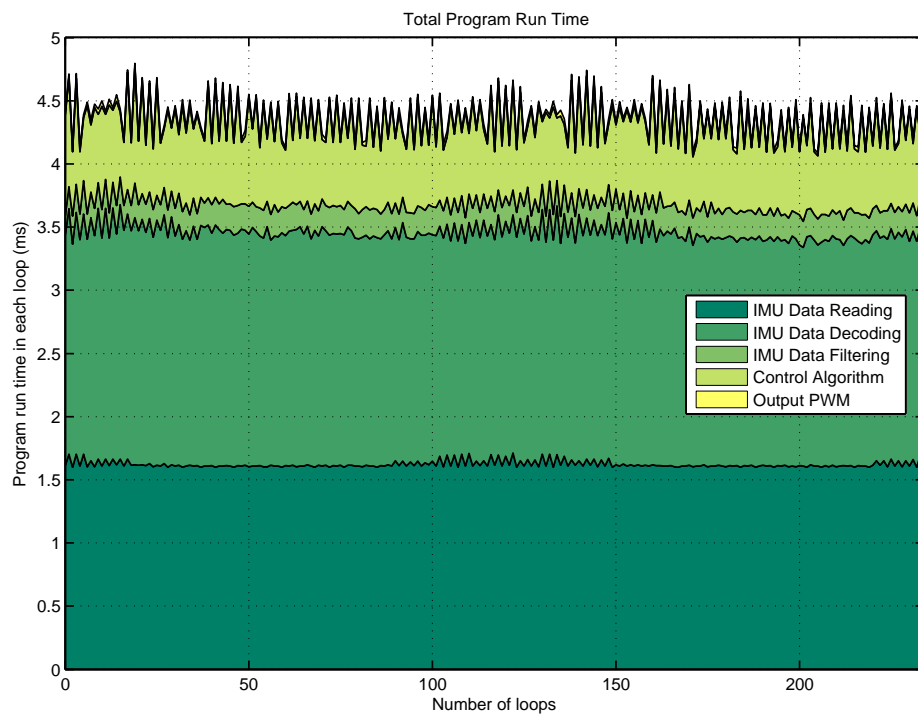


**Figure 4.14:** Total program run-time



## Chapter 5

# Dynamics Modeling

### 5.1 Introduction

As the quadrotor MAV has relatively simpler dynamics compared to helicopter or co-axial rotorcraft, a model based controller design is desired. Model based controller design allows a systematic design process such that specific control performance of the system can be achieved. Mathematical model of the platform is essential to the MAV system design.

In this chapter, a nonlinear model for quadrotor MAV is derived to describe the dynamics of the aircraft. A few assumptions are made in deriving the model:

1. The origin of the body-frame is coincident with the CG of the quadrotor;
2. Axes of body-frame coincide with body principal axes of inertia, i.e. the moment of inertia of aircraft body,  $\mathbf{J}$ , is diagonal;
3. Propellers are assumed rigid due to its small size, i.e., no blade flapping occurs.

These assumptions are valid as the proposed quadrotor MAV is four way symmetry and of small size.

A model system overview of the quadrotor is presented in Fig. 5.1. Noted that the outputs are displayed on the right of each block, while the inputs are shown on the left.. In the next few

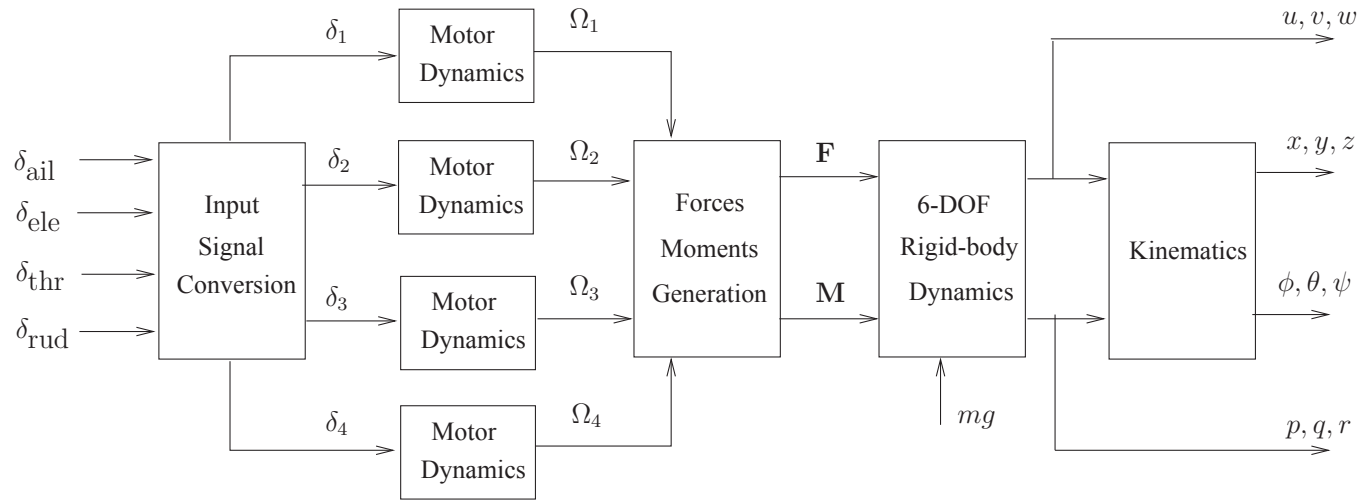
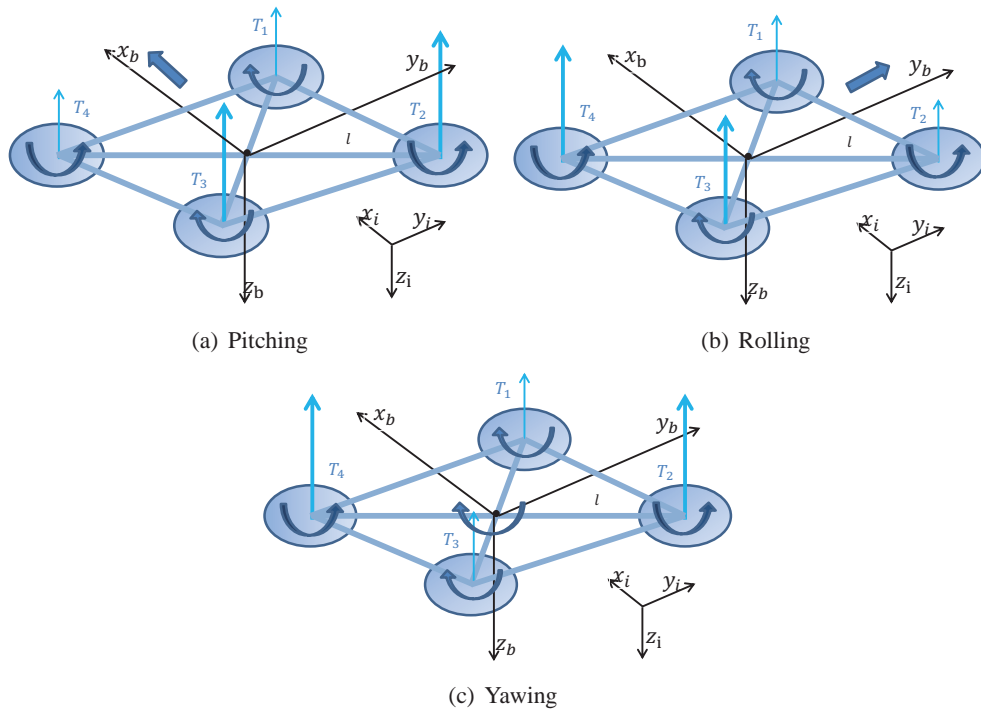


Figure 5.1: Overall model of the quadrotor





**Figure 5.2:** Pitching, rolling and yawing of a quadrotor MAV

sections, mechanism in each major block will be derived, starting from the right-most block. The author's contributions on the dynamics modeling of the quadrotor MAV can also be found in [42, 55, 58]

## 5.2 Working Principle

Before deriving the model, a basic working principle of the quadrotor MAV will be briefly explained. For a quadrotor, the four spinning rotors create a net lift and thus controlling the vertical acceleration of the body. The difference in rotational speeds of the rotors will result in pitching, rolling and yawing of the quadrotor (see Fig. 5.2). Note that in the following derivation, rotor number  $i = 1, 2, 3, 4$  correspond to *front right*, *bottom right*, *bottom left*, *front left* rotor respectively. Rotors 1 and 3 rotate counter-clockwise while rotors 2 and 4 rotate clockwise. Basic main movements of the MAV is tabulated in Table 5.1.

<b>Movement</b>	<b>Rotor 1</b>	<b>Rotor 2</b>	<b>Rotor 3</b>	<b>Rotor 4</b>
Pitching Forward	Slow	Fast	Fast	Slow
Pitching Backward	Fast	Slow	Slow	Fast
Rolling Leftward	Fast	Fast	Slow	Slow
Rolling Rightward	Slow	Slow	Fast	Fast
Yawing Leftward	Slow	Fast	Slow	Fast
Yawing Rightward	Fast	Slow	Fast	Slow
Upward Movement	Fast	Fast	Fast	Fast
Downward Movement	Slow	Slow	Slow	Slow

**Table 5.1:** Main movements of MAV

### 5.3 Coordinate Systems

As a common practice of aeronautic analysis, two main coordinate frames will be used in the derivation. One is the North-East-Down (NED) frame and the other is the body frame. While the NED frame is stationary with respect to a static observer on the ground, the body frame is placed at the CG of the quadrotor helicopter, where its origin and orientation move together with the helicopter fuselage. Note that the body  $x$ -axis pointed to the front of the aircraft, body  $y$ -axis to the right of the aircraft, and body  $z$ -axis pointed downwards in body frame, as shown in Fig. 5.2. From this point onwards in this thesis, coordinates in NED frame will be denoted in subscript  $n$ , while coordinates in body frame will be denoted in subscript  $b$ .

The equations of motion are more conveniently formulated in the body frame for a few reasons [11]:

1. The inertia matrix is time-invariant;
2. Quadrotor body symmetry can greatly simplify the equations;
3. Measurement obtained on-board are mostly given in body frame, or can be easily converted to body frame;
4. Control forces are almost always given in body frame.

## 5.4 Kinematics

To obtain the translational and rotational motions between the NED and the body coordinate systems, one has the following well-known navigation equations [12]:

$$\dot{\mathbf{P}}_{\mathbf{n}} = \mathbf{R}_{\mathbf{n}/\mathbf{b}} \mathbf{V}_{\mathbf{b}}, \quad (5.1)$$

$$\dot{\mathbf{\Theta}} = \mathbf{S}^{-1} \boldsymbol{\omega}_{\mathbf{b}}, \quad (5.2)$$

where the rotational matrix,  $\mathbf{R}_{\mathbf{n}/\mathbf{b}}$ , and the lumped transformation matrix,  $\mathbf{S}^{-1}$  are given by

$$\mathbf{R}_{\mathbf{n}/\mathbf{b}} = \begin{bmatrix} c_{\theta} c_{\psi} & s_{\phi} s_{\theta} c_{\psi} - c_{\phi} s_{\psi} & c_{\phi} s_{\theta} c_{\psi} + s_{\phi} s_{\psi} \\ c_{\theta} s_{\psi} & s_{\phi} s_{\theta} s_{\psi} + c_{\phi} c_{\psi} & c_{\phi} s_{\theta} s_{\psi} - s_{\phi} c_{\psi} \\ -s_{\theta} & s_{\phi} c_{\theta} & c_{\phi} c_{\theta} \end{bmatrix}, \quad (5.3)$$

$$\mathbf{S}^{-1} = \begin{bmatrix} 1 & s_{\phi} t_{\theta} & c_{\phi} t_{\theta} \\ 0 & c_{\phi} & -s_{\phi} \\ 0 & s_{\phi}/c_{\theta} & c_{\phi}/c_{\theta} \end{bmatrix}, \quad (5.4)$$

with  $s_{*} = \sin(*)$ ,  $c_{*} = \cos(*)$ , and  $t_{*} = \tan(*)$ .

Noted that the rotational matrix,  $\mathbf{R}_{\mathbf{n}/\mathbf{b}}$ , is orthogonal, thus its inverse is identical to its transpose, i.e.,  $\mathbf{R}_{\mathbf{n}/\mathbf{b}}^{-1} = \mathbf{R}_{\mathbf{n}/\mathbf{b}}^{\mathbf{T}}$ . This unique property of the rotational matrix greatly simplifies the model of the MAV.

## 5.5 6 DOF Rigid-Body Dynamics

By using the Newton-Euler formalism which describe the translational and rotational dynamics of a rigid-body, the following two dynamic equations take into account of the mass of the air-

craft,  $m$ , and its inertia matrix,  $\mathbf{J}$ .

$$m\dot{\mathbf{V}}_{\mathbf{b}} + \omega_{\mathbf{b}} \times (m\mathbf{V}_{\mathbf{b}}) = \mathbf{F}, \quad (5.5)$$

$$\mathbf{J}\dot{\omega}_{\mathbf{b}} + \omega_{\mathbf{b}} \times (\mathbf{J}\omega_{\mathbf{b}}) = \mathbf{M}, \quad (5.6)$$

where  $\mathbf{F}$  and  $\mathbf{M}$  are the force and moment vectors acting on the body,  $m$  and  $\mathbf{J}$  are the mass and the moment of inertia of the aircraft respectively.

As mentioned in the previous section, the inertia matrix,  $\mathbf{J}$ , is assumed diagonal. It can be represented as

$$\mathbf{J} = \begin{bmatrix} J_x & 0 & 0 \\ 0 & J_y & 0 \\ 0 & 0 & J_z \end{bmatrix}. \quad (5.7)$$

## 5.6 Forces and Moments Generation

According to [10, 24, 28], the force and torque vectors of quadrotors are contributed by two major sources, more specifically, the gravitational force and the main rotor movements. There is another source of moment generation due to the reaction (counter) torque produced by the rotating propellers. However, it is usually neglected as its contribution to this block is usually less than 1% of the total moment generated [11]. For simplicity, it is simply ignored. As a result, the force and moment vector is divided into these two parts

$$\Lambda = \begin{bmatrix} \mathbf{F} \\ \mathbf{M} \end{bmatrix} = \Lambda_{\text{gravity}} + \Lambda_{\text{rotor}}. \quad (5.8)$$

### 5.6.1 Gravitational Force

The first component is the gravitational vector  $\Lambda_{\text{gravity}}$  due to the gravity acceleration,  $g$ . As the gravitational force acting only on the  $z$ -axis of the NED frame, by transforming it to the

body frame, we have

$$\mathbf{F}_{\text{gravity}} = \mathbf{R}_{\mathbf{n}/\mathbf{b}}^{-1} \begin{bmatrix} 0 \\ 0 \\ mg \end{bmatrix} = \begin{bmatrix} -mgs_\theta \\ mgc_\theta s_\phi \\ mgc_\theta c_\phi \end{bmatrix}. \quad (5.9)$$

It is clear that the gravitational acceleration only affects the force vector but not the moment vector, thus overall gravitational vector can be formulated as

$$\mathbf{\Lambda}_{\text{gravity}} = \begin{bmatrix} \mathbf{F}_{\text{gravity}} \\ \mathbf{0} \end{bmatrix} = \begin{bmatrix} -mgs_\theta \\ mgc_\theta s_\phi \\ mgc_\theta c_\phi \\ 0 \\ 0 \\ 0 \end{bmatrix}. \quad (5.10)$$

## 5.6.2 Rotor Movement

The forces and torques directly produced by the main movement inputs contributed to most of the forces and moments generated. For each of the rotating rotor, it creates a thrust,  $T_i$ , and a torque,  $Q_i$ , for  $i = 1, 2, 3, 4$ . From the aerodynamics consideration, the thrust and torques created are formulated as

$$T_i = C_T \rho A R^2 \Omega_i^2, \quad (5.11)$$

$$Q_i = C_Q \rho A R^3 \Omega_i^2, \quad (5.12)$$

where  $C_T$  and  $C_Q$  are the aerodynamic coefficients of the propeller,  $\rho$  is the density of the air,  $A$  and  $R$  are the disc area swept by the rotating rotor and the radius of the rotor blade, while  $\Omega_i$  is the rotating speed of the  $i$ -th rotor. In the MAV design, the propellers have fixed pitch. Thus the

aerodynamic coefficients can be approximated as a constant. As the rest of the terms are also constants except  $\Omega_i$ , the equations can then be simplified to

$$T_i = k_T \Omega_i^2, \quad (5.13)$$

$$Q_i = k_Q \Omega_i^2, \quad (5.14)$$

where  $k_T$  and  $k_Q$  can be obtained through experiments. We may call  $k_T$  and  $k_Q$  as thrust coefficient and torque coefficient respectively for ease of reading.

The summation of thrusts produced by each of the rotor will result in a total lift in body negative  $z$ -axis direction, thus

$$\mathbf{F}_{\text{rotor}} = \begin{bmatrix} 0 \\ 0 \\ -(T_1 + T_2 + T_3 + T_4) \end{bmatrix}. \quad (5.15)$$

Next, pitch and roll moments will be generated by the thrust difference of the opposing rotors, while the yaw moments is generated based on the total moments of each rotors, provided they are installed strictly upright. The moment vector will then be

$$\mathbf{M}_{\text{rotor}} = \begin{bmatrix} \frac{l_m}{\sqrt{2}}(-T_1 + T_2 - T_3 + T_4) \\ \frac{l_m}{\sqrt{2}}(T_1 + T_2 - T_3 - T_4) \\ Q_1 - Q_2 + Q_3 - Q_4 \end{bmatrix}, \quad (5.16)$$

where  $l_m$  is the distance from one motor to the CG of the quadrotor. Note that this derivation is only true for a X-configuration quadrotor MAV.

## 5.7 Motor Dynamics

The motor dynamics is the most important block of all which requires high accuracy in modeling, as the dynamics of the quadrotor is highly affected by the motor performance. In order to accurately capture the motor dynamics, signal changes due to the ESC must also be considered. Here, the identification work is separated into two different blocks as shown below:

1. *Voltage generation block*: Analog voltage output by the ESC based on normalized PWM input generated by controller. The whole block will be treated as a static system as the ESC contains no dynamical states;
2. *Motor dynamics block*: Speed dynamic of the motor powered with input analog voltage. This system will be first derived from electrical and mechanical properties of a DC motor, then the parameters will be identified through bench experiments.

### 5.7.1 Equivalent Analog Voltage

In most motor identification commonly done by many researchers, the output voltage  $v_a$ , is assumed to be directly driven by the normalized PWM signal  $\delta$  to the ESC for simplicity. This, however, ignored the transformation cause by the ESC.

Intuitively, one might assume that the output voltage from the ESC is directly proportional to the product of the normalized PWM signal and the supply voltage  $v_s$ . This relationship depends on the working theory and the circuitry of the ESC. In this work, the relationship between the inputs and the output is unknown, and thus can only be identified experimentally. In general, we can write it as

$$v_a = f(v_s, \delta), \quad (5.17)$$

where the normalized input  $\delta$  is

$$\delta = \frac{u_{\text{PWM}} - 1039}{1000}, \quad (5.18)$$

such that  $\delta$  will always stay within 0 and 1. Here the  $u_{\text{PWM}}$  is the PWM input in unit  $\mu\text{s}$ .

## 5.7.2 Electrical and Mechanical Dynamics

There is a main restriction on the motor model: The assumption that the mechanical friction is only linear in the motor speed; namely, only viscous friction is assumed to be present in the motor (such an assumption is approximate since Coulomb friction is usually experienced in motors). The motor dynamics can be separated into electrical and mechanical parts [54]. The analysis on the motor system is also divided into dynamics analysis and steady-state analysis.

### Electrical Properties

The rotor is assumed to be a single coil characterized by the inductance  $L_a$  and resistance  $R_a$ , but it has to be taken into account the back electromotive force (EMF)  $e$  of the motor. The equation associated with such an electric circuit is given by

$$v_a(t) = L_a \frac{di_a}{dt} + R_a i_a + e. \quad (5.19)$$

The following two equations hold for the back EMF  $e$  and the torque exerted by the motor  $T_M$ :

$$T_M = K_\Phi \Phi i_a, \quad (5.20)$$

$$e = K_\Phi \Phi \Omega, \quad (5.21)$$

where  $K_\Phi$  is the magnetic flux constant.

As regards to the flux flowing in the motor, the flux  $\Phi$  is constant for a DC motor with



constant stator magnet, we have

$$T_M = K_1 i_a, \quad (5.22)$$

$$e = K_1 \Omega, \quad (5.23)$$

where  $K_1 = K_\Phi \Phi$ .

### Mechanical Properties

The motor exerts a torque while supplied by voltage on the rotor. This torque acts on the mechanical structure, which is characterized by the rotor inertia  $J$  and the viscous friction coefficient  $F$ . Since propeller torque is exerted on the motor, then, if  $Q$  is the torque produced, the following equation describes the mechanical system of the motor:

$$T_M - Q = J \frac{d\Omega}{dt} + F\Omega. \quad (5.24)$$

As  $Q$  is produced due to aerodynamic torque of the spinning propeller, it can be represented as

$$Q = k_Q \Omega^2. \quad (5.25)$$

More detail derivation of aerodynamic torque has been discussed in the previous sections.

### Dynamic Analysis

The dynamic of the motor is the combination of its electrical dynamic and mechanical dynamic.

The electrical dynamic is given by

$$\frac{i_a(s)}{v_a(s) - e(s)} = \frac{K_a}{1 + \tau_a s}, \quad (5.26)$$

where  $K_a = 1/R_a$  and  $\tau_a = L_a/R_a$  are the rotor gain and time constant.

The mechanical dynamic has the similar form:

$$\frac{\Omega(s)}{T_M(s) - Q(s)} = \frac{K_m}{1 + \tau_m s}, \quad (5.27)$$

where  $K_m = 1/F$  and  $\tau_m = J/F$  are the mechanical gain and time constant.

In general, as the electrical dynamic of the motor is much faster than the mechanical dynamic, i.e.  $\tau_a \ll \tau_m$ , the whole motor dynamic is assumed to behave as a first order system, with mechanical dynamic dominate the performance of the system. Thus, only  $\tau_m$  needs to be identified, while  $K_m$  and  $K_a$  will be broken down into different segments due to the aerodynamic torque. They will be discussed in the following steady-state analysis.

### Steady-State Analysis

In modeling the whole quadrotor as a system, the dynamic of each motor is found to be much faster than the dynamic of the rigid-body, and thus the motor can be considered a static system. This will ease up the identification work as the relationship between the speed of the motor to the input voltage of the motor can be obtained easily.

In equilibrium, taking all derivative terms to zero, we have

$$v_a = R_a i_a + e, \quad (5.28)$$

$$T_M = F\Omega + k_Q \Omega^2. \quad (5.29)$$

Combining them, we have

$$\begin{aligned} v_a &= \left( \frac{R_a F}{K_1} + K_1 \right) \Omega + \frac{R_a k_Q}{K_1} \Omega^2 \\ &\equiv K_2 \Omega + K_3 \Omega^2. \end{aligned} \quad (5.30)$$

## 5.8 Parameter Identification

There are a few parameters needed to be identified in order to obtain the model of the quadrotor. The proposed parameters identification method and their identified values will be discussed in this section.

### 5.8.1 Measurable Parameters

The mass of the aircraft and the length of the arms can be directly measured by a weighing scale and a ruler. Their respective values are:

$$m = 0.0448 \text{ kg},$$

$$l_m = 0.0695 \text{ m}.$$

### 5.8.2 Gravity

For the gravity acceleration, we have the following formulation to estimate  $g$ :

$$g = 9.780327(1 + 0.0053024 \sin^2 \varphi - 0.0000058 \sin^2 2\varphi),$$

where  $\varphi$  is the latitude of the location. In Singapore,  $\varphi \approx 2$  deg, we have

$$g \approx 9.781 \text{ ms}^{-2}.$$

### 5.8.3 Moment of Inertia

According to [29], the moment of inertia for aircraft body can be measured by the trifilar pendulum method. The experimental setup is shown in Fig. 5.3. In this experiment, the aircraft is suspended by three flexible strings with equal length  $l$ . The horizontal distances between the attached points and the CG are  $l_1$ ,  $l_2$  and  $l_3$  respectively. One can slightly twist and release the platform around the  $z$ -axis and record the oscillation period  $t_l$ . The moment of inertia can then

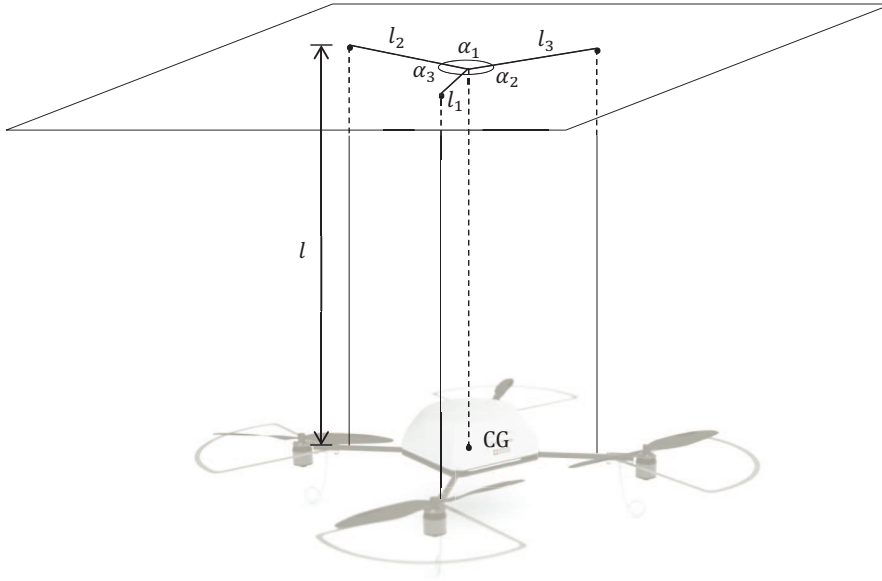


**Figure 5.3:** Trifilar pendulum method

be calculated by:

$$J_z = \frac{mgl_1l_2l_3t_l^2}{4\pi^2l} \cdot \frac{l_1 \sin \alpha_1 + l_2 \sin \alpha_2 + l_3 \sin \alpha_3}{l_2l_3 \sin \alpha_1 + l_1l_3 \sin \alpha_2 + l_1l_2 \sin \alpha_3}.$$

Besides experimental method, the tensor and rotating moment of inertia of the mechanical parts can also be estimated numerically with the aid of SolidWorks. With the exact density and scale to the real physical parts, the tensor moment of inertia of the quadrotor MAV is calculated with the mass properties function of Solidworks. They are given by

$$J_x = 3.0738 \times 10^{-5} \text{ kgm}^2,$$

$$J_y = 3.0849 \times 10^{-5} \text{ kgm}^2,$$

$$J_z = 5.9680 \times 10^{-5} \text{ kgm}^2.$$

#### 5.8.4 Motor Dynamics

An experiment is set up to estimate the value of  $\tau_m$ . As explained in the previous section, the motor dynamics is dominated by its mechanical property, and thus a first order system is assumed. The time constant of such system can be approximated by measuring the transient response of the rotating speed of the motor given a step input.  $\tau_m$  can then be obtained by finding the time taken from the beginning to 63.2% of the steady-state value. It is obtained as

$$\tau_m = 0.0821 \text{ s.}$$

To determine the relationship between the supply voltage  $v_s$  and normalized PWM signal  $\delta$  to the motor rotor voltage  $v_a$ , an experiment is performed by varying  $\delta$  while measuring the output voltage from the ESC,  $v_a$ . The experiment is repeated for a few times with different  $v_s$  to the ESC. The results can be visualized in Fig. 5.4. Some manipulation was done to the input data and output data, we have obtained a fairly linear relationship between the inputs and output as shown in Fig. 5.5. The identified equation is

$$v_s^2 \delta = 1.0864 v_a^2 - 0.7031, \quad \text{or} \quad v_a^2 = 0.9205 v_s^2 \delta + 0.6472.$$

Next, the steady-state property of the motor is identified. The motor was directly supplied with analog voltage  $v_a$ , and the corresponding rotational speed of the propeller is measured with a photo-interrupter. The result is plotted in Fig. 5.6. The response of the motor matches fairly well with the theoretical model of

$$v_a = K_2 \Omega + K_3 \Omega^2, \tag{5.31}$$

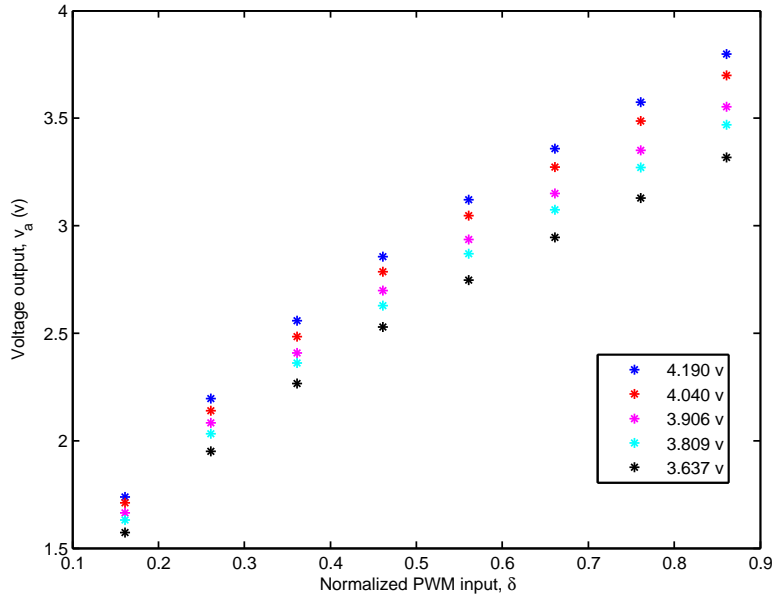


**Figure 5.4:** Steady-state response of the ESC on two different inputs

where

$$K_2 = 1.020 \times 10^{-3},$$

$$K_3 = 2.817 \times 10^{-7}.$$

### 5.8.5 Aerodynamics Coefficients

The relationship between the rotor rotational speed with the thrust produced can be obtained through an experiment as shown in Fig. 5.7. In this experiment, a high grade force and torque sensor is used. The Nano17 F/T Sensor from ATI Industrial Automation is the smallest commercially available 6-axis transducer in the market (see Fig. 5.8). It is designed to measure the 3 DOF force and 3 DOF torque in the small package of 17 mm diameter. With this product, accurate  $z$ -axis thrust and torque of the motor mounted on it can be obtained with ease. In the same setup, a photo interrupter is installed at where the propeller cut through when spinning. The

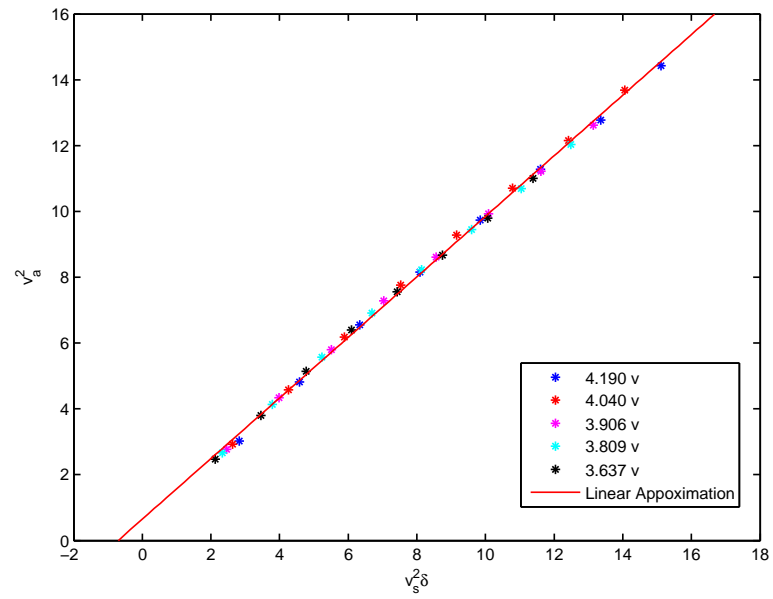


**Figure 5.5:** Linear relationship obtained experimentally

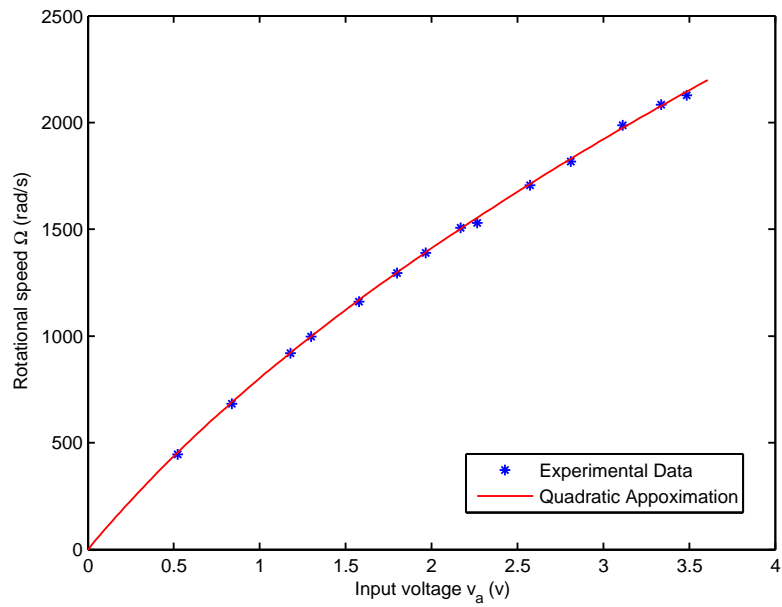


**Figure 5.6:** Rotational speed response of the motor supplied with analog voltage

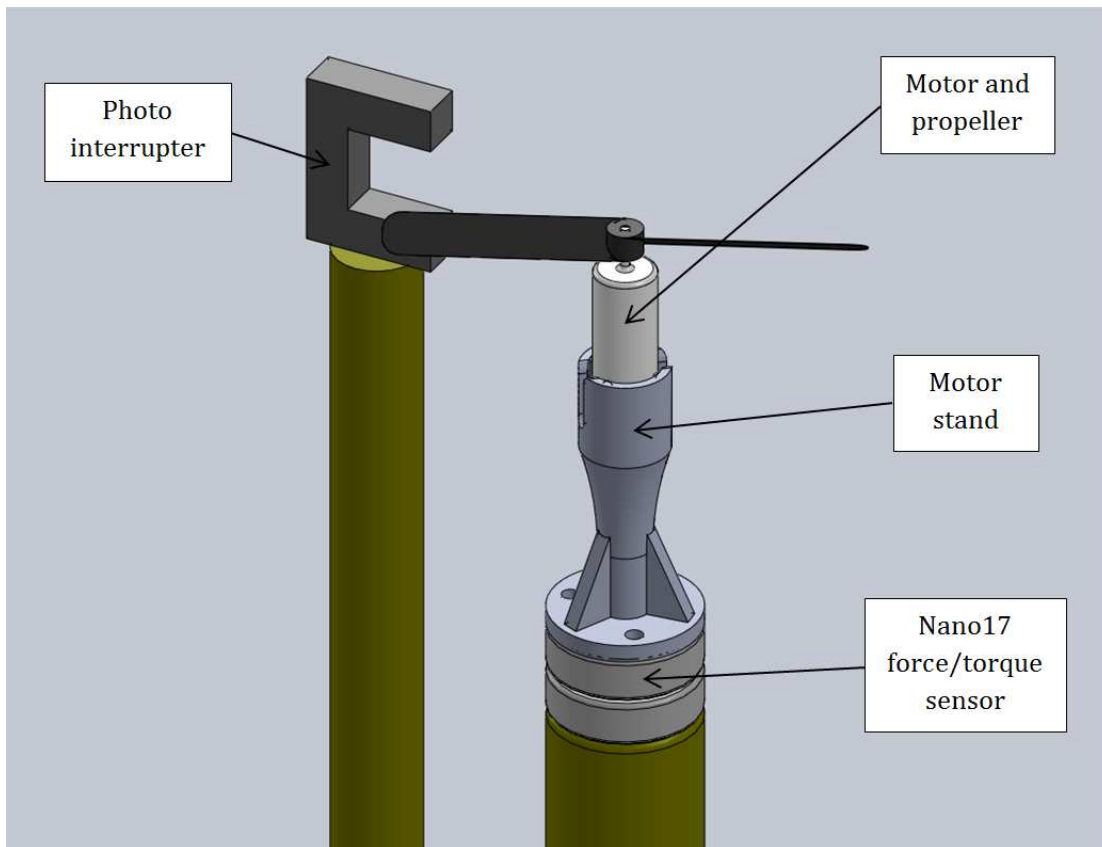


**Figure 5.7:** Setup to obtain motor speed and thrust/torque produced





**Figure 5.8:** Nano17 F/T Sensor

time taken between each cut is recorded and the corresponding rotating speed can be calculated.

The above results are plotted in Fig. 5.9 and Fig. 5.10. The corresponding aerodynamic constants are the gradient of the plots, which are respectively

$$k_T = 3.7901 \times 10^{-8} \text{ N s}^2,$$

$$k_Q = 1.8623 \times 10^{-10} \text{ N m s}^2.$$

## 5.9 Model Verification

The identified parameters with its value and physical meaning are summarized in Table 5.2. With these identified parameters, the mathematical model of the MAV is derived. The dynamics model of the MAV is further verified to be close to the actual dynamics of the systems.

In the verification flight test, the physical MAV is commanded to pitch forward and backward in an oscillating manner, while the oscillating period increases as time goes. This is equiv-

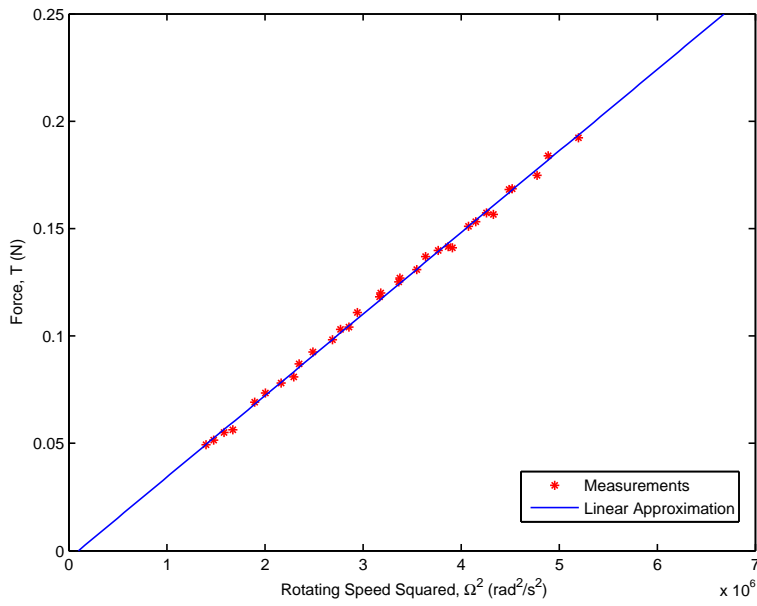


**Figure 5.9:** Thrust vs rotation speed square

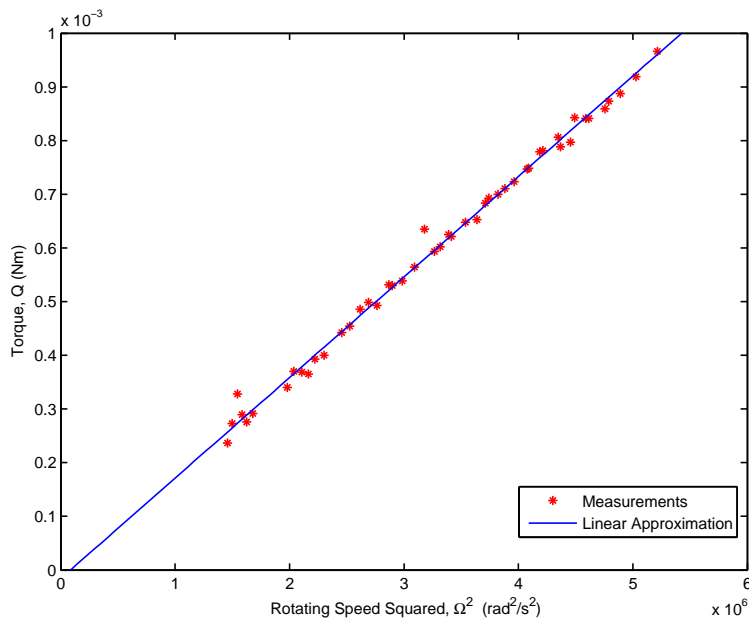


**Figure 5.10:** Torque vs rotation speed square

Parameter	Value	Physical Meaning
$m$	$4.48 \times 10^{-2}$ kg	Mass of the MAV
$l_m$	$6.95 \times 10^{-2}$ m	Distance between a motor to the CG of the MAV
$g$	$9.781$ ms <sup>-2</sup>	Gravitational acceleration at Singapore
$J_x$	$3.0738 \times 10^{-5}$ kgm <sup>2</sup>	Rolling Moment of inertia of MAV
$J_y$	$3.0849 \times 10^{-5}$ kgm <sup>2</sup>	Pitching Moment of inertia of MAV
$J_z$	$5.9680 \times 10^{-5}$ kgm <sup>2</sup>	Yawing Moment of inertia of MAV
$\tau_m$	$8.21 \times 10^{-2}$ s	Time constant of motor
$K_2$	$1.020 \times 10^{-3}$	Lumped constant of $(R_a F / K_\Phi \Phi + K_\Phi \Phi)$
$K_3$	$2.817 \times 10^{-7}$	Lumped constant of $(R_a k_Q / K_\Phi \Phi)$
$k_T$	$3.7901 \times 10^{-8}$ Ns <sup>2</sup>	Thrust coefficient
$k_Q$	$1.8623 \times 10^{-10}$ Nms <sup>2</sup>	Torque coefficient

**Table 5.2:** Identified parameters

alent to the chirp signal that is commonly used in model identification. A chirp input consist of a band of different frequency inputs to the aircraft, where the response of the aircraft should match its frequency response within the band. The Euler angles and angular rates responses of the system are recorded in the on-board logger. The exact same chirp inputs are also fed to the simulator that simulates the dynamics of the MAV from the developed mathematical model. The angles and angular rates responses from the simulator is recorded as well.

Both the flight data and simulated data are compared. Fig. 5.11 shows the perturbation signal on elevator channel to the MAV, while Fig. 5.12 shows the responses of the system in pitch direction plotted together with the simulated results. Besides some random low amplitude oscillations caused by the disturbances from the air movement, the responses match fairly well. The roll response is assumed to be similar to the pitch response, as the quadrotor MAV is four way symmetry.

In the other flight test, a chirp-like signal was injected to the throttle channel of the quadrotor MAV, resulting in agitated heave movement. In this experiment, a Vicon motion tracking system is used to measure the position of the quadrotor with reference to the start up origin. With the measured  $z$ -position, the corresponding velocity respond will be computed. Both the input signals and computed  $z$ -axis velocity are logged and plotted in Fig. 5.13 and Fig. 5.14. In the latter figure, it can be seen that the derived mathematical model on heave movement matches

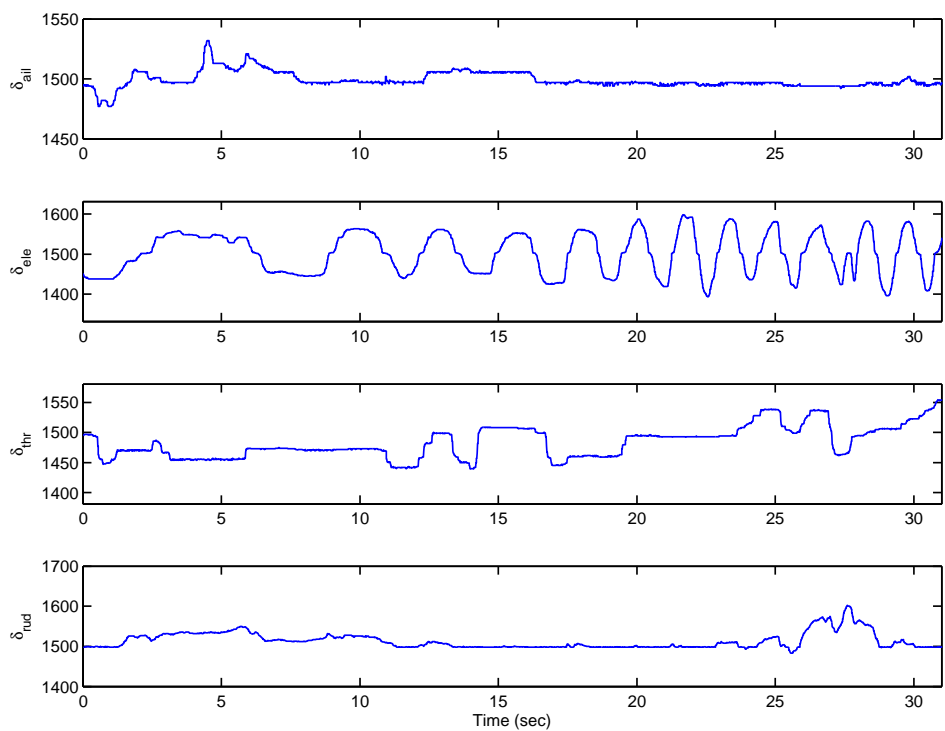


**Figure 5.11:** Input to the MAV system in pitch perturbation test

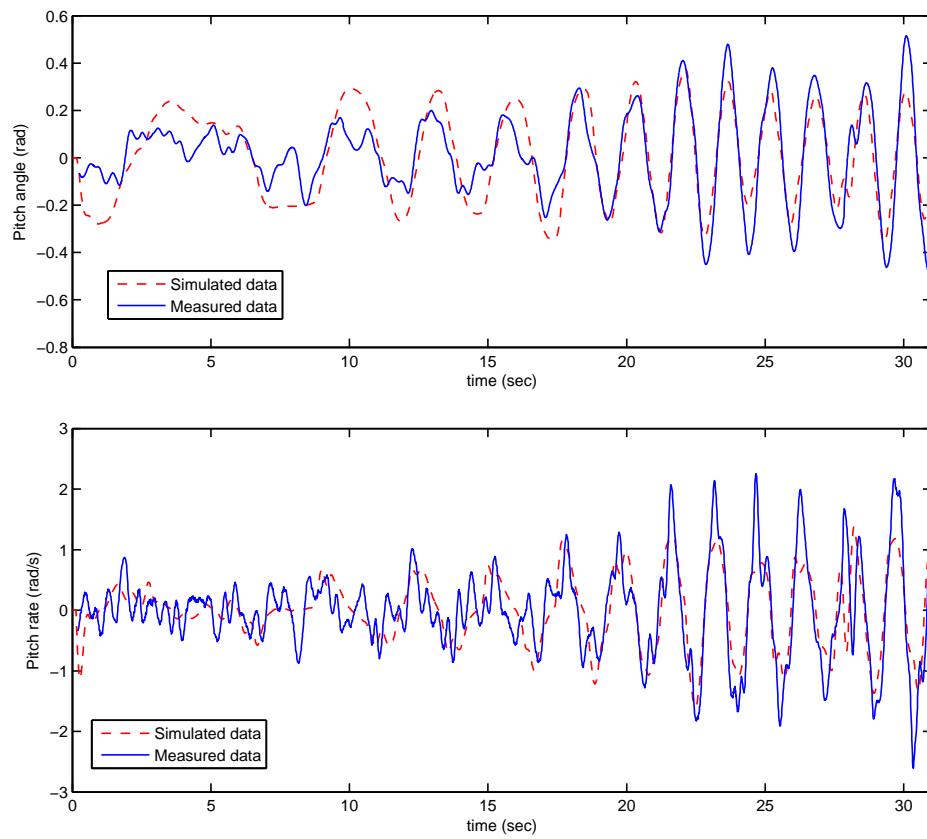


**Figure 5.12:** Pitch angle and angular rate of the system response together with simulated response

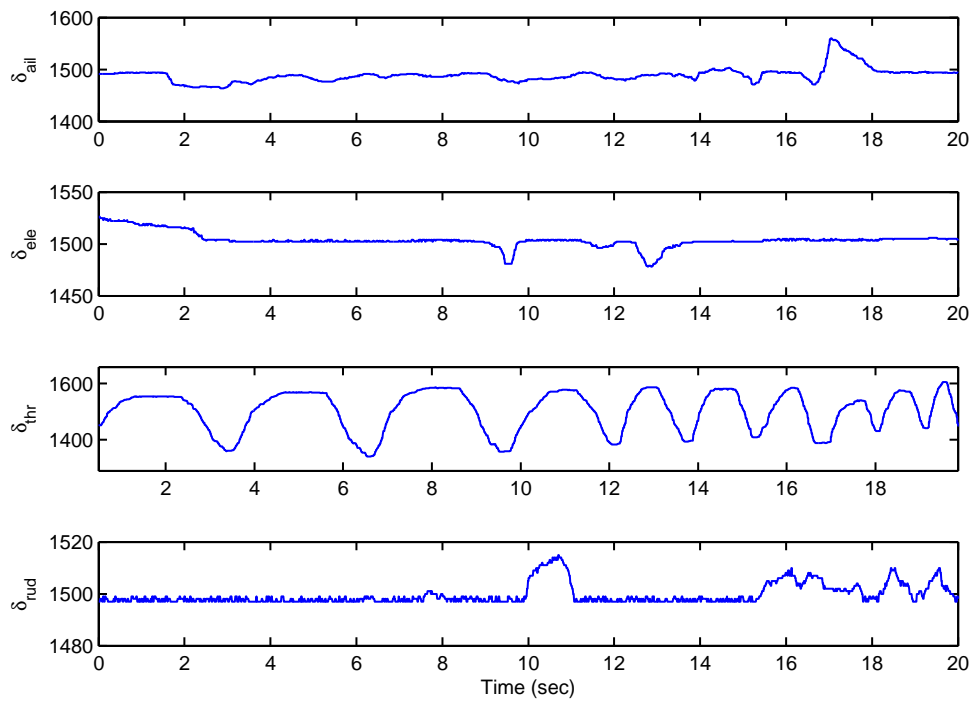


**Figure 5.13:** Input to the MAV system in heave perturbation test

well with the experimental data to a certain perturbation frequency, which is approximately 1 Hz. The quadrotor MAV was unable to respond to the perturbation signal above this frequency, as it can be observed with naked eyes during the flight tests.

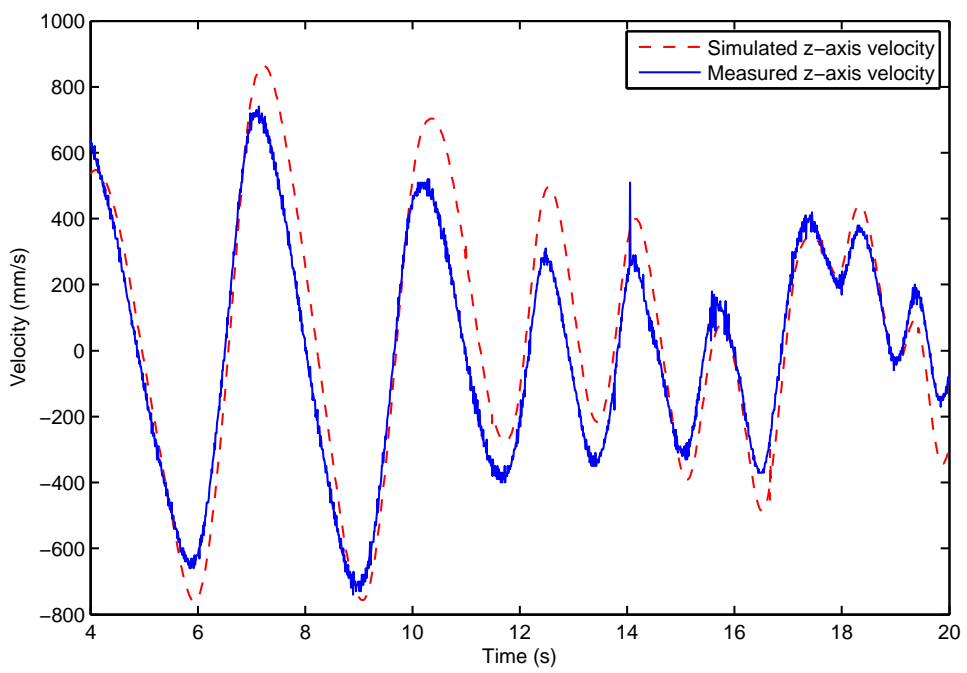


**Figure 5.14:** Heave velocity response of the MAV together with simulated response





## Chapter 6

# Flight Control Systems Design

### 6.1 Introduction

In this chapter, an explicit control structure of the MAV will be proposed and derived. The control inputs are first defined, followed by feedback linearization approach to linearize the dynamic model of the MAV. Then, an LQR based controller is designed to stabilize the orientation of the MAV, and an RPT based controller is formulated for MAV position control. Detailed structure of the inner- and outer-loop layers of the flight control system can be visualized in Fig. 6.1.

Intuitively, the control inputs to the system can be written as  $u_0$  to  $u_3$ , where  $u_0$  is the net body z-axis force of the quadrotor, while  $u_1$  to  $u_3$  are the body moments. With this control inputs allocation, the control of the MAV now has clear physical meaning. The quadrotor dynamics derived from Euler formalism can then be rewrite as

$$\dot{\phi} = p + q \sin \phi \tan \theta + r \cos \phi \tan \theta, \quad (6.1)$$

$$\dot{\theta} = q \cos \phi - r \sin \phi, \quad (6.2)$$

$$\dot{\psi} = q \frac{\sin \phi}{\cos \theta} + r \frac{\cos \phi}{\cos \theta}, \quad (6.3)$$

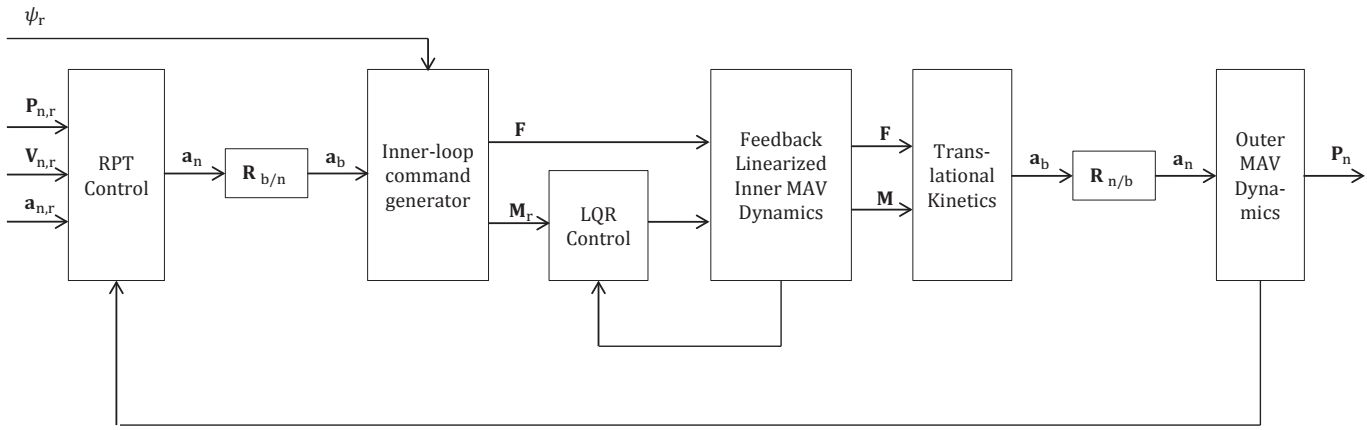


Figure 6.1: Detailed structure of the inner- and outer-loop layers of the flight control system

$$J_x \dot{p} = u_1 + (J_y - J_z)rq, \quad (6.4)$$

$$J_y \dot{q} = u_2 + (J_z - J_x)pr, \quad (6.5)$$

$$J_z \dot{r} = u_3 + (J_x - J_y)pq, \quad (6.6)$$

$$m\dot{w} = mg \cos \theta \cos \phi - u_0 - m(vp + uq). \quad (6.7)$$

Control laws can then be implemented to control the input signals  $u_0$  to  $u_3$  to their desired values respectively. The design of the controllers will be discussed in the next section. Assuming that the desired reference is reached, the control inputs can then be mapped to the pulse width inputs to the motors. In this mapping, the motors dynamics are ignored as they are relatively fast compared to the rigid body dynamics and the aerodynamics of the MAV.

First, rotational speed of each motor can be calculated with any desired force and moments, as follows.

$$\begin{aligned} \begin{bmatrix} u_0 \\ u_1 \\ u_2 \\ u_3 \end{bmatrix} &= \begin{bmatrix} k_T & k_T & k_T & k_T \\ -\frac{lmk_T}{\sqrt{2}} & \frac{lmk_T}{\sqrt{2}} & \frac{lmk_T}{\sqrt{2}} & -\frac{lmk_T}{\sqrt{2}} \\ \frac{lmk_T}{\sqrt{2}} & \frac{lmk_T}{\sqrt{2}} & -\frac{lmk_T}{\sqrt{2}} & -\frac{lmk_T}{\sqrt{2}} \\ k_Q & -k_Q & k_Q & -k_Q \end{bmatrix} \begin{bmatrix} \Omega_1^2 \\ \Omega_2^2 \\ \Omega_3^2 \\ \Omega_4^2 \end{bmatrix} \\ &= 10^{-8} \times \begin{bmatrix} 3.7901 & 3.7901 & 3.7901 & 3.7901 \\ -0.18626 & 0.18626 & 0.18626 & -0.18626 \\ 0.18626 & 0.18626 & -0.18626 & -0.18626 \\ 0.018623 & -0.018623 & 0.018623 & -0.018623 \end{bmatrix} \begin{bmatrix} \Omega_1^2 \\ \Omega_2^2 \\ \Omega_3^2 \\ \Omega_4^2 \end{bmatrix}. \quad (6.8) \end{aligned}$$

For the ease of software implementation, a new variable of rotating speed  $\bar{\Omega}$  in the unit of 10000 rad/s is defined to replace the  $\Omega$ :

$$\Omega = \bar{\Omega} \times 10000. \quad (6.9)$$

We then have

$$\begin{bmatrix} u_0 \\ u_1 \\ u_2 \\ u_3 \end{bmatrix} = \begin{bmatrix} 3.7901 & 3.7901 & 3.7901 & 3.7901 \\ -0.18626 & 0.18626 & 0.18626 & -0.18626 \\ 0.18626 & 0.18626 & -0.18626 & -0.18626 \\ 0.018623 & -0.018623 & 0.018623 & -0.018623 \end{bmatrix} \begin{bmatrix} \bar{\Omega}_1^2 \\ \bar{\Omega}_2^2 \\ \bar{\Omega}_3^2 \\ \bar{\Omega}_4^2 \end{bmatrix}, \quad (6.10)$$

or

$$\begin{bmatrix} \bar{\Omega}_1^2 \\ \bar{\Omega}_2^2 \\ \bar{\Omega}_3^2 \\ \bar{\Omega}_4^2 \end{bmatrix} = \begin{bmatrix} 0.0660 & -1.3422 & 1.3422 & 13.4243 \\ 0.0660 & 1.3422 & 1.3422 & 13.4243 \\ 0.0660 & 1.3422 & -1.3422 & 13.4243 \\ 0.0660 & -1.3422 & -1.3422 & 13.4243 \end{bmatrix} \begin{bmatrix} u_0 \\ u_1 \\ u_2 \\ u_3 \end{bmatrix}. \quad (6.11)$$

With ignored dynamics of the motor, according to the derivation from the previous sections, the normalized input PWM signal to the motor can be estimated as

$$v_a = 10.20\bar{\Omega} + 28.17\bar{\Omega}^2, \quad (6.12)$$

$$\delta = \frac{1.0864v_a^2 - 0.7031}{v_s^2}. \quad (6.13)$$

With this backwards tracing structure, with the desired control force and torques  $u_0$  to  $u_3$ , one can easily trace the rotating speed,  $\bar{\Omega}$ , then to the equivalent analog voltage,  $v_a$ , and hence the required normalized PWM input,  $\delta$ , can be calculated by compensating the battery voltage,  $v_s$ .

## 6.2 Feedback Linearization

By assigning a linearization feedback

$$u_1 = J_x \bar{u}_1 - (J_y - J_z)rq, \quad (6.14)$$

$$u_2 = J_y \bar{u}_2 - (J_z - J_x)pr, \quad (6.15)$$

$$u_3 = J_z \bar{u}_3 - (J_x - J_y)pq, \quad (6.16)$$

we can approximate a linear system for each channel, given by

$$\begin{bmatrix} \dot{\phi} \\ \dot{p} \end{bmatrix} = \begin{bmatrix} 0 & 1 \\ 0 & 0 \end{bmatrix} \begin{bmatrix} \phi \\ p \end{bmatrix} + \begin{bmatrix} 0 \\ 1 \end{bmatrix} \bar{u}_1, \quad (6.17)$$

$$\begin{bmatrix} \dot{\theta} \\ \dot{q} \end{bmatrix} = \begin{bmatrix} 0 & 1 \\ 0 & 0 \end{bmatrix} \begin{bmatrix} \theta \\ q \end{bmatrix} + \begin{bmatrix} 0 \\ 1 \end{bmatrix} \bar{u}_2, \quad (6.18)$$

$$\begin{bmatrix} \dot{\psi} \\ \dot{r} \end{bmatrix} = \begin{bmatrix} 0 & 1 \\ 0 & 0 \end{bmatrix} \begin{bmatrix} \psi \\ r \end{bmatrix} + \begin{bmatrix} 0 \\ 1 \end{bmatrix} \bar{u}_3. \quad (6.19)$$

Similarly for height dynamic,

$$m\dot{w} = mg \cos \theta \cos \phi - u_0 - m(vp + uq). \quad (6.20)$$

Since we could not obtain linear velocity measurements on-board, the latter terms are ignored. This is a valid assumption for non-aggressive flight as the velocity and angular velocity of the MAV will be close to 0. With linearization feedback, we have

$$m\bar{u}_0 = u_0 - mg \cos \theta \cos \phi, \quad (6.21)$$

and we can approximate a linear system for height control

$$\begin{bmatrix} \dot{z} \\ \dot{\omega} \end{bmatrix} = \begin{bmatrix} 0 & 1 \\ 0 & 0 \end{bmatrix} \begin{bmatrix} z \\ \omega \end{bmatrix} + \begin{bmatrix} 0 \\ -1 \end{bmatrix} \bar{u}_0, \quad (6.22)$$

$$(6.23)$$

### 6.3 Inner Loop Design

As each channel of the MAV's inner-loop system is a decoupled linear system, we can now consider the optimal regulator problem that, given the system equation

$$\dot{\mathbf{x}} = \mathbf{A}\mathbf{x} + \mathbf{B}\mathbf{u}, \quad (6.24)$$

we can obtain a matrix  $\mathbf{K}$  of the optimal control vector

$$\mathbf{b}(t) = -\mathbf{K}\mathbf{x}(t) \quad (6.25)$$

such that the performance index

$$J = \int_0^{\infty} (\mathbf{x}^T \mathbf{Q} \mathbf{x} + \mathbf{u}^T \mathbf{R} \mathbf{u}) dt \quad (6.26)$$

is minimized. Here,  $\mathbf{Q}$  is a positive-semidefinite Hermitian matrix, and  $\mathbf{R}$  is a positive-definite Hermitian matrix. These matrices determine the relative importance of the error and the expenditure of the energy of the control signals. We can then design the LQR controller by choosing appropriate  $\mathbf{Q}$  and  $\mathbf{R}$  matrices.

With the chosen  $\mathbf{Q}$  and  $\mathbf{R}$  matrices, a positive-definite matrix  $\mathbf{P}$  can be obtained as the solution to the Riccati equation

$$\mathbf{A}^T \mathbf{P} + \mathbf{P} \mathbf{A} - \mathbf{P} \mathbf{B} \mathbf{R}^{-1} \mathbf{B}^T \mathbf{P} + \mathbf{Q} = \mathbf{0}. \quad (6.27)$$

Then, the optimal feedback gain matrix  $\mathbf{K}$  is obtained as

$$\mathbf{K} = \mathbf{R}^{-1}\mathbf{B}^T\mathbf{P}. \quad (6.28)$$

## 6.4 Outer Loop Design

To further investigate the performance of the micro quadrotor, a position controller is proposed. In order to realize it, global position measurement need to be obtained for feedback control. For this micro quadrotor, as it is designed for indoor navigation, no GPS sensor is installed in the system. In our solution, we utilize an external sensor source called the Vicon motion sensor installed on the wall of the building to provide an estimation of the UAV's local position in the building. The estimated measurement is accurate up to a bounded error of 0.1 mm. The Vicon system setup will be mentioned in the next section.

By treating the closed inner-loop and its command generator as a virtual actuator (see [12]), the outer-loop dynamics of the aircraft can be treated separately into 3 channels, namely the  $x$ -,  $y$ - and  $z$ -channels, individually without considering the coupling effect between the channels in the system. Thus in such situation, the dynamical equation of any one of the channel, for example the  $x$ -channel, can be expressed as

$$\begin{bmatrix} \dot{x}_n \\ \dot{u}_n \end{bmatrix} = \begin{bmatrix} 0 & 1 \\ 0 & 0 \end{bmatrix} \begin{bmatrix} x_n \\ u_n \end{bmatrix} + \begin{bmatrix} 0 \\ 1 \end{bmatrix} a_{x,n}, \quad (6.29)$$

where  $x_n, v_n, a_{x,n}$  are respectively the NED position, velocity and acceleration in  $x$ -direction. By applying the RPT approach introduced in [71], we can obtain an augmented system of the

following form:

$$\dot{\mathbf{x}} = \mathbf{A}\mathbf{x} + \mathbf{B}\mathbf{u} + \mathbf{E}\mathbf{w}, \quad (6.30)$$

$$\mathbf{y} = \mathbf{x}, \quad (6.31)$$

$$\mathbf{e} = \mathbf{C}_2\mathbf{x}, \quad (6.32)$$

where

$$\mathbf{x} = \begin{bmatrix} x_{n,r} \\ u_{n,r} \\ a_{x,n,r} \\ x_n \\ u_n \end{bmatrix}, \quad \mathbf{w} = \dot{a}_{x,n,r}, \quad (6.33)$$

$$\mathbf{A} = \begin{bmatrix} 0 & 1 & 0 & 0 & 0 \\ 0 & 0 & 1 & 0 & 0 \\ 0 & 0 & 0 & 0 & 0 \\ 0 & 0 & 0 & 0 & 1 \\ 0 & 0 & 0 & 0 & 0 \end{bmatrix}, \quad \mathbf{B} = \begin{bmatrix} 0 \\ 0 \\ 0 \\ 0 \\ 1 \end{bmatrix}, \quad \mathbf{E} = \begin{bmatrix} 0 \\ 0 \\ 1 \\ 0 \\ 0 \end{bmatrix}, \quad (6.34)$$

$$\mathbf{C}_2 = \begin{bmatrix} -1 & 0 & 0 & 1 & 0 \end{bmatrix}. \quad (6.35)$$

Here, state variables with subscript  $r$  represent the reference signals that aircraft is tracking.

With this configuration, we can obtain a closed-form solution for the state feedback gain for the



system that solves the RPT control problem, given by

$$u = \mathbf{F}x, \quad (6.36)$$

with

$$\mathbf{F} = \begin{bmatrix} -\frac{\omega_{n,x}^2}{\epsilon_x^2} & -\frac{2\zeta_x\omega_{n,x}}{\epsilon_x} & \frac{\omega_{n,x}^2}{\epsilon_x^2} & \frac{2\zeta_x\omega_{n,x}}{\epsilon_x} & 1 \end{bmatrix}, \quad (6.37)$$

where  $\epsilon_x$  is the tuning parameter,  $\omega_{n,x}$  and  $\zeta_x$  are respectively the nominal natural frequency and damping ratio of the closed-loop system of  $x$ -axis dynamic. Similarly with the same procedure, the controllers of the  $y$ - and  $z$ -channels are designed and implemented.

## 6.5 Flight Control Simulation

Once the mathematical model is derived and the controllers are design, a simulator is programmed in MATLAB for controller fine-tuning. The simulator incorporate the derived MAV dynamics shown in Chapter 5 together with the control structure proposed in the previous sections. As the system can be separated into three controllable second order linear system, LQR design can be easily done. Fig. 6.2 shows the simulated angles and angular rates responses of the controlled MAV system with step inputs.

## 6.6 Flight Control Verification

In practice, the simulated controlled system does not guarantee to behave as good in actual world. A best way to fine-tune the control law design of the MAV is through physical flight test.

A full autonomous MAV control, including three-degree orientation control and three-degree translational control, is realized in the presence of Vicon motion tracking system. In this system, several infrared cameras (see Fig. 6.3) are installed around the flyable area of the closed room, where they are used to detect reflective markers mounted on the aircraft fuselage. The system

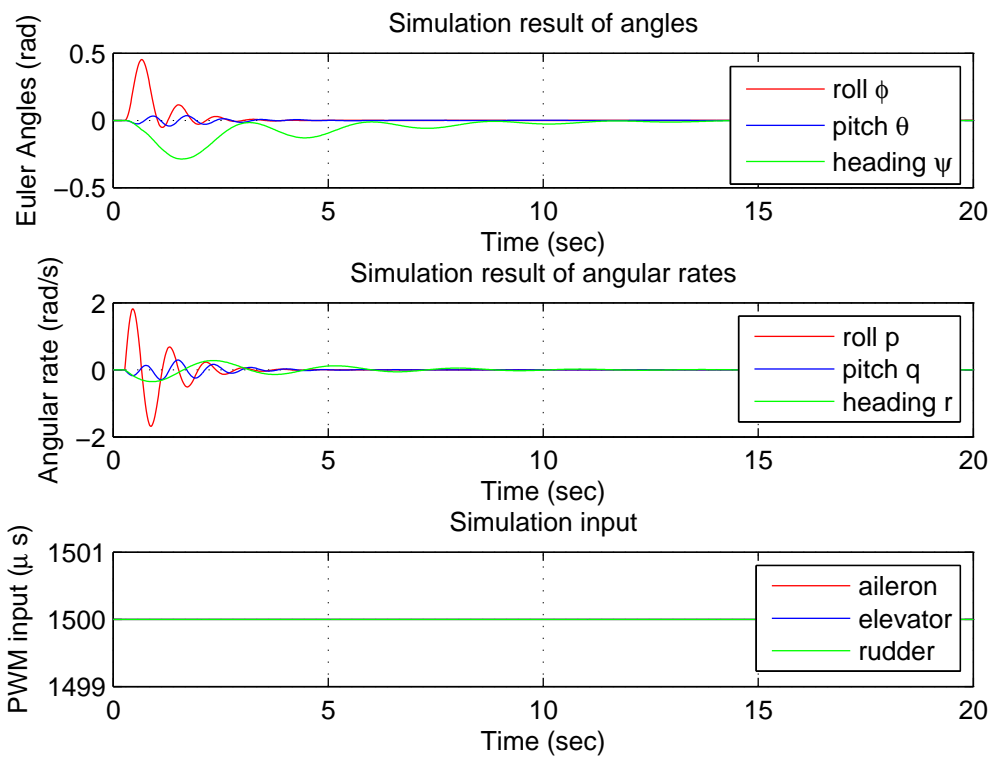


**Figure 6.2:** Simulated responses of the MAV orientation control system



**Figure 6.3:** A single infrared Vicon camera

then estimate the orientation and position of the aircraft, based on the estimated positions of the reflective markers. In the Vicon setup in the National University of Singapore (NUS) as shown in Fig. 6.4, 10 cameras are used to provide up to 0.1 mm accuracy of the estimated position of the markers. The position information is then sent up to the quadrotor MAV for further processing to realize position control and trajectory tracking.

The quadrotor is commanded to track a square path with 3.6 meters side length in one experiment, while tracking a zigzag path in the second experiment. The orientation of the quadrotor was stabilized with an LQR controller, while the position control of the MAV is realized in RPT control structure. The position responses of the autonomous system in both flight tests are shown in Fig. 6.5 and Fig. 6.6. The MAV is able to track the  $x$ - and  $y$ -positions fairly well, while remains  $\pm 5$  cm error on the  $z$ -position. This difference is due to the dynamics of the difference channel, as the  $x$ - and  $y$ -channels' dynamics are much higher than the  $z$ -channel's, and thus more prone to surrounding noise.

Besides realizing the flight control in the Vicon system, the MAV has also realized au-

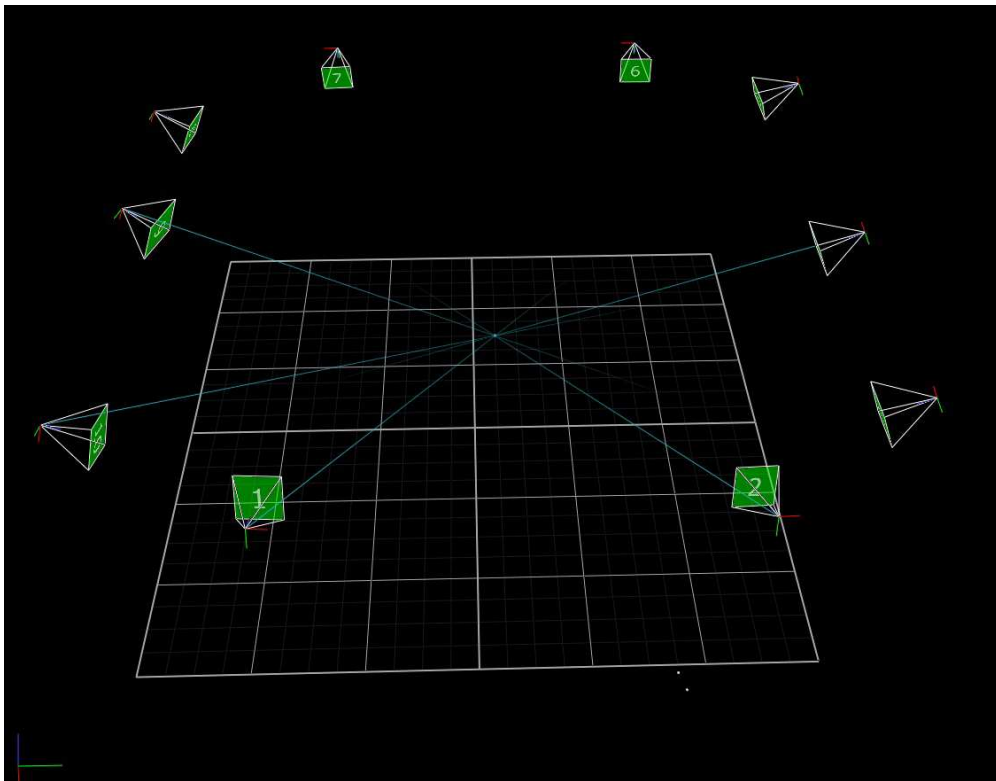


**Figure 6.4:** The Vicon system setup

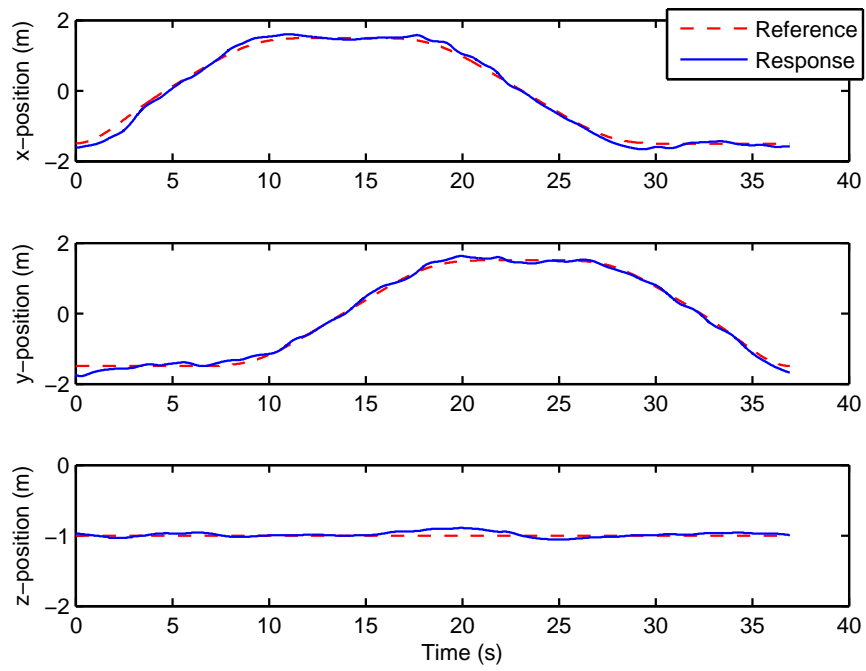


**Figure 6.5:** Position reference and response of the quadrotor in full autonomous square path

tonomous flight with mono vision sensor. The algorithm and results are documented in [41].

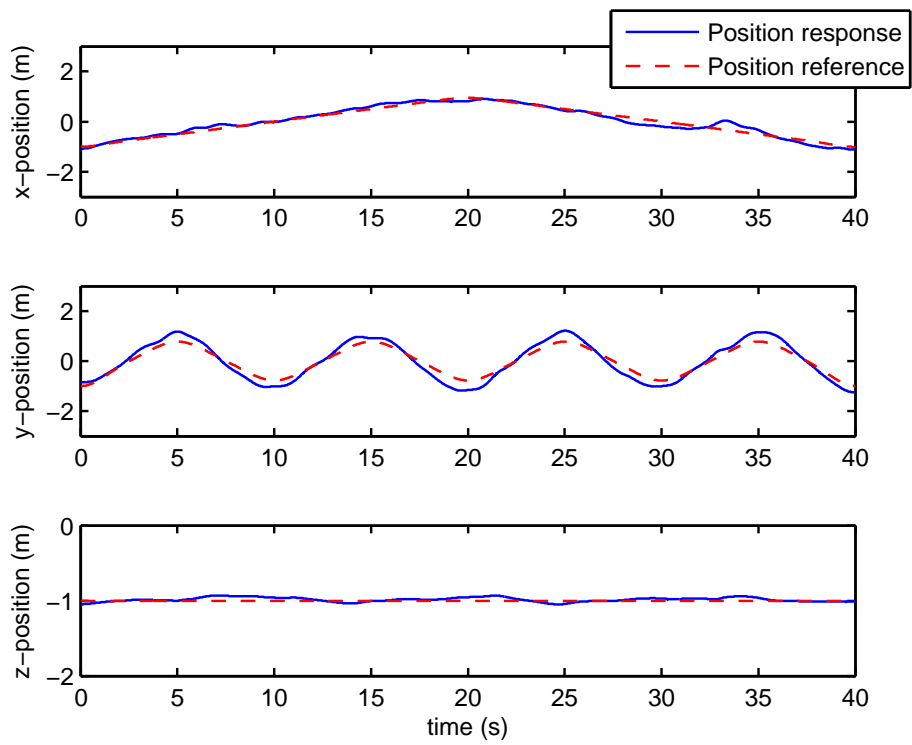


**Figure 6.6:** Position reference and response of the quadrotor in full autonomous zigzag path

## Chapter 7

# Trajectory Planning

### 7.1 Introduction

Once the control problems are solved, the next layer of intelligent autonomous navigation is the flight trajectory reference generation. In order to formulate a trajectory that could be tracked precisely, it is necessary to consider the vehicle's dynamic. As shown in [45,47], the quadrotor is a differential flat system with the flat outputs:

$$\sigma = [x, y, z, \psi]^T, \quad (7.1)$$

where  $\mathbf{P}_n = [x, y, z]^T$  denote the position of the center of mass and the  $\psi$  is the heading angle of the vehicle. Specifically, since a quadrotor MAV can navigate to any direction without the turn of its heading, there is no need to alternate the heading angle at all time. Therefore, the smooth trajectory of the MAV could be represented by the sub-space of the flat outputs with a constant heading angle given by

$$\mathbf{P}_n(t) : [t_{\text{ini}}, t_{\text{end}}] \longrightarrow \mathbb{R}^3, \quad (7.2)$$

where  $t_{\text{ini}}$  and  $t_{\text{end}}$  denote the initial and final time of the desired trajectory. The trajectory requires at least  $C_2$  smoothness as its feasibility as input to the vehicle is determined by its derivatives of different orders. As a differential flat system, it is sufficient to limit the maximum acceleration or thrust of the vehicle by considering the dynamic of the MAV in generating a reference path. According to the work in [51], the feasibility condition of the vehicle's thrust is constrained by

$$\max \left\{ \sum_{i=1}^3 (\ddot{p}_i(t) - g_i)^2 \right\} \leq f_{\text{max}}^2, \quad \forall t \in [t_{\text{ini}}, t_{\text{end}}], \quad (7.3)$$

where  $p_1 = x, p_2 = y, p_3 = z, g$  is gravity vector and  $f_{\text{max}}$  is the maximum allowable thrust.

To further simplify the formulation, aggressive maneuvering is assumed not necessary. The constraint on vehicle's thrust is thus split into three individual axis to enhance the computation speed. The constraint can be simplified to

$$\max \{ (\ddot{p}_i(t) - g_i)^2 \} \leq \alpha_i^2, \quad \forall t \in [t_{\text{ini}}, t_{\text{end}}], \quad (7.4)$$

where  $i \in \{1, 2, 3\}$  and  $\alpha_i$  satisfies

$$\sum_{i=1}^3 \alpha_i^2 \leq f_{\text{max}}^2. \quad (7.5)$$

It has been proven in [45] that the upper bound of the norm of the vehicle's body angular rates is proportional to the norm of trajectory's jerk (derivative of the acceleration) as

$$\bar{\omega}^2 = \frac{\sum_{i=1}^3 \max_{t \in [t_{\text{ini}}, t_{\text{end}}]} j_i(t)^2}{\sum_{i=1}^3 \min_{t \in [t_{\text{ini}}, t_{\text{end}}]} (\ddot{p}_i(t) - g_i)^2}, \quad (7.6)$$

where  $j_1, j_2,$  and  $j_3$  are the corresponding jerk of the trajectory in  $x$ -,  $y$ - and  $z$ -axis. In order to achieve a smooth response from the vehicle, a minimum jerk trajectory is naturally considered.

The trajectory planning of the MAV is strongly based on the basis mentioned above. In order to realize the trajectory generation for such system, we have divided the problem into



three different parts. Starting with the normalization of the uniform B-spline, followed by two approaches to solve the minimum jerk trajectory problem—a closed solution and the more practical quadratic programming solution.

## 7.2 Normalized Uniform B-Spline

The normalized uniform B-splines is named after its normalized and hence equally segmented knots vector. The base of the B-splines has been defined in [6] as a recursive function

$$N_{i,0}(u) = \begin{cases} 1, & \text{if } u_i \leq u < u_{i+1}, \\ 0, & \text{otherwise.} \end{cases} \quad (7.7)$$

$$N_{i,p}(u) = \frac{u - u_i}{u_{i+p} - u_i} N_{i,p-1}(u) + \frac{u_{i+p+1} - u}{u_{i+p+1} - u_{i+1}} N_{i+1,p-1}(u), \quad (7.8)$$

where  $N_{i,p}(u)$  is the basis function of the generally defined B-splines and  $[u_0, u_1, u_2, \dots]$  forms the knot vector of B-splines. Normalization of the uniform B-spline will thus produce the knot vector  $[0, 1, 2, 3, \dots]$ . A basis element function of a normalized uniform B-splines has been given in [69] as

$$T_{j,i}(s) = \begin{cases} 1, & \text{if } i = j = 0, \\ \frac{1-s}{i} T_{0,i-1}(s), & \text{if } j = 0, i \neq 0, \\ \frac{s}{i} T_{i-1,i-1}(s), & \text{if } j = i > 0, \\ \frac{i-j+s}{i} T_{j-1,i-1}(s) + \frac{1+j-s}{i} T_{j,i-1}(s), & \text{if } j = 1, \dots, i-1, \\ 0, & \text{otherwise.} \end{cases} \quad (7.9)$$

Thus, a spline function can then be expressed as

$$S_k(t) = \sum_{i=1}^M c_i B_k(t - i + 1), \quad c_i \in \mathbb{R}^3, \quad (7.10)$$

where

$$B_k(s) = \begin{cases} T_{k-j,k}(s-j), & j \leq s < j+1, \\ 0, & \text{otherwise.} \end{cases} \quad (7.11)$$

Here,  $j = 0, \dots, k$  where  $k$  denotes the order of the spline, and  $M$  denotes the number of user specified control points. Notice that in general path optimization,  $c_i$  are the trajectory points in 3D space to be optimized later. As we have broken down the trajectory to its components along  $x$ -,  $y$ - and  $z$ -directions,  $c_i$  becomes a scalar in our problem formulation, i.e.,  $c_i \in \mathbb{R}$ . Also, as the trajectory references fed to the outer-loop RPT controller mentioned in the previous chapter is up to the second derivatives of the positions (the accelerations), we can specifically formulate this optimization problem in third order, i.e.  $k = 3$ .

In order to arbitrarily specify the boundary conditions in our system, a cubic clamped normalized uniform B-spline is proposed. This customized B-spline has a knot vector in the form of  $[0, 0, 0, 0, 1, 2, 3, \dots, m-1, m, m, m, m]$ , where the first three and the last three bases corresponding to the vector elements of 0 and  $m$  are for the initial and the final conditions of the desired trajectory. Note that in our case,  $m = M - 1$ , and thus the knot vector has  $M + 6$  terms. From Equation (7.7), we could easily deduce the different basis accordingly. The expression of common basis element  $B_3(u)$  is given by

$$B_3(u) = \begin{cases} \frac{1}{6}u^3, & \text{if } u \in [0, 1), \\ \frac{1}{6} - \frac{1}{2}(u-1)^3 + \frac{1}{2}(u-1)^2 + \frac{1}{2}(u-1), & \text{if } u \in [1, 2), \\ \frac{1}{6} + \frac{1}{2}(u-3)^3 + \frac{1}{2}(u-3)^2 - \frac{1}{2}(u-3), & \text{if } u \in [2, 3), \\ -\frac{1}{6}(u-4)^3, & \text{if } u \in [3, 4), \\ 0, & \text{otherwise.} \end{cases} \quad (7.12)$$

whereas the initial three and the final three bases can be uniquely expressed as

$$N_{0,3}(u) = \begin{cases} (1-u)^3, & \text{if } u \in [0, 1), \\ 0, & \text{otherwise.} \end{cases} \quad (7.13)$$

$$N_{1,3}(u) = \begin{cases} u(1-u)^2 + \frac{u(4-3u)(2-u)}{8}, & \text{if } u \in [0, 1), \\ -\frac{(u-2)^3}{4}, & \text{if } u \in [1, 2), \\ 0, & \text{otherwise.} \end{cases} \quad (7.14)$$

$$N_{2,3}(u) = \begin{cases} \frac{u^2(-3u+4)}{4} + \frac{u^2(3-u)}{6}, & \text{if } u \in [0, 1), \\ \frac{u(u-2)^2}{4} + \frac{(3-u)(-2u^2+6u-3)}{6}, & \text{if } u \in [1, 2), \\ \frac{u^2(-3u+4)}{4} + \frac{u^2(3-u)}{6}, & \text{if } u \in [2, 3), \\ 0, & \text{otherwise.} \end{cases} \quad (7.15)$$

and

$$N_{M+3,3}(u) = N_{2,3}(-u + M - 1), \quad (7.16)$$

$$N_{M+4,3}(u) = N_{1,3}(-u + M - 1), \quad (7.17)$$

$$N_{M+5,3}(u) = N_{0,3}(-u + M - 1). \quad (7.18)$$

Finally, we can express the overall cubic spline in

$$S_3(t) = \sum_{i=-2}^0 c_i N_{i+2,3}(t) + \sum_{i=1}^M c_i B_3(t - i + 1) + \sum_{i=M+1}^{M+3} c_i N_{i+2,3}(t), \quad c_i \in \mathbb{R}, \quad (7.19)$$

for each individual channel in  $x$ -,  $y$ - and  $z$ -direction.

Now, there are  $M + 6$  control points where the first three and last three are used to determine the boundary conditions. Thus in general, if a new basis for the clamped spline is defined, the

cubic spline can be expressed as

$$S_3(t) = \sum_{i=0}^{M+5} \tau_i F_{i,3}(t), \quad \tau_i \in \mathbb{R}, \quad (7.20)$$

where

$$\begin{aligned} \tau_i &= c_{i-2}, \\ F_{i,3}(t) &= \begin{cases} N_{i,3}(t), & \text{if } i \in \{0, 1, 2, M+3, M+4, M+5\}, \\ B_3(t-i+3), & \text{otherwise.} \end{cases} \end{aligned} \quad (7.21)$$

### 7.3 Minimum Jerk Trajectory: Closed Solution

We can now formulate the problem of the minimum jerk trajectory based on the clamped normalized uniform B-spline. The formulation of the problem is similar to the documented works in [45] and [64] but with 6 additional clamped bases as the initial and the final conditions of the trajectory. If a set of sampled data points is given as

$$\begin{aligned} D &= \{d_i \in \mathbb{R} : i = 1, \dots, N\}, \\ T &= \{t_i \in \mathbb{R} : i = 1, \dots, N\}, \end{aligned} \quad (7.22)$$

where  $D$  is the set of 1D trajectory data points,  $T$  is the set of time indicating at what time each of the above data points are reached, and  $N$  is the total number of trajectory points to be optimized, then, the minimum jerk trajectory will be achieved by minimizing the criterion function

$$J = w_g \int_{-\infty}^{\infty} v^2(t) dt + \sum_{i=1}^N (S_3(t_i) - d_i)^2, \quad (7.23)$$

where  $w_g$  is a weighting factor, and

$$v(t) = \sum_{i=0}^{M+5} \frac{d^3}{dt^3} \tau_i F_{i,3}(t), \quad \tau_i \in \mathbb{R}, \quad (7.24)$$

is the third derivative of Equation (7.20).

It is further shown in [36] that  $\int_{-\infty}^{\infty} v^2(t)dt$  can be expressed as the form of  $\tau^T G \tau$ , where  $\tau = [\tau_0, \tau_1, \dots, \tau_{M+5}]^T$ , and  $G$  can be calculated explicitly. More specifically, the elements in  $G$  are

$$g_{i,j} = \alpha^5 \int_{-\infty}^{\infty} F_{i,3}^{(3)}(t) F_{j,3}^{(3)}(t) dt, \quad (7.25)$$

where  $\alpha = (M + 6)/T_{\text{true}}$  and  $T_{\text{true}} = t_{\text{end}} - t_{\text{ini}}$  is the total time of the trajectory. On the other hand, by letting

$$H = \begin{bmatrix} F_{0,3}(\alpha t_1) & F_{1,3}(\alpha t_1) & \dots & F_{M+5,3}(\alpha t_1) \\ F_{0,3}(\alpha t_2) & F_{1,3}(\alpha t_2) & \dots & F_{M+5,3}(\alpha t_2) \\ \vdots & \vdots & \ddots & \vdots \\ F_{0,3}(\alpha t_N) & F_{1,3}(\alpha t_N) & \dots & F_{M+5,3}(\alpha t_N) \end{bmatrix}, \quad (7.26)$$

we can express the second term of  $J$  as

$$\sum_{i=1}^N (S_3(t_i) - d_i)^2 = (H\tau - d)^T (H\tau - d), \quad (7.27)$$

with  $d = [d_1, d_2, \dots, d_N]^T$ . Note that the dimension of vector  $\tau$  and  $d$  are  $M + 6$  and  $N$  respectively.

Now, the minimization of the criterion function in Equation (7.23) can be reformulated as

$$J_{\min} = \min_{\tau} \{w_g \tau^T G \tau + (H\tau - d)^T (H\tau - d)\}. \quad (7.28)$$

However, in the clamped cubic spline, the first three and last three elements in  $\tau$  are used to determine the boundary condition. Therefore, they are fixed and should not be treated as optimization variable. Here, a transformation matrix  $U$  is used to separate the fixed part  $\tau_F$  and the

programmable part  $\tau_P$  of  $\tau$  as

$$U \begin{bmatrix} \tau_F \\ \tau_P \end{bmatrix} = \tau. \quad (7.29)$$

Then, Equation (7.28) can be rewrite as

$$J_{\min} = \min_{\tau_P} \left\{ \begin{bmatrix} \tau_F \\ \tau_P \end{bmatrix}^T w_g U^T G U \begin{bmatrix} \tau_F \\ \tau_P \end{bmatrix} + (H U \begin{bmatrix} \tau_F \\ \tau_P \end{bmatrix} - d)^T (H U \begin{bmatrix} \tau_F \\ \tau_P \end{bmatrix} - d) \right\}, \quad (7.30)$$

which can be further simplified to

$$J_{\min} = \min_{\tau_P} \left\{ \begin{bmatrix} \tau_F \\ \tau_P \end{bmatrix}^T (w_g U^T G U + U^T H^T H U) \begin{bmatrix} \tau_F \\ \tau_P \end{bmatrix} - 2d^T H U \begin{bmatrix} \tau_F \\ \tau_P \end{bmatrix} + d^T d \right\}. \quad (7.31)$$

By letting  $R = w_g U^T G U + U^T H^T H U$ ,  $S = d^T H U$  then partition  $R$  and  $S$  according to the dimensions of  $\tau_F$  and  $\tau_P$  as

$$R = \begin{bmatrix} R_{FF} & R_{FP} \\ R_{PF} & R_{PP} \end{bmatrix} \text{ and } S = [S_F, S_P], \quad (7.32)$$

Equation (7.31) can be expressed as

$$J_{\min} = \min_{\tau_P} \{ \tau_F^T R_{FF} \tau_F + \tau_F^T R_{FP} \tau_P + \tau_P^T R_{PF} \tau_F + \tau_P^T R_{PP} \tau_P - 2S_F \tau_F - 2S_P \tau_P + d^T d \}. \quad (7.33)$$

By taking the first derivative with respect  $\tau_P$ , we will obtain the optimal values for the programmable part in a closed form as

$$\tau_P^* = R_{PP}^{-1} (S_P^T - R_{FP}^T \tau_F). \quad (7.34)$$

By using the optimal  $\tau_P$ , one could easily reconstruct the control points vector and the B-spline using the de Boor's algorithm [6].

## 7.4 Minimum Jerk Trajectory: Quadratic Programming

Although there is a closed solution for the minimum jerk trajectory, it is usually not advisable in real application as the dimension of the solution matrices are too large to be computed efficiently. On the other hand, taking a closer look at Equation (7.28), it is a typical quadratic optimization problem which could be solved efficiently using off-the-shelf optimization solvers such as *quadprog* from MATLAB or *CPLEX* from IBM. Also by considering the problem as a general optimization problem, it allows us to add more constraints on the trajectory, such as the maximum velocity or acceleration.

As the MAVs are designed to fly in-door, the flyable area is limited. The velocity of the vehicle will naturally be restricted, it is reasonable to only limit the acceleration of the MAV. For generality, the numerical method presented in this manuscript is also suitable to explicitly limit derivatives of any degrees that is smaller than the order of the B-spline basis.

Reformulating Equation (7.28), we get

$$J_{\min} = \min_{\tau} \{ \tau^T (w_g G + H^T H) \tau - 2d^T H \tau + d^T d \}. \quad (7.35)$$

Note that  $w_g G + H^T H$  is always positive semi definite which guarantees a unique minimum of the quadratic programming problem. Now, in order to constraint the derivatives, we first express the derivatives of the trajectory. Taking the first derivative of the B-spline trajectory in Equation (7.20), we have

$$\frac{dS_3(t)}{dt} = \sum_{i=0}^{M+4} \eta_i F_{i+1,2}(t), \quad (7.36)$$

where

$$\eta_i = \frac{3}{t_{i+4} - t_{i+1}}(\tau_{i+1} - \tau_i). \quad (7.37)$$

According to [35], to limit maximum and minimum value of the derivative trajectory, a sufficient condition is to let

$$\dot{S}_{3,\min} \leq \eta_i \leq \dot{S}_{3,\max}, \quad \forall i = \{0, 1, \dots, M + 4\}. \quad (7.38)$$

Since here we are focusing on the constraint of acceleration, the second order derivative of the original trajectory is examined. From the Equation (7.36), one can easily compute a matrix  $L$  as

$$L = \alpha^2 \begin{bmatrix} 6 & -9 & 3 & 0 & 0 & \dots & 0 & 0 & 0 \\ 0 & \frac{3}{2} & \frac{-5}{2} & 1 & 0 & \dots & 0 & 0 & 0 \\ 0 & 0 & 1 & -2 & 1 & 0 & \dots & 0 & 0 \\ 0 & 0 & 0 & 1 & -2 & 1 & 0 & \dots & 0 \\ & & & & \dots & & & & \\ 0 & 0 & \dots & 0 & 1 & -2 & 1 & 0 & 0 \\ 0 & 0 & \dots & 0 & 0 & \frac{3}{2} & \frac{-5}{2} & 1 & 0 \\ 0 & 0 & \dots & 0 & 0 & 0 & 6 & -9 & 3 \end{bmatrix}.$$

We can then project the acceleration constraints into the constraints of control points vector  $\tau$  as

$$\ddot{S}_{3,\min} \leq L_i \tau \leq \ddot{S}_{3,\max}, \quad \forall i = \{0, 1, \dots, M + 5\}, \quad (7.39)$$

where  $L_i$  denotes the  $i$ 's row of  $L$ . To satisfy the boundary condition, one should fix the first three and last three elements of  $\tau$ . This could be easily formed as an equality constraints of the form

$$A_{\text{eq}} \tau = b_{\text{eq}}, \quad (7.40)$$



where

$$A_{\text{eq}} = \begin{bmatrix} I_3 & 0 & 0 \\ 0 & \ddots & 0 \\ 0 & 0 & I_3 \end{bmatrix}.$$

Equations (7.35), (7.39), and (7.40) form a typical convex quadratic programming problem which can be solved numerically in an efficient manner [53].

## 7.5 Implementation on Ground Station

Once the trajectory generation is formulated, it is implemented on a ground station running MATLAB. In order ease the operator's task of selecting waypoints for the MAV, a simple user interface is developed. In this interface, the operator is to manually click the waypoints on the coordinate plane which represented the  $x$ - and  $y$ -direction of the ground. Fig. 7.7 shows an example of simple 2 waypoints selected by the operator (the red dots). Once the waypoints are selected, MATLAB will run a quadratic programming solver to obtain an optimal solution to the minimum jerk trajectory problem with the waypoints as the initial state and final state respectively. A trajectory will then be generated (blue line in the same figure) while the accelerations and velocities of the path will be displayed as shown in Fig. 7.2.

The software is able to input as many waypoints as the operator wish to. Other examples of different path patterns generation, such as square path, circular path, and zigzag path, are shown in Fig. 7.3 to Fig. 7.8. Based on the accelerations and velocities generated, the trajectory is of  $C_2$  smoothness as discussed earlier in this chapter. The minimum jerk trajectory ensure a smooth trajectory and even velocity references such that the quadrotor MAV is able to track well. As soon as the path is generated, the trajectory reference together with its velocity and acceleration references will be sent to the aircraft to start navigating.

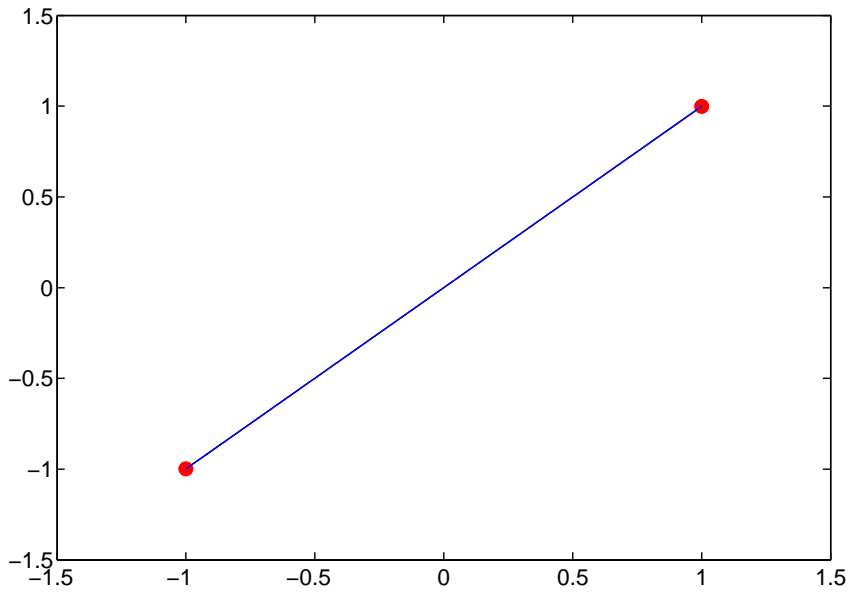


**Figure 7.1:** Straight path drawn in MATLAB

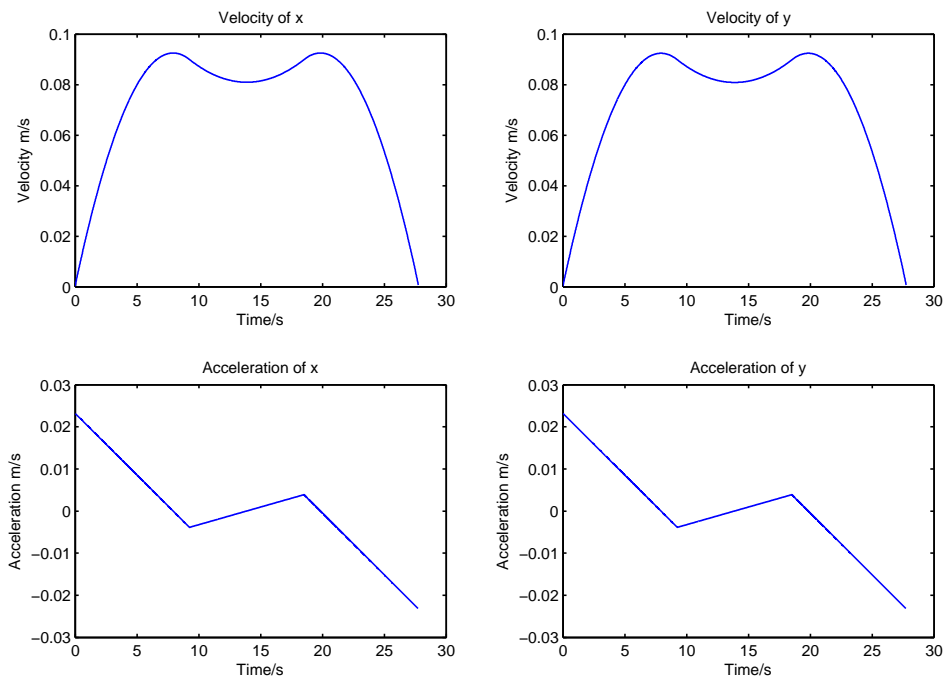


**Figure 7.2:** Acceleration and velocity references generated for a straight path

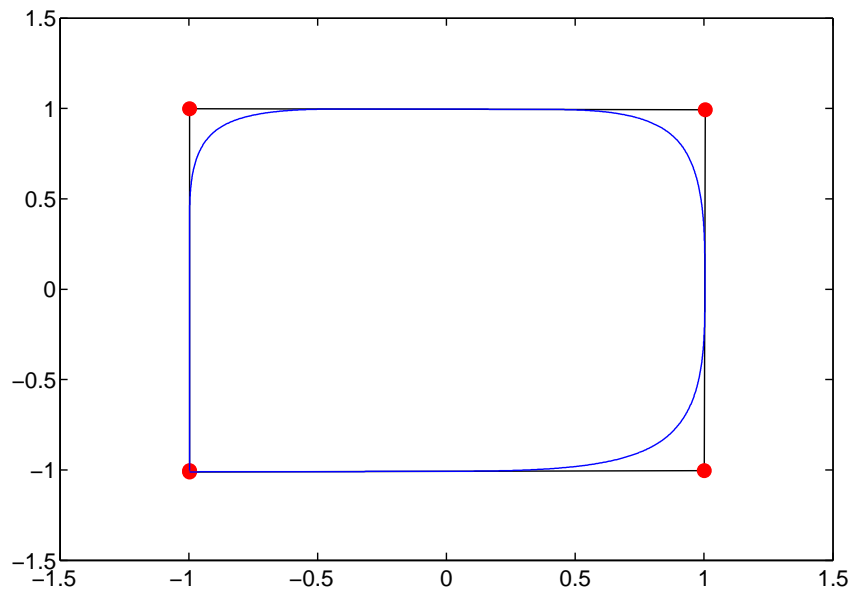


**Figure 7.3:** Square path drawn in MATLAB

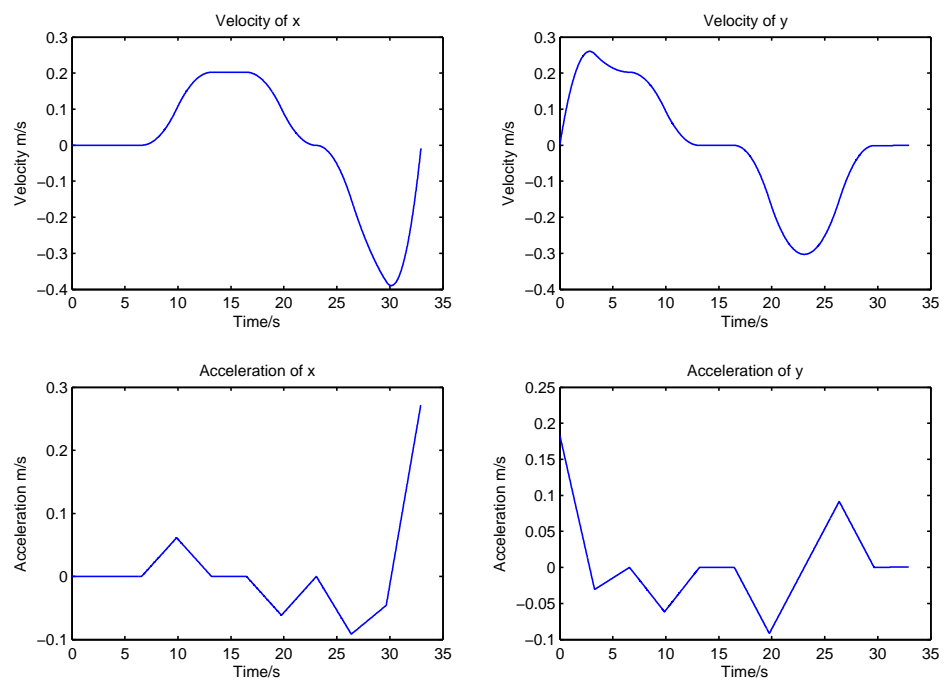


**Figure 7.4:** Acceleration and velocity references generated for a square path

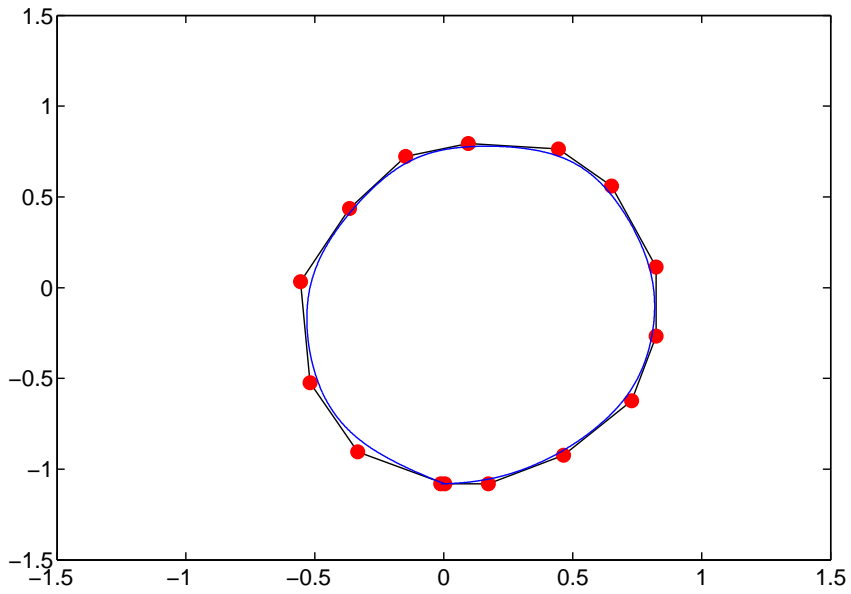


**Figure 7.5:** Circular path drawn in MATLAB

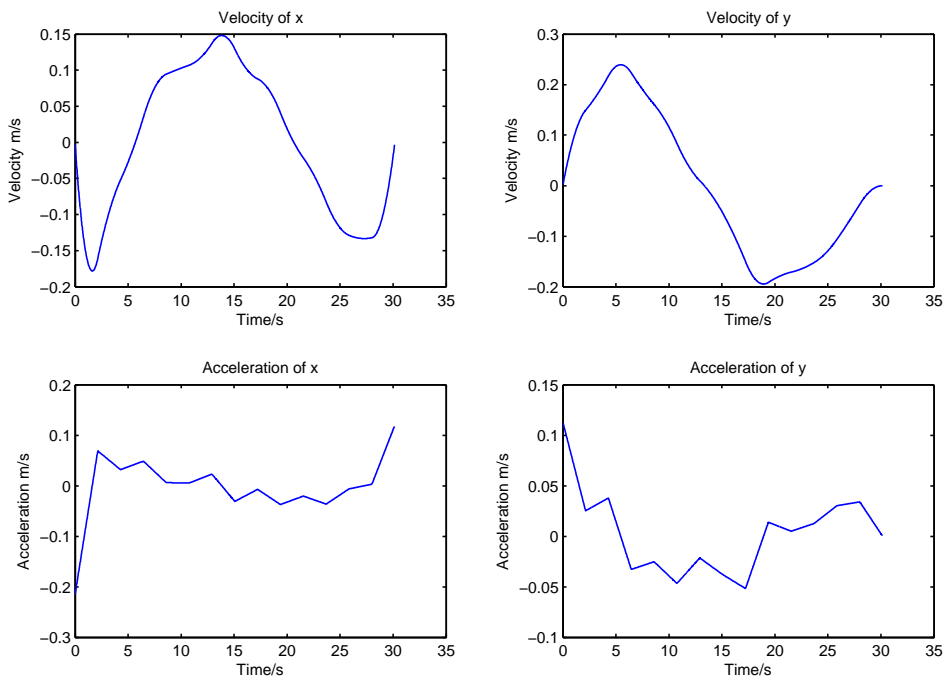


**Figure 7.6:** Acceleration and velocity references generated for a circular path

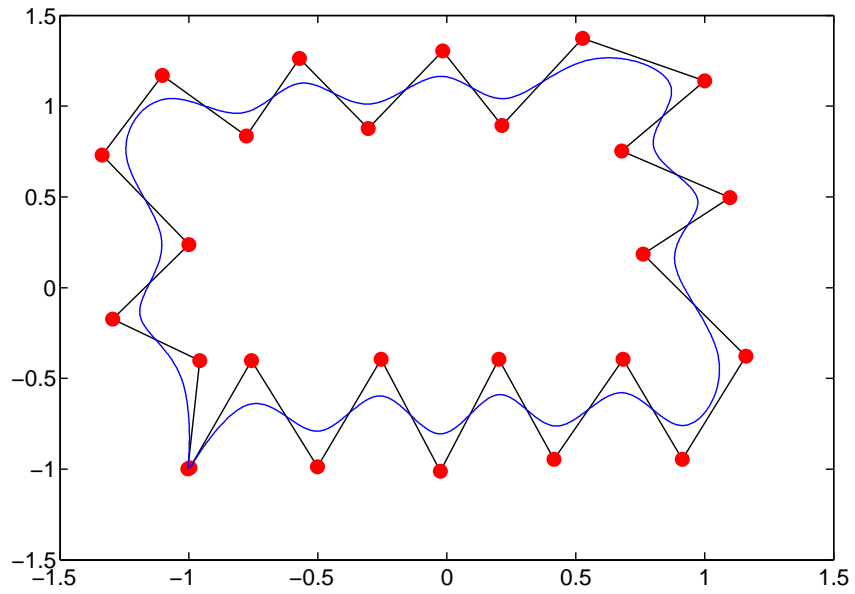


**Figure 7.7:** Random zigzag path drawn in MATLAB

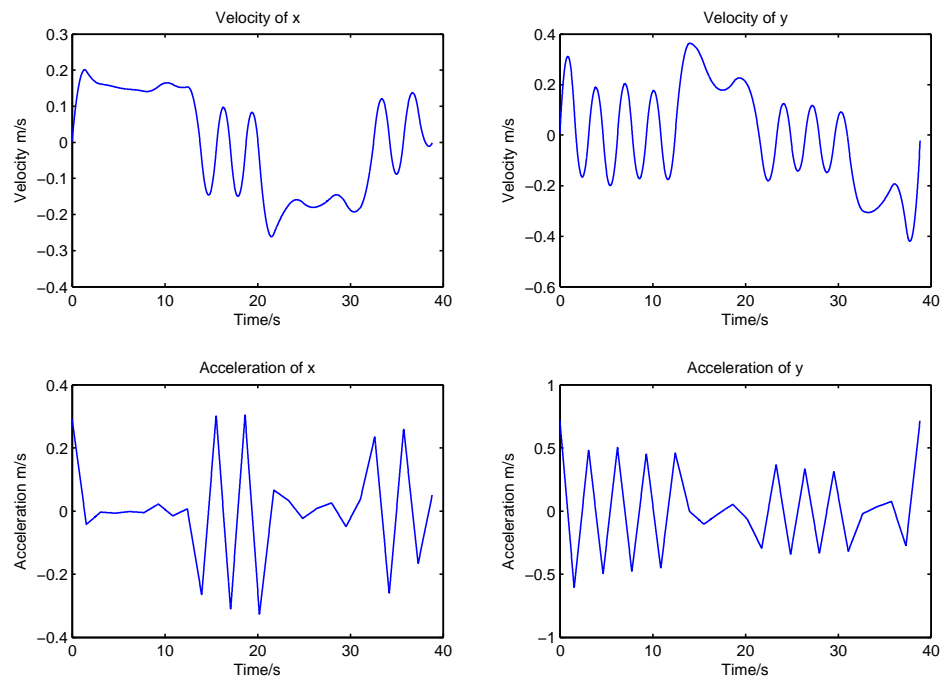


**Figure 7.8:** Acceleration and velocity references generated for a zigzag path



## Chapter 8

# Case Study: UAV Calligraphy

### 8.1 Introduction

There are a wide range of application for the developed MAV as it is tiny and suitable for indoor navigation. In February 2014, the NUS UAV Research Group is selected to put up a performance on one application of MAV in Singapore Airshow 2014. Singapore Airshow is one of the world's largest aviation event held biyearly in Singapore. It has attracted exhibitors from more than 50 countries to participate and to showcase their development in aviation sector.

After much consideration, we have decided to put up an entertaining flight show that showcases the capability of autonomous calligraphy writing with MAVs [56]. This performance presents a few new challenges to the developed MAV:

1. Hardware changes needed to incorporate a calligraphy brush holder to the bottom of the MAVs;
2. Algorithms to extract user handwritten characters and then transform it to important turning points for further path generation;
3. Generated trajectory needs to be further optimized on flight time to speed up the writing process.

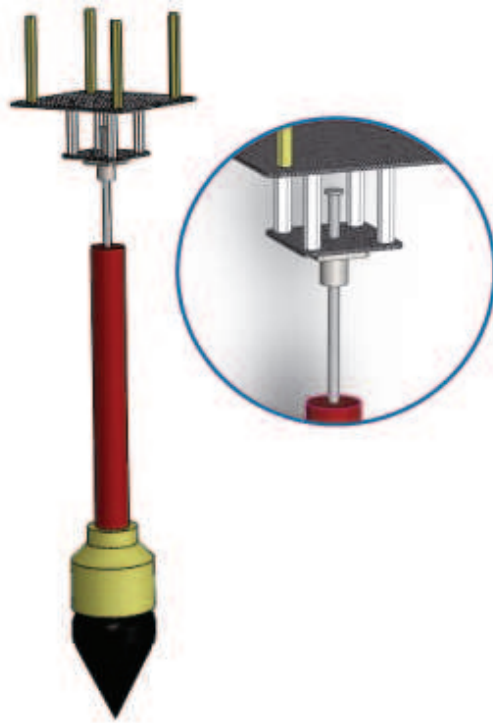


**Figure 8.1:** The designed calligraphy brush and its holder

In this chapter, the realization of the calligraphy writing by MAV will be discussed. Solution to each of the challenges listed above will be discussed in the following sections.

## 8.2 Hardware Setup

To realize calligraphy writing, a calligraphy brush together with the holding mechanism is customized. The full overview design of the brush can be visualized in Fig. 8.1. More specifically, the author wish to highlight an important design consideration to realize the system—the linear bearing joint (zoomed view in Fig. 8.1). A linear bearing is included at the base of the brush holder, while a shaft attached to the brush passes through and is locked to the bearing. The installation of such a mechanism enables

1. A free low-friction linear movement along  $z$ -direction of the brush with reference to the



MAV above it. This reduces the disturbance to the airborne MAV resulted from the contact between the calligraphy brush and the writing board. Performance of the MAV will thus not be affected during the contact-writing instances;

2. The calligraphy brush can be rotated freely along  $z$ -axis, resulting smooth and natural writing along an arc or circular drawing.

Next, an accurate position sensor is needed for each quadrotor to track the generated trajectory precisely. Here in this calligraphy writing performance, the accuracy of the MAV position measurement is the prime factor affecting the writing result. As the MAVs will write in a controlled environment, an external source of accurate object position estimation is used. A Vicon motion sensing system is set up for this purpose. Working principle of the system has been previously mentioned in Chapter 6. A total of 36 Vicon cameras are installed to the system to provide object position estimation with a resolution up to 0.01 mm. With such accuracy, the performance of the MAV boils down to its trajectory tracking and position control accuracy.

### 8.3 Handwriting Extractions

As the performance allows any user to have their handwritten characters to be written out by the MAVs, a user interface to extract the handwriting data is developed in MATLAB (see Fig. 8.2). User can simply write any Chinese character or English word on the space provided in the software using a styler. In order to perform regression and rebuild a flyable reference trajectory, the original user input is sampled by finding the more *meaningful* points. Here, the *meaningful* points refer to the starting, ending and turning points where they usually form the skeleton of the handwriting. To determine the turning points in a sequenced 2D points set, a split-and-merge algorithm is applied to divide these 2D points into individual line segments. The turning points will then be assigned to the endpoints of these line segments [7]. The original sequenced 2D points set is acquired by recording user's handwritten input through a tablet via an interface application we have created. They are sorted in the chronological order and sent to the ground

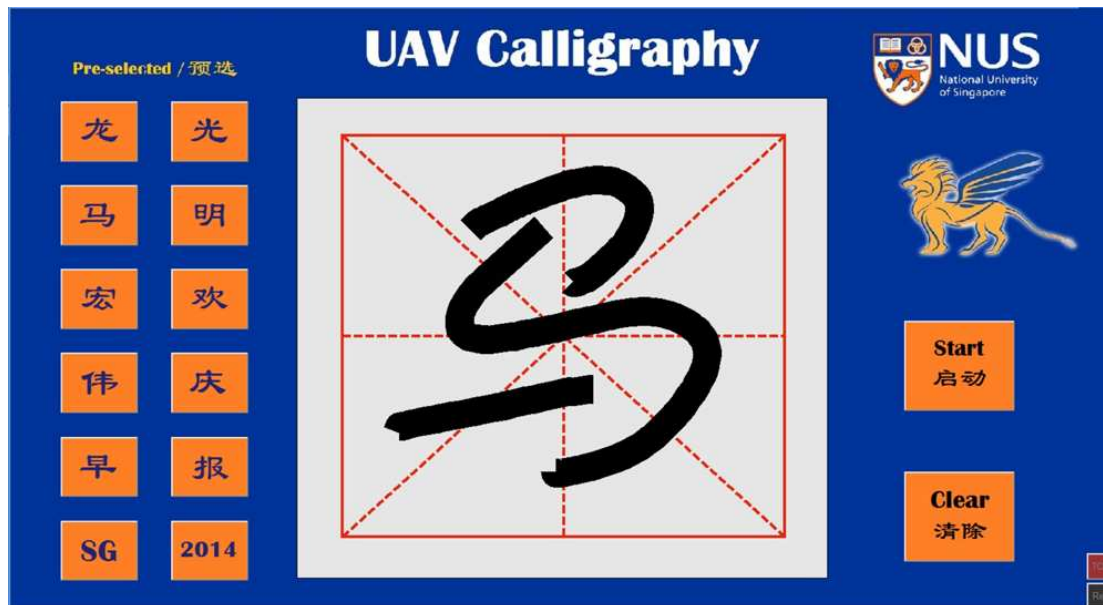


**Figure 8.2:** Graphical interface for user handwriting input

station for turning point extractions.

The algorithm is illustrated in Fig. 8.3. The sequence of the split-and-merge algorithm is as follows:

1. Connect the first point A and the last point B.
2. Find point C among all data points that has the longest perpendicular distance to line A-B.
3. If this longest distance is within a threshold, then a cluster is created containing points between A and B.
4. Else, the input points will be split into two sub-groups, A-C and C-B. For each sub-group, the split-and-merge algorithm will be called recursively.
5. The algorithm stops when all longest distance fall inside the preset threshold.

Finally, the algorithm will return all the endpoints of the resulted point-sub-groups in their original chronological order. All these endpoints are used to run a B-spline based regression to generate a reference trajectory under the constraints of MAV dynamics.

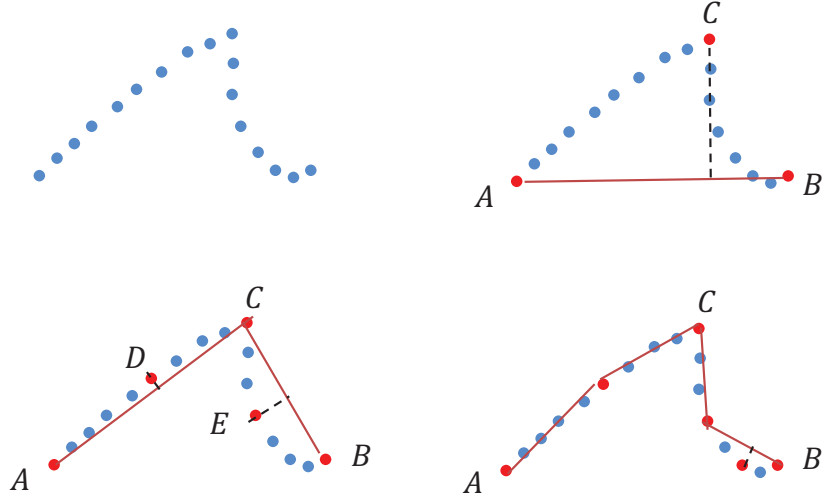


**Figure 8.3:** Split-and-merge sequence on continuous line segments

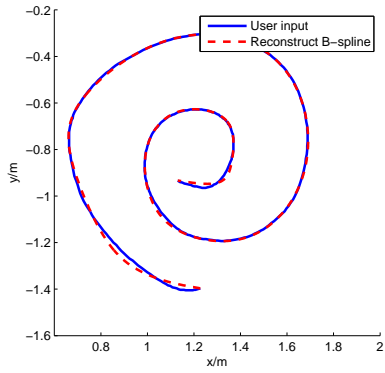
## 8.4 Trajectory Generating: Optimal Time Segmentation

The trajectory generation algorithm is similar to the minimum jerk trajectory optimization shown in Chapter 7. However, due to the initial and final points extracted via split-and-merge algorithm mentioned in the previous section, the time information of each extracted points cannot be obtained. An additional time re-segmentation algorithm is implemented to update the time-stamp of each extracted points while iteratively optimize the trajectory based on minimum jerk optimization.

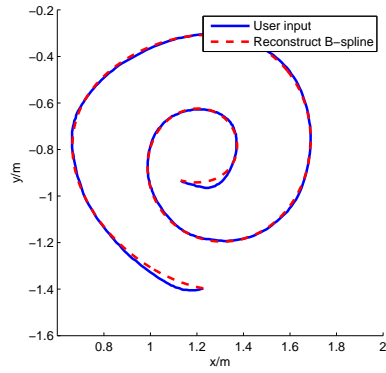
Let  $T_i = t_{i+1} - t_i$  be the new programmable variables, then a new optimization problem is formulated as

$$\min f(\mathbf{T}), \quad \text{s.t. } T_i > 0. \quad (8.1)$$

where  $f(\mathbf{T})$  is the optimal solution to Equation (7.35) for time segment  $\mathbf{T} = [T_1, T_2, \dots, T_{N-1}]^T$ . This problem can be solved via a gradient descent method [45] by calculating the gradient vector

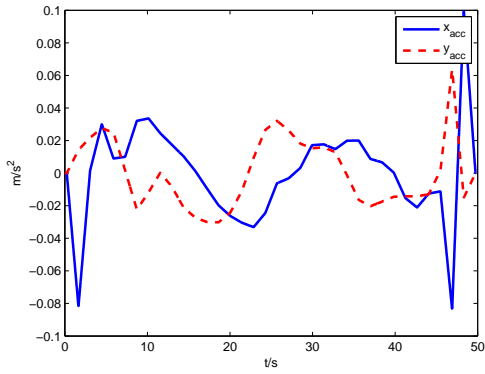


(a) Without time re-segmentation

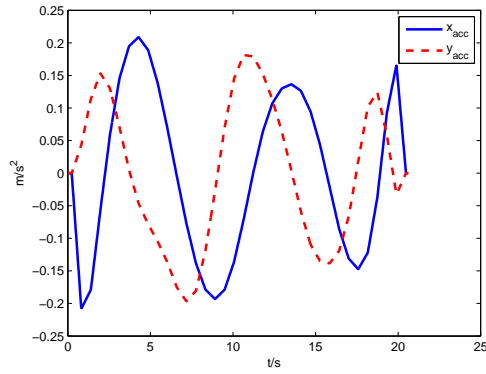


(b) With time re-segmentation

**Figure 8.4:** User input and generated spline of vortex drawing

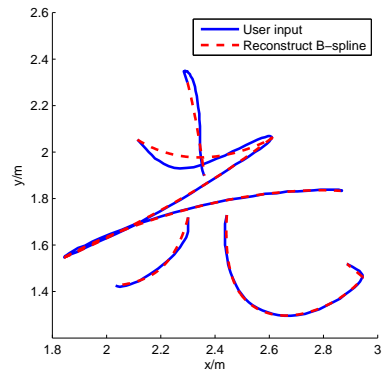


(a) Without time re-segmentation

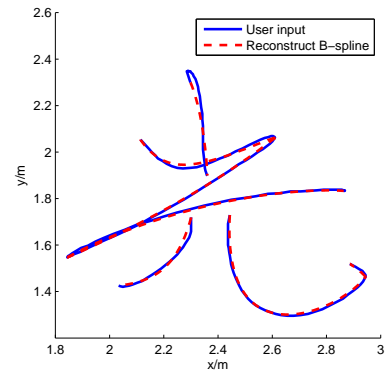


(b) With time re-segmentation

**Figure 8.5:** Generated spline's acceleration of vortex drawing

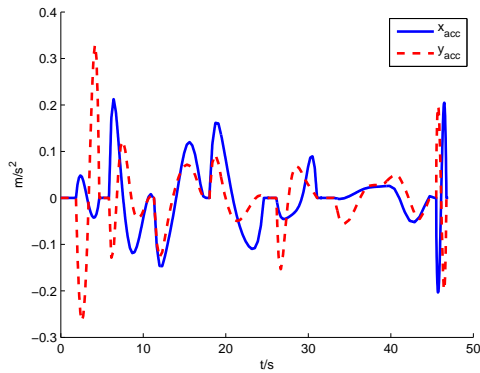


(a) Without time re-segmentation

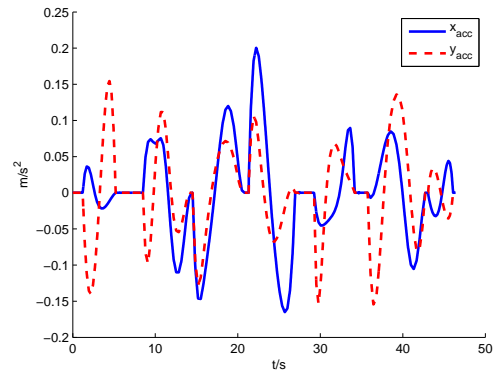


(b) With time re-segmentation

**Figure 8.6:** User input and generated spline of Chinese character *Guang*



(a) Without time re-segmentation



(b) With time re-segmentation

**Figure 8.7:** Generated spline's acceleration of Chinese character *Guang*

of  $f$  numerically as

$$\nabla f = \frac{f(\mathbf{T} + h\mathbf{g}_i) - f(\mathbf{T})}{h}, \quad (8.2)$$

where  $h$  is a small number at the level of  $10^{-6}$ ,  $\mathbf{g}_i$  is a perturbation vector with two choices: If the total time to finish the trajectory is allowed to change then  $\mathbf{g}_i$  is designed such that its  $i$ -th element is 1 and all the others are 0; If the total time is fixed, then  $\mathbf{g}_i$  is designed such that its  $i$ -th element is 1 and all the others are  $-1/N - 2$ . This is to make sure the  $\sum g_i = 0$  so that the total trajectory time remains the same. With the numerically obtained gradient, the gradient descent method is performed using backtrack line search.

By automatic time re-segmentation, the trajectory is further smoothen. It is now more suitable for MAV to perform precision tracking. The benefit of time re-segmentation can be viewed in Fig. 8.4 to Fig. 8.7. In the first case study, a simple vortex was hand-drawn to the system. Fig. 8.4 shows the reconstructed B-spline trajectories both without and with time re-segmentation respectively. Although the trajectory improvement of spline with time re-segmentation seems insignificant in this case, the resulted acceleration reference (Fig. 8.5) becomes smoother. Besides, the time of the trajectory has improved significantly. In another case study, a Chinese character *Guang* was written. It can be seen that the time re-segmentation improves the interpolation accuracy of the generated trajectory (Fig. 8.6). According to Fig. 8.7, the generated acceleration reference to the MAV is relatively more gentle compared to the result without time re-segmentation.

## 8.5 MAV Autonomous Writing Results

In the actual implementation, the MAV trajectories are generated pre-flight by running a set of MATLAB codes implementing the proposed trajectory planning algorithm. Then, a MATLAB Simulink program is constructed to acquire position and velocity measurements from the Vicon system and execute the outer-loop control law in real time.

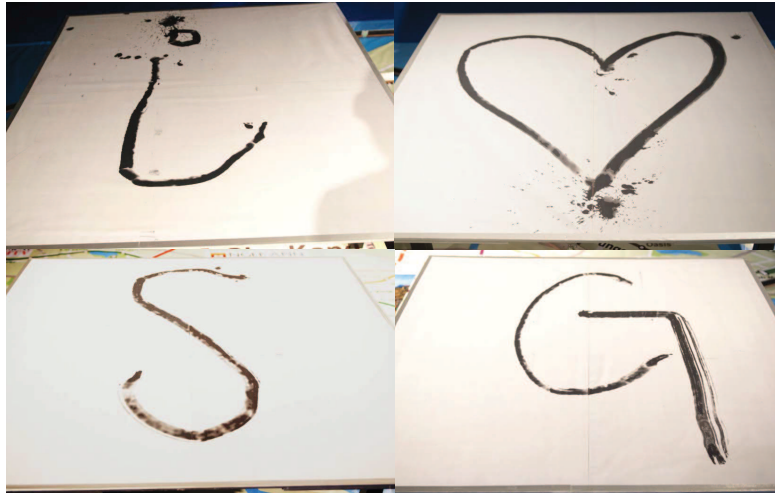
In the testing environment, a graphical interface which allows user handwritten input is



**Figure 8.8:** Four MAVs writing calligraphy to the public

presented using a Windows Surface Pro tablet (see Fig. 8.2). The interface was developed with MATLAB and it is able to transmit user input wirelessly from the Surface to the ground station. The whole MAV calligraphy system has been tested with various arbitrary handwritten inputs. Calligraphy flight performances of public inputs to the system via the Surface were demonstrated live to the audience during the Singapore Airshow 2014 held in Changi Exhibition Centre, Singapore. In the system setup during the Airshow, four MAVs are commanded to write four different characters at the same time (see Fig. 8.8). Reliability and robustness of the whole system has been well tested throughout the entire Airshow duration of 6 days. Several examples of the written words are shown in Fig. 8.9.

Besides the visual results, flight tests data were also logged for observation and possible improvement. Fig. 8.10 shows the  $x$ -,  $y$ - and  $z$ -axis position tracking results during one of the flight test. In general, the MAV is able to perform trajectory tracking almost perfectly, as a result of the RPT controller used in the outer-loop control. However, off-sets were observable on  $z$ -direction when the MAV descended to certain height due to the ground effect of the MAV from the writing pad.



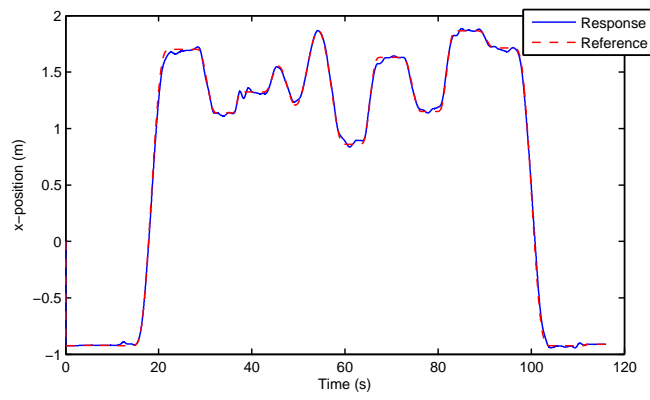
(a) *i love SG (Singapore)*



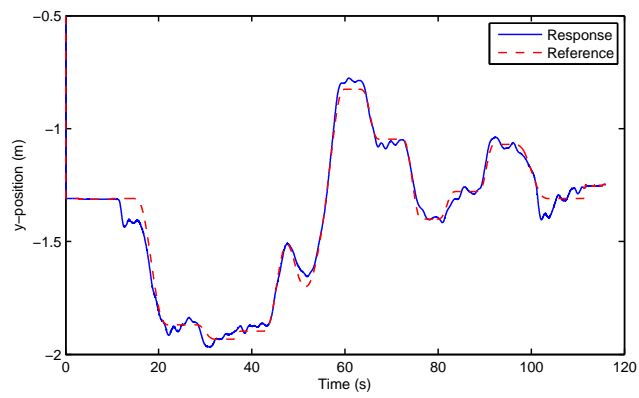
(b) *yi ma dang xian*

**Figure 8.9:** Samples of the MAV calligraphy results

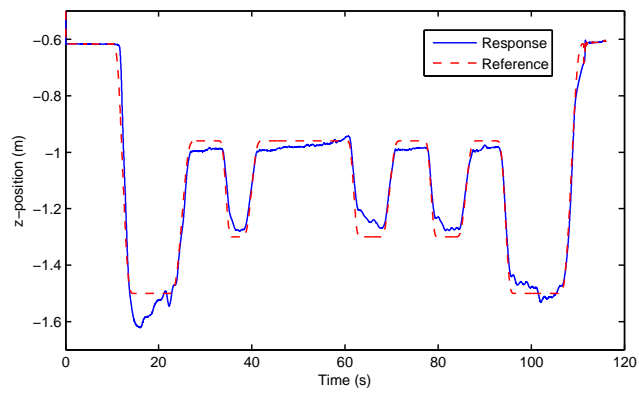




(a)  $x$ -position



(b)  $y$ -position



(c)  $z$ -position

**Figure 8.10:** Position tracking of the MAV

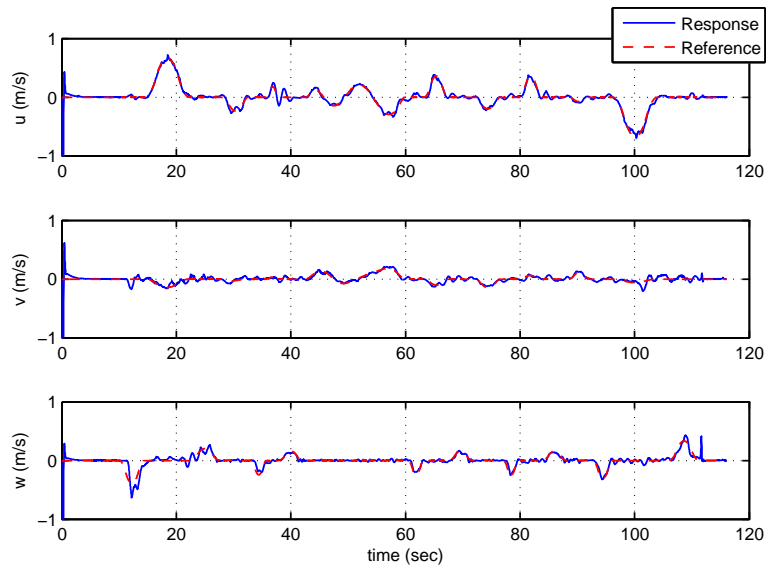
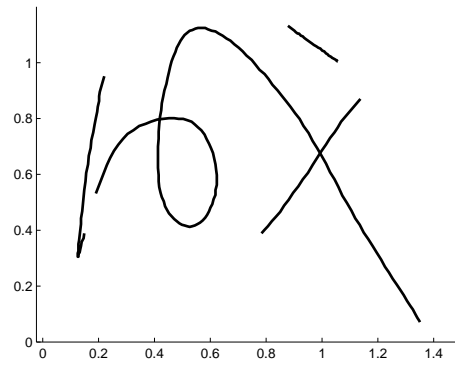
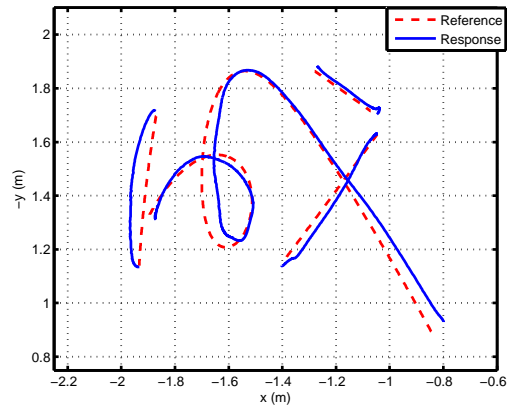


**Figure 8.11:** Velocity tracking of the MAV

Fig. 8.11 shows the velocity references and the corresponding responses during calligraphy writing. The benefit of the RPT controller is clearly shown here as the MAV not only tracks its trajectory well, but also has good velocity control performance. Finally, three diagrams of the Chinese character *Cheng* are shown in Fig. 8.12. The first diagram shows the user handwritten input via the Surface application we have created. The second diagram shows the generated path (dotted line) of the MAV based on B-spline optimization incorporated with the aircraft dynamics, while the solid line shows the MAV trajectory response. The final diagram shows the result of the MAV calligraphy on the writing board. The results are satisfying.



(a) User handwritten input



(b) Generated reference and its response



(c) Writing result

**Figure 8.12:** Sequence of processing



## Chapter 9

# Conclusion and Future Work

In this thesis, the topic of MAV system design and development has been discussed in both breadth and depth. With the general aim to develop a small-scale autonomous air vehicle for indoor applications, various design considerations and technics have been proposed and investigated. This thesis provides systematic guidelines towards the choice of the platforms, the structure design considerations, and the avionics circuit board design process. It also provides a detail derivation on the mathematics model of the MAV, several methods of identifying model's parameters, controller implementation and path optimization algorithm. Most importantly, these findings and guidelines are supported by both simulation and experimental results. A summary of main contributions of this thesis in the field of MAV is followed:

1. Multiple platforms were carefully studied on their potential to be developed into MAV platform;
2. An optimum structure and shape of the MAV platform is obtained through finite element analysis. While constrained by its size and weight, the MAV fuselage is designed such that no additional components such as bolts and nuts are needed. The airframe can be 3D printed to include mechanism to hold different parts of the fuselage.
3. A circuit design incorporate necessary sensors and processors of the MAV is proposed to

<b>Component</b>	<b>Budgeted Weight (g)</b>	<b>Actual Weight (g)</b>
<b>Power supply:</b>	15	
Battery		9.80
<b>Hardware:</b>	20	
Motor and propeller		14.36
Quadrotor arms		3.72
Quadrotor frame		2.13
<b>Circuit board:</b>	15	
Avionic system		7.32
Camera system		6.25
<b>Miscellaneous:</b>		1.70
<b>Total</b>	<b>50</b>	<b>45.28</b>

**Table 9.1:** Weight budget and final weight

greatly reduce the components weight. A complete weight breakdown together with the proposed weight budget of each parts can be found in Table. 9.1;

4. Dynamics model of the MAV systems is identified. Flight controllers are designed on the model;
5. Minimum jerk trajectory optimization with initial and final positions, velocities, and accelerations is proposed;
6. A case study is presented on calligraphy writing with MAV.

As the progress of the quadrotor MAV development, a few limitations of the platform were surfaced:

1. *Size of the platform:* as the size of the designed platform is approximately 15 cm in largest dimension, it limits the potential implementation of powerful avionic sensors and processors, such as high grade IMU and high performance central processing unit (CPU) or graphics processing unit (GPU). To overcome the limitation, size and weight budget for the MAV need to be relaxed. It enables the installment of high grade components, which are usually heavier. It is a typical trade-off scenario between the size of the MAV

and the performance of the avionic system. Nonetheless, as technology advances, smaller and smarter components will be developed and available commercially. It might solve the size issue of the platform in the future;

2. *Communication with GCS*: As the vision based motion estimation was done in GCS, a strong communication link between the MAV and the GCS must be ensured. The current down-link system uses 5.8 GHz wireless communication, in which the line-of-sight requirement must be satisfied. Also, occasional communication lost also resulted in degradation of the video quality, and thus affects the performance of the vision based motion estimation. A possible and good solution to this issue is to move the processing of the vision algorithm on-board, such that the performance of the MAV is not over-relied on the communication performance. However, moving the processing on-board requires the implementation of high performance GPU, and possibly FPGA circuits to efficiently run the algorithms.

Based on the above-mentioned points, there are still huge room for improvement for the MAV development, especially in the development of mission critical MAV.

Throughout this work, high potential of future work for MAVs is noticeable. MAVs' agility, size and extended operation envelope have made them suitable for useful applications like aerial surveillance, surveying and mapping, and search and rescue. However, the exploration of MAVs is still at its infancy stage. There is still a large gap between academic research results and mature industrial applications. The majority of research results are obtained in ideal environments with rich reference information, such as good line-of-sight communication, unblocked GPS signal, and obstacle-free environments. For implementations in realistic indoor and outdoor cluttered environments, in which only MAVs can operate, there are generally very limited reference resources. Enhancing the intelligence of MAVs to handle these challenging situations is what the end users are looking for.

Follows from the end of this thesis, the author aims to investigate the problem of intelligent navigation of MAVs in realistic indoor and outdoor cluttered environments without global referencing resources. This target can be achieved by systematic integration of achievements of the following four tasks:

1. MAV platform design with small size but sufficient payload and endurance;
2. Robust and precise ego-motion estimation in indoor and outdoor cluttered environments via on-board relative sensors;
3. Navigation in cluttered environments with obstacle avoidance;
4. Smooth navigation transition between indoor and outdoor environments.

The proposed algorithms and methods will be tested and verified using actual MAV platforms. Multiple indoor and outdoor scenarios will be defined or developed for the developed MAVs to demonstrate its functionalities.

Throughout the years while developing the MAV system, the author has taken part in several UAV related competitions. He has made his contribution on platform structure design of UAVs in the US DARPA UAVForge Challenge held in Atlanta in 2012 and the AVIC Cup International Innovation UAV Grand Prix in Beijing the following year. In 2014, he co-lead a team to win the International Micro Air Vehicle competition held in Delft. In this competition, multiple quadrotor MAVs were used to complete four different missions. The platform structural design, avionics design and the controller implementation proposed in this thesis have made significant contribution to the team.



# Bibliography

- [1] 800HighTech (2011), *AeroVironment Nano Humming Bird UAV* [Online]. Available: <http://www.hightech-edge.com/aerovironment-nano-humming-bird-flapping-wing-uav-video-clip/10309>
- [2] M. Achtelik, A. Bachrach, R. He, S. Prentice and N. Roy, "Autonomous navigation and exploration of a quadrotor helicopter in GPS-denied indoor environments," *Proceedings of the IEEE ICRA*, Kobe, 2009
- [3] R. Albertani, B. Stanford, J. Hubner and P. Ifju, "Characterization of flexible-wing MAVs: aeroelastic and propulsion effects on flying qualities," *Proceedings of the AIAA Atmospheric Flight Mechanics Conf. and Exhibit*, San Francisco, Paper 6324, 2005.
- [4] B. Beasley, "A study of planar and nonplanar membrane wing platforms for the design of a flapping-wing micro air vehicle," Master thesis, University of Maryland, US, 2006.
- [5] A. Berman (April, 2005), *Basics of choosing a motor and ESC/MSM and Brushed vs. Brushless Systems* [Online]. Available: [http://www.rcuniverse.com/magazine/article\\_display.cfm?article\\_id=505](http://www.rcuniverse.com/magazine/article_display.cfm?article_id=505)
- [6] C. de Boor, *A Practical Guide to Splines*. Springer-Verlag, New York, 1978.
- [7] G. A. Borges and M. J. Aldon, "A split-and-merge segmentation algorithm for line extraction in 2d range images," *Proceedings of the 15th Int. Conf. on Pattern Recognition*, Barcelona, Spain, pp. 441-444, 2000.

- [8] S. A. Bortoff, "The University of Toronto RC helicopter: a testbed for nonlinear control," *Proceedings of the 1999 IEEE Int. Conf. Control Applications*, Honolulu, Hawaii, pp. 333-338, 1999.
- [9] S. Bouabdallah, P. Murrieri and R. Siegwart, "Towards autonomous indoor micro VTOL," *Autonomous Robots*, vol. 18(2), pp. 171-183, 2005.
- [10] S. Bouabdallah, A. Noth and R. Siegwart, "PID vs LQ control techniques applied to an indoor micro quadrotor," *Proceedings of the IEEE Int. Conf. on Intelligent Robots and Systems*, pp. 2451-2456, 2004.
- [11] T. Bresciani, "Modelling, identification and control of a quadrotor helicopter," Master thesis, Lund University, Lund, Sweden, Oct, 2008.
- [12] G. Cai, B. M. Chen and T. H. Lee, *Unmanned Rotorcraft Systems*, Springer, New York, 2011.
- [13] H. Chao, Y. Cao and Y. Q. Chen, "Autopilots for small fixed-wing unmanned air vehicles: a survey," *Proceedings of the 2007 IEEE Int. Conf. on Mechatronics and Automation*, Harbin, China, pp. 3144-3149, 2007.
- [14] W. S. Clarence, *Vibration: Fundamentals and Practice*, CRC Press, 1999.
- [15] C. E. Cohen, B. W. Parkinson and B. D. McNally, "Flight tests of attitude determination using GPS compared against an inertial navigation unit," *Navigation*, vol. 41(1), pp. 83-97, 1994.
- [16] R. Cory and R. Tedrake, "Experiments in fixed-wing UAV perching," *Proceedings of the AIAA Guidance, Navigation, and Control Conf. and Exhibit*, Honolulu, Hawaii, pp. 7256-7267, 2008.
- [17] M. Cowley, *AeroVironment's WASP micro air vehicle sets world record* [Online]. Available: <http://www.aerovironment.cn/news/news-archive/wasp62.html>

- [18] A. Das, K. Subbarao and F. Lewis, "Dynamic inversion with zero-dynamics stabilisation for quadrotor control," *IET Control Theory & Applications*, vol. 3(3), pp. 303-314, 2009.
- [19] DelFly, *DelFly Micro* [Online]. Available: <http://www.delfly.nl>
- [20] A. Eresen, N. Imamoglu and M.O. Efe, "Autonomous quadrotor flight with vision-based obstacle avoidance in virtual environment," *Expert Systems with Applications*, vol. 39(1), pp. 894-905, 2012.
- [21] S. M. Ettinger, M. C. Nechyba, P. G. Ifju and M. Waszak, "Vision-guided flight stability and control for micro air vehicles," *Proceedings of the 2002 IEEE/RSJ Int. Conf. on Intelligent Robots and Systems*, Lausanne, vol. 3, pp. 2134-2140, 2002.
- [22] F. Fraundorfer, L. Heng, D. Honegger, G. H. Lee, L. Meier, P. Tanskanen and M. Pollefeys, "Vision-based autonomous mapping and exploration using a quadrotor MAV," *Proceedings of the IEEE/RSJ Int. Conf. on Intelligent Robots and Systems (IROS)*, Vilamoura, pp. 4557-4564, 2012.
- [23] V. Ghadiok, J. Goldin and W. Ren, "Autonomous indoor aerial gripping using a quadrotor," *Proceedings of 2011 IEEE/RSJ Int. Conf. on Intelligent Robots and Systems (IROS)*, San Francisco, CA, pp. 4645-4651, 2011.
- [24] R. Goel, S. M. Shah, N. K. Gupta and N. Ananthkrishnan, "Modeling, simulation and flight testing of an autonomous quadrotor," *Proceedings of the Int. Conf. on Environmental and Agriculture Engineering*, 2009.
- [25] J. M. Grasmeyer and M. T. Keennon, "Development of the black widow micro air vehicle," *American Institute of Aeronautics and Astronautics*, vol. 195, pp.519-535, 2011.
- [26] W. E. Green, P. Y. Oh and G. Barrows, "Flying insect inspired vision for autonomous aerial robot maneuvers in near-earth environments," *Proceedings of the 2004 IEEE Int. Conf. on Robotics and Automation*, New Orleans, LA, vol. 3, pp. 2347-2352, 2004.

- [27] J. F. Guerrero-Castellanos, N. Marchand, A. Hably, S. Lesecq and J. Delamare, "Bounded attitude control of rigid bodies: real-time experimentation to a quadrotor mini-helicopter," *Control Engineering Practice*, vol. 19(8), pp. 790-797, 2011.
- [28] T. Hamel, R. Mahony, R. Lozano and J. Ostrowski, "Dynamic modelling and configuration stabilization for an X4-flyer," *Proceedings of the 15th Triennial World Congress of IFAC*, Barcelona, Spain, pp. 846-851, 2002
- [29] C. M. Harris, *Shock and Vibration Handbook*, 4th ed. New York, NY:McGraw-Hill, 1996.
- [30] A. S. Huang, A. Bachrach, P. Henry, M. Krainin, D. Maturana, D. Fox and N. Roy, "Visual odometry and mapping for autonomous flight using an RGB-D camera," *Proceedings of the Int. Symp. on Robotics Research (ISRR)*, Flagstaff, Arizona, pp. 1-16, 2011.
- [31] H. C. Hwang, D. K. Chung, K. J. Yoon, H. C. Park, Y. J. Lee and T. S. Kang, "Design and flight test of a fixed wing MAV," *Proceedings of the AIAA's 1st Technical Conf. and Workshop on Unmanned Aerospace Vehicle*, Portsmouth, Virginia, 2002.
- [32] C. Jablonski (2009), *Flapping nano aircraft takes flight* [Online]. Available: <http://www.zdnet.com/blog/emergingtech/flapping-nano-aircraft-takes-flight/1711>
- [33] J. S. Jang and D. Liccardo, "Small UAV automation using MEMS," *IEEE Aerospace Electron System Magazine*, vol. 22, pp. 30-34, 2007.
- [34] E. N. Johnson, M. A. Turbe, A. D. Wu, S. K. Kannan and J. C. Neidhoefer, "Flight test results of autonomous fixed-wing UAV transitions to and from stationary hover," *Proceedings of the AIAA Guidance, Navigation, and Control Conf. Exhibit*, Monterey, Colorado, 2006.
- [35] H. Kano, H. Fujioka and C. F. Martin, "Optimal smoothing and interpolating splines with constraints," *Applied Mathematics and Computation*, vol. 218(5), pp. 1831-1844, 2011.

- [36] H. Kano, H. Nakata and C. F. Martin, "Optimal curve fitting and smoothing using normalized uniform B-splines: a tool for studying complex systems," *Applied Mathematics and Computation*, vol. 159(1), pp. 96-128, 2005.
- [37] J. Keller, D. Thakur, V. Dobrokhodov, K. Jones, M. Pivtoraiko, J. Gallier, I. Kaminer and V. Kumar, "A computationally efficient approach to trajectory management for coordinated aerial surveillance," *Unmanned Systems*, vol. 1(1), pp. 59-74, 2013.
- [38] D. D. Kreculj, "Stress analysis in an unidirectional carbon/epoxy composite material," *FME Transactions*, vol. 36(3), pp. 127-132, 2008.
- [39] I. Kroo and P. Kunz, "Mesoscale flight and miniature rotorcraft development," *Proceedings of the Fixed and Flapping Wing Aerodynamics for Micro Air Vehicle Applications*, AIAA, pp. 503-517, 2001.
- [40] Lacasse Fine Wood Products Inc. (2008), *Comparison Between Brush and Brushless Motors* [Online]. Available: <http://www.bestwoodworkingrouters.com/CNCmachineParts/CNCspindleMotors-7brushlessVSbrush.shtml>
- [41] K. Li, R. Huang, S. K. Phang, S. Lai, F. Wang, P. Tan, B. M. Chen and T. H. Lee, "Vision-based autonomous control of an ultralight quadrotor MAV," *Proceedings of the 2014 Int. Micro Air Vehicle Conf. and Competition*, Delft, The Netherlands, pp. 50-57, August 2014.
- [42] K. Li, S. K. Phang, B. M. Chen and T. H. Lee, "Platform design and mathematical modeling of an ultralight quadrotor micro aerial vehicle," *Proceedings of the 2013 Int. Conf. on Unmanned Aircraft Systems*, Atlanta, US, pp. 1066-1075, May 2013.
- [43] L. Meier, P. Tanskanen, L. Heng, G. H. Lee, F. Fraundorfer and M. Pollefeys, "PIXHAWK: A micro aerial vehicle design for autonomous flight using onboard computer vision," *Autonomous Robots*, vol. 5(1-2), pp. 21-39, 2012.

- [44] L. Meier, P. Tanskanen, F. Fraundorfer and M. Pollefeys, "PIXHAWK: A system for autonomous flight using onboard computer vision," *Proceedings of 2011 IEEE Int. Conf. on Robotics and Automation (ICRA)*, Shanghai, China, pp. 2992-2997, 2011.
- [45] D. Mellinger and V. Kumar, "Minimum snap trajectory generation and control for quadrotors," *Proceedings of 2011 IEEE Int. Conf. on Robotics and Automation (ICRA)*, Shanghai, China, pp. 2520-2525, 2011.
- [46] D. Mellinger, M. Shomin, V. Kumar, "Control of quadrotors for robust perching and landing," *Proceedings of the Int. Conf. on Powered Lift*, Philadelphia, Oct 2010.
- [47] D. Mellinger, M. Nathan, V. Kumar, "Trajectory generation and control for precise aggressive maneuvers with quadrotors," *Int. J. Robotics Research*, vol. 31(5), pp. 664-674, 2012.
- [48] N. Michael, D. Mellinger, Q. Lindsey and V. Kumar, "The grasp multiple micro-uav testbed," *IEEE Robotics & Automation Magazine*, vol. 17(3), pp. 56-65, 2010.
- [49] R. C. Michelson and S. Reece, "Update on flapping wing micro air vehicle research-ongoing work to develop a flapping wing, crawling entomopter," *Proceedings of the 13th Bristol Int. Conf. on RPV/UAV Systems*, Bristol, England, vol. 30, pp 30-41, 1998.
- [50] MLB Company (2003), *Trochoid* [Online]. Available: <http://mlbuav.com/trochoid.html>
- [51] M. W. Mueller, M. Hehn and R. D'Andrea, "A computationally efficient algorithm for state-to-state quadrocopter trajectory generation and feasibility verification," *Proceedings of the IEEE/RSJ Int. Conf. on Intelligent Robots and Systems*, pp. 3480-3486, 2013.
- [52] R. Naldi, L. Gentili, L. Marconi and A. Sala, "Design and experimental validation of a nonlinear control law for a ducted-fan miniature aerial vehicle," *Control Engineering Practice*, vol. 18(7), pp. 747-760, 2010.

- [53] J. Nocedal and S. J. Wright, *Numerical Optimization*. Springer Series in Operations Research and Financial Engineering, Second Edition, Springer, 2006.
- [54] Oriental Motor USA Inc. (2011), *Basics of Motion Control* [Online]. Available: <http://www.orientalmotor.com/technology/articles/AC-brushless-brushed-motors.html>
- [55] S. K. Phang, C. Cai, B. M. Chen and T. H. Lee, "Design and mathematical modeling of a 4-standard-propeller (4SP) quadrotor," *Proceedings of the 10th World Congress on Intelligent Control and Automation*, Beijing, China, pp. 3270-3275, 2012.
- [56] S. K. Phang, S. Lai, F. Wang, M. Lan and B. M. Chen, "UAV calligraphy," *Proceedings of the 11th IEEE Int. Conf. on Control & Automation*, Taichung, Taiwan, pp. 422-428, 2014.
- [57] S. K. Phang, K. Li, B. M. Chen and T. H. Lee, "Systematic design methodology and construction of micro aerial quadrotor vehicles," *Handbook of Unmanned Aerial Vehicle*, K. P. Valavanis and G. J. Vachtsevanos, Eds. Springer, pp. 181-206, 2014.
- [58] S. K. Phang, K. Li, F. Wang, B. M. Chen and T. H. Lee, "Explicit model identification and control of a micro aerial vehicle," *Proceedings of the 2014 Int. conf. on Unmanned Aircraft Systems*, Orlando, US, pp. 1048-1054, May 2014.
- [59] S. K. Phang, K. Li, K. H. Yu, B. M. Chen and T. H. Lee, "Systematic design and implementation of a micro quadrotor UAV," *Unmanned Systems*, vol. 2(2), pp. 121-141, 2014.
- [60] S. K. Phang, J. J. Ong, R. Yeo, B. M. Chen and T. H. Lee, "Autonomous mini-UAV for indoor flight with embedded on-board vision processing as navigation system," *Proceedings of the IEEE R8 Int. Conf. on Computational Technologies in Electrical and Electronics Engineering*, Irkutsk Listvyanka, Russia, pp. 722-727, July 2010.
- [61] D. J. Pines, and F. Bohorquez, "Challenges facing future micro-air-vehicle development," *Journal of Aircraft*, vol. 43(2), pp. 290-305, 2006.

- [62] D. Quick (2011), *World's first hummingbird-like unmanned aircraft system takes flight* [Online]. Available: <http://www.gizmag.com/aerovironment-nano-hummingbird/17918>
- [63] S. Raju, B. K. Murthy, S. Kumar and V. K. Reddy, "Effect of thickness ratio on nonlinear static behaviour of skew bidirectional FRP laminates with circular cutout," *Int. J. of Applied Engineering Research*, vol. 1(4), pp. 923-932, 2011.
- [64] C. Richter, A. Bry, and N. Roy, *Polynomial trajectory planning for quadrotor flight* [Online]. Available: <http://www.michigancmes.org/papers/roy7.pdf>
- [65] F. Ruffier, S. Viollet, S. Amic and N. Franceschini, "Bio-inspired optical flow circuits for the visual guidance of micro air vehicles," *Proceedings of the 2003 Int. Symp. on Circuits and Systems*, Bangkok, vol. 3, pp. 846-849, 2003.
- [66] Z. Sarris, "Survey of UAV applications in civil markets," *Proceedings of the 9th Mediterranean Conf. on Control and Automation*, Dubrovnik, Croatia, 2001.
- [67] D. Schafroth, S. Bouabdallah, C. Bermes and R. Siegwart, "From the test benches to the first prototype of the muFly micro helicopter," *Intelligent and Robotic Systems*, vol. 54, pp. 245-260, 2008.
- [68] J. Sirohi, M. Tishchenko and I. Chopra, "Design and Testing of a Micro-Aerial Vehicle with a Single Rotor and Turning Vanes," *61st Annual Forum of the American Helicopter Society*, 2004.
- [69] K. Takayama and H. Kano, "A new approach to synthesizing free motions of robotic manipulators based on the concept of unit motion," *IEEE Transactions on Systems, Man and Cybernetics*, vol. 25(3), pp. 453-463, 1995.
- [70] C. Thipyopas, A. B. Sun, E. Bernard and J. M. Moschetta, "Application of electro-active materials to a coaxial-rotor NAV," *Int. J. of Micro Air Vehicles*, vol. 3(4), pp. 247-260, 2012.



- [71] B. Wang, X. Dong, B. M. Chen, T. H. Lee and S. K. Phang, "Formation Flight of unmanned rotorcraft based on robust and perfect tracking approach," *Proceedings of the 2012 American Control Conf.*, pp. 3284-3290, 2012.
- [72] F. Wang, P. Liu, S. Zhao, B. M. Chen, S. K. Phang, S. Lai and T. H. Lee, "Guidance, navigation and control of an unmanned helicopter for automatic cargo transportation," *Proceedings of the 2014 Chinese Control Conf.*, Nanjing, China, pp. 1013-1020, 2014.
- [73] F. Wang, S. K. Phang, J. J. Ong, B. M. Chen and T. H. Lee, "Design and construction methodology of an indoor UAV system with embedded vision," *Control and Intelligent Systems*, vol. 40(1), pp 22-32, 2012.
- [74] F. Wang, K. Wang, S. Lai, S. K. Phang, B. M. Chen and T. H. Lee, "An efficient UAV navigation solution for confined but partially known indoor environments," *Proceedings of the 11th IEEE Int. Conf. on Control & Automation*, Taichung, Taiwan, pp. 1351-1356, 2014.
- [75] R. J. Wood, S. Avadhanula, E. Steltz, M. Seeman, J. Entwistle, A. Bachrach, G. Barrows and S. Sanders, "An autonomous palm-sized gliding micro air vehicle," *IEEE Robotics & Automation Magazine*, vol. 14(2), pp. 82-91, 2007.
- [76] R. Zhang, X. Wang and K. Cai, "Quadrotor aircraft control without velocity measurements," *Proceedings of the 48th IEEE Conf. on Decision and Control*, Shanghai, China, pp. 5213-5218, 2009.



# Publications

## Book Chapter

1. **S. K. Phang**, K. Li, B. M. Chen and T. H. Lee, “Systematic design methodology and construction of micro aerial quadrotor vehicles,” in *Handbook of Unmanned Aerial Vehicles*, K. P. Valavanis and G. J. Vachtsevanos, Eds. Springer, 2014, pp. 181-206.

## Refereed Journal

1. **S. K. Phang**, S. Lai, F. Wang, M. Lan and B. M. Chen, “Systems design and implementation with jerk-optimized trajectory generation for UAV calligraphy,” *Submitted for publication*.
2. F. Wang, P. Liu, S. Zhao, B. M. Chen, **S. K. Phang**, S. Lai, T. Pang, B. Wang, C. Cai and T. H. Lee, “Development of an unmanned helicopter for vertical replenishment,” *Unmanned Systems*, in press.
3. **S. K. Phang**, K. Li, K. H. Yu, B. M. Chen and T. H. Lee, “Systematic design and implementation of a micro quadrotor UAV,” *Unmanned Systems*, vol 2, no 2, pp 121-141, April 2014.
4. F. Lin, K. Ang, F. Wang, B. M. Chen, T. H. Lee, B. Yang, M. Dong, X. Dong, J. Cui, **S. K. Phang**, B. Wang, D. Luo, K. Peng, G. Cai, S. Zhao, M. Yin and K. Li, “Development of an

unmanned coaxial rotorcraft for the DARPA UAVForge challenge,” *Unmanned Systems*, vol 1, no 2, pp 211-245, September 2013.

5. F. Wang, **S. K. Phang**, J. J. Ong, B. M. Chen and T. H. Lee, “Design and construction methodology of an indoor UAV system with embedded vision,” *Control and Intelligent Systems*, vol 40, no 1, pp 22-32, February 2012.

## **International Conference**

1. **S. K. Phang**, J. Cui, K. Ang, F. Wang, X. Dong, Y. Ke, S. Lai, K. Li, X. Li, F. Lin, J. Lin, P. Liu, T. Pang, B. Wang, K. Wang, Z. Yang and B. M. Chen, “Urban post-disaster search and rescue solutions with unmanned aircraft systems,” *To be presented in the 2015 International Conference on Electronics, Information and Communication*, Singapore, January 2015.
2. K. Li, R. Huang, **S. K. Phang**, S. Lai, F. Wang, P. Tan, B. M. Chen and T. H. Lee, “Vision-based autonomous control of an ultralight quadrotor MAV,” *Proceedings of the 2014 International Micro Air Vehicle Conference and Competition*, Delft, The Netherlands, pp. 50-57, August 2014.
3. F. Wang, P. Liu, S. Zhao, B. M. Chen, **S. K. Phang**, S. Lai and T. H. Lee, “Guidance, navigation and control of an unmanned helicopter for automatic cargo transportation,” *Proceedings of the 2014 Chinese Control Conference*, Nanjing, China, pp. 1013-1020, July 2014.
4. F. Wang, K. Wang, S. Lai, **S. K. Phang**, B. M. Chen and T. H. Lee, “An efficient UAV navigation solution for confined but partially known indoor environments,” *Proceedings of the 11th IEEE International Conference on Control & Automation*, Taichung, Taiwan, pp. 1351-1356, June 2014.

5. **S. K. Phang**, S. Lai, F. Wang, M. Lan and B. M. Chen, "UAV calligraphy," *Proceedings of the 11th IEEE International Conference on Control & Automation*, Taichung, Taiwan, pp. 422-428, June 2014.
6. **S. K. Phang**, K. Li, F. Wang, B. M. Chen and T. H. Lee, "Explicit model identification and control of a micro aerial vehicle," *Proceedings of the 2014 International conference on Unmanned Aircraft Systems*, Orlando, US, pp. 1048-1054, May 2014.
7. F. Lin, K. Ang, F. Wang, B. M. Chen, T. H. Lee, B. Yang, M. Dong, X. Dong, J. Cui, **S. K. Phang**, B. Wang, D. Luo, S. Zhao, M. Yin, K. Li, K. Peng and G. Cai, "Development of an unconventional unmanned coaxial rotorcraft: GremLion," *Proceedings of the 15th International Conference on Human-Computer Interaction*, Las Vegas, US, pp. 120-129, July 2013.
8. F. Wang, J. Cui, **S. K. Phang**, B. M. Chen and T. H. Lee, "A mono-camera and scanning laser ranger finder based UAV indoor navigation system," *Proceedings of the 2013 International conference on Unmanned Aircraft Systems*, Atlanta, US, pp. 693-700, May 2013.
9. K. Li, **S. K. Phang**, B. M. Chen and T. H. Lee, "Platform design and mathematical modeling of an ultralight quadrotor micro aerial vehicle," *Proceedings of the 2013 International conference on Unmanned Aircraft Systems*, Atlanta, US, pp. 1066-1075, May 2013.
10. **S. K. Phang**, C. Cai, B. M. Chen and T. H. Lee, "Design and mathematical modeling of a 4-standard-propeller (4SP) quadrotor," *Proceedings of the 10th World Congress on Intelligent Control and Automation*, Beijing, China, pp. 3270-3275, July 2012.
11. F. Wang, **S. K. Phang**, J. Cui, G. Cai, B. M. Chen and T. H. Lee, "Nonlinear modeling of a miniature fixed-pitch coaxial UAV," *Proceedings of the 2012 American Control Conference*, Montreal, Canada, pp. 3863-3870, June 2012.

12. B. Wang, X. Dong, B. M. Chen, T. H. Lee and **S. K. Phang**, “Unmanned rotorcrafts formation flight based on robust and perfect tracking approach,” *Proceedings of the 2012 American Control Conference*, Montreal, Canada, pp. 3284-3290, June 2012.
13. F. Wang, **S. K. Phang**, J. Cui, B. M. Chen and T. H. Lee, “Search and rescue: a UAV aiding approach,” *Proceedings of the 23rd Canadian Congress of Applied Mechanics*, Vancouver, BC, Canada, pp. 183-186, June 2011.
14. **S. K. Phang**, J. J. Ong, R. Yeo, B. M. Chen and T. H. Lee, “Autonomous mini-UAV for indoor flight with embedded on-board vision processing as navigation system,” *Proceedings of the IEEE R8 International Conference on Computational Technologies in Electrical and Electronics Engineering*, Irkutsk Listvyanka, Russia, pp. 722-727, July 2010.